

Article

Lithium deficiency and the onset of Alzheimer's disease

<https://doi.org/10.1038/s41586-025-09335-x>

Received: 4 September 2024

Accepted: 30 June 2025

Published online: 06 August 2025

Open access

 Check for updates

Liviu Aron¹, Zhen Kai Ngian¹, Chenxi Qiu¹, Jaejoon Choi¹, Marianna Liang¹, Derek M. Drake¹, Sara E. Hamplova¹, Ella K. Lacey¹, Perle Roche¹, Monlan Yuan¹, Saba S. Hazaveh¹, Eunjung A. Lee², David A. Bennett³ & Bruce A. Yankner¹✉

The earliest molecular changes in Alzheimer's disease (AD) are poorly understood^{1–5}. Here we show that endogenous lithium (Li) is dynamically regulated in the brain and contributes to cognitive preservation during ageing. Of the metals we analysed, Li was the only one that was significantly reduced in the brain in individuals with mild cognitive impairment (MCI), a precursor to AD. Li bioavailability was further reduced in AD by amyloid sequestration. We explored the role of endogenous Li in the brain by depleting it from the diet of wild-type and AD mouse models. Reducing endogenous cortical Li by approximately 50% markedly increased the deposition of amyloid-β and the accumulation of phospho-tau, and led to pro-inflammatory microglial activation, the loss of synapses, axons and myelin, and accelerated cognitive decline. These effects were mediated, at least in part, through activation of the kinase GSK3β. Single-nucleus RNA-seq showed that Li deficiency gives rise to transcriptome changes in multiple brain cell types that overlap with transcriptome changes in AD. Replacement therapy with lithium orotate, which is a Li salt with reduced amyloid binding, prevents pathological changes and memory loss in AD mouse models and ageing wild-type mice. These findings reveal physiological effects of endogenous Li in the brain and indicate that disruption of Li homeostasis may be an early event in the pathogenesis of AD. Li replacement with amyloid-evading salts is a potential approach to the prevention and treatment of AD.

The identification of treatable causes of AD requires a fundamental understanding of the pathogenic processes leading to memory loss. Although substantial progress has been made in defining gene variants that confer risk for AD, the environmental factors that affect the timing of disease onset are not as well understood^{1,6}. Several factors relating to diet, lifestyle and the environment have been identified, but their contributions to AD pathogenesis are unclear^{1,6,7}. Altered homeostasis of metals is one such factor^{7–12}. These studies have focused primarily on the toxic effects of metals such as iron, copper and zinc, which can promote amyloid-β (Aβ) aggregation, tau phosphorylation or oxidative stress in model systems^{6–12}. However, metals also have essential roles in brain function, and disruption of this normal physiology in AD is relatively unexplored.

Lithium deficiency in MCI and AD

To explore the role of metal-ion homeostasis in AD, we used inductively coupled plasma mass spectrometry (ICP–MS) to assess 27 abundant and trace metals in the brain and blood of aged individuals with no cognitive impairment (NCI) and individuals with amnestic MCI or AD. Metal levels were determined in the prefrontal cortex (PFC), which is a prominently affected region in AD, and the cerebellum, which is relatively unaffected. Of all the metals surveyed, only one, Li, showed

significantly reduced levels in the PFC of individuals with both MCI and AD (Fig. 1a,b and Supplementary Table 1). The mean and median Li cortex-to-serum ratio and total cortical Li were significantly reduced in the PFC of people with MCI and AD (Fig. 1c,d), but not in the cerebellum (Extended Data Fig. 1a,b). In a second independent cohort, Li levels were also significantly reduced in the PFC of people with AD (Fig. 1e). By contrast, the mean serum Li levels in MCI and AD were not significantly different from controls (Extended Data Fig. 1c). Li levels were not significantly affected by sex or the range of postmortem intervals in this study (see Methods). The cortex-to-serum ratios of several other metals also changed in AD, but not in MCI (Fig. 1a,b and Supplementary Table 1). However, the change in Li showed the lowest adjusted *P* value of all the metals analysed (Fig. 1b). Together, these results indicate that endogenous Li homeostasis is perturbed in the brain in MCI and AD.

We next investigated whether endogenous Li homeostasis in the brain might be perturbed by AD pathology. Previous studies have implicated the interaction of several metals with Aβ^{8,9}. To determine whether amyloid deposition affects the distribution of Li, we performed laser absorption (LA)-ICP–MS and quantified Li in amyloid plaques compared with plaque-free regions in the frontal cortex. A highly significant concentration of Li in Aβ plaques was detected in every case of MCI and AD, which increased from MCI to AD (Fig. 1f).

¹Department of Genetics, Harvard Medical School, Boston, MA, USA. ²Division of Genetics and Genomics, Boston Children's Hospital, Boston, MA, USA. ³Rush Alzheimer's Disease Center, Rush University Medical Center, Chicago, IL, USA. ✉e-mail: bruce_yankner@hms.harvard.edu

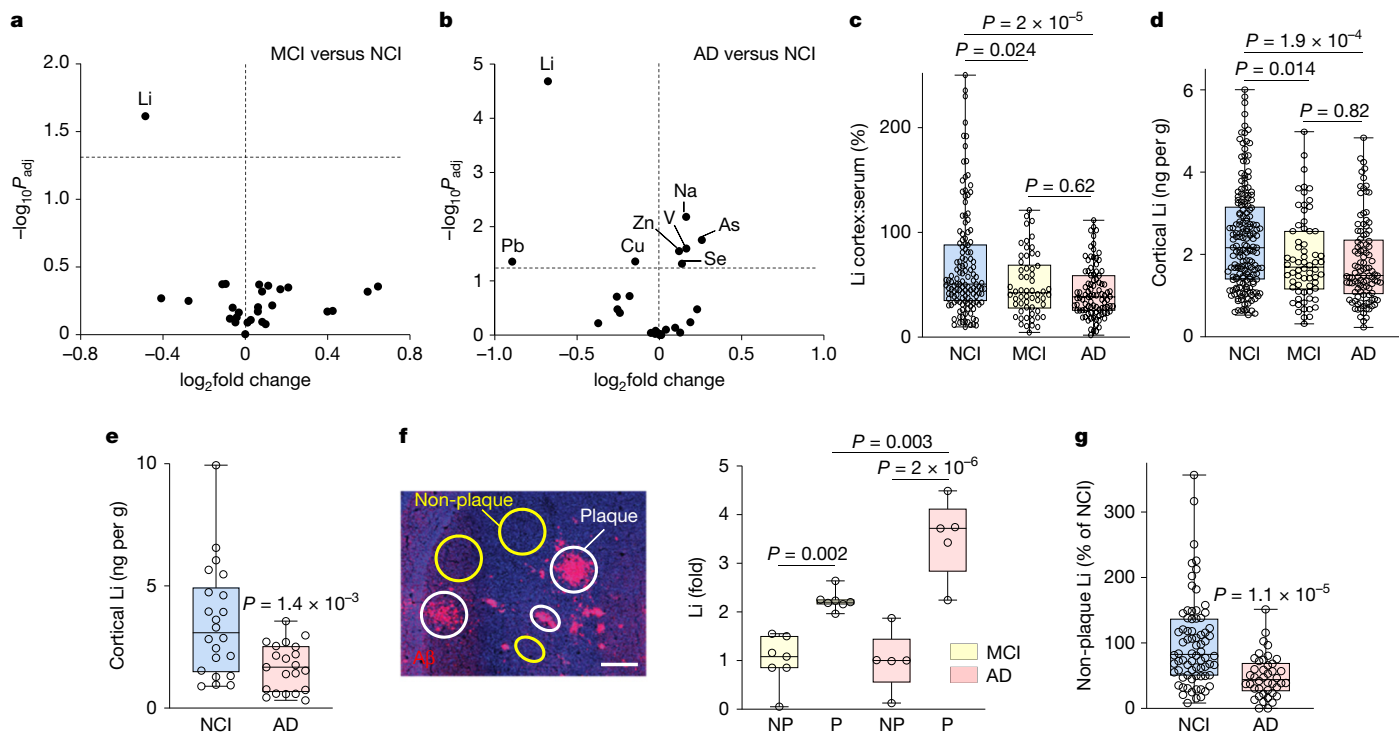


Fig. 1 | Lithium deficiency and the onset of AD. **a,b**, Volcano plots showing changes in metal cortex-to-serum ratios in the PFC of MCI versus NCI (**a**) and AD versus NCI (**b**) cases, along with their statistical significance, determined by one-way analysis of variance (ANOVA) with Tukey's post-hoc test, followed by the Benjamini–Hochberg correction for the number of metals assessed. **c,d**, Li cortex-to-serum ratios (**c**) and total cortical Li levels (**d**) in cases from ROSMAP. Each point represents an individual case. **e**, Total cortical Li in cases from a replication cohort. **f**, Li is concentrated in Aβ plaques in MCI and AD. Aβ immunolabelling in the PFC of an AD case (left). LA-ICP-MS was done on an adjacent unfixed section to quantify Li in Aβ plaques (white circles) and neighbouring non-plaque regions (yellow circles). Scale bar, 50 μm. The ratios of Li level in plaque (P) to

non-plaque (NP) regions are shown (right) in MCI and AD cases. **g**, Cortical brain samples were subfractionated into plaque-enriched and non-plaque fractions. Li levels in non-plaque fractions were measured by ICP-MS and normalized to the mean of NCI. *P* values were calculated by one-way (**a–d**) or two-way (**f**) ANOVA with Tukey's post-hoc and Benjamini–Hochberg corrections (**a–c**) or Tukey's post-hoc corrections (**d,f**), or by two-tailed unpaired *t*-test (**e,g**). **c–g**, Box plots show individual values, median (line), box limits (25th and 75th percentiles) and whiskers (minimum and maximum). **a–c**, NCI *n* = 133, MCI *n* = 58, AD *n* = 94. **d**, NCI *n* = 177, MCI *n* = 66, AD *n* = 105. **e**, NCI *n* = 22, AD *n* = 21. **f**, MCI *n* = 7, AD *n* = 5. **g**, NCI *n* = 74, AD *n* = 42.

To complement this *in situ* analysis, PFC samples were subfractionated into a plaque-enriched insoluble fraction and a soluble fraction devoid of amyloid plaques (Supplementary Fig. 1). The mean and median Li levels in the PFC non-plaque fraction were significantly reduced in AD relative to control NCI cases (Fig. 1g). Furthermore, lower Li levels in the non-plaque cortical fraction correlated with reduced cognitive test scores for episodic and semantic memory, and for a global index of cognitive function, across the entire ageing population (Supplementary Table 2). In patients with AD, lower Li levels in the non-plaque cortical fraction correlated with reduced scores for episodic memory and the index of global cognitive function (Supplementary Table 2).

To further explore the relationship of Li to Aβ, we examined the cortical distribution of endogenous Li in J20 Aβ precursor protein (*App*)-transgenic mice¹³ that exhibit widespread Aβ deposition. LA-ICP-MS showed an approximately 3–4-fold concentration of Li in cortical Aβ deposits in 12-month-old J20 mice relative to adjacent plaque-free cortical regions (Extended Data Fig. 1d). Furthermore, subfractionation of the cortex showed that Li in the non-plaque cortical fraction was significantly reduced in J20 relative to wild-type mice, consistent with Li sequestration by amyloid deposits (Extended Data Fig. 1e). By contrast, 3-month-old J20 mice before the onset of amyloid deposition did not exhibit reduced Li in the soluble cortical fraction relative to age-matched wild-type mice (Extended Data Fig. 1e). Together, these results indicate that Li is sequestered by Aβ deposits, reducing its bioavailability.

Lithium deficiency in mouse models

To explore the biology of endogenous Li, mice were maintained on a chemically defined diet that is calorically and nutritionally equivalent to the typical grain-based mouse diet, including the same Li concentration. Serum and cortical Li levels in mice on this diet were in a similar range to those in the ageing human population, and the mean values were not significantly different (see Methods section on Mouse diet). Selective removal of Li from the mouse diet (a 92% reduction) led to an 89% reduction in mean serum Li and a 47–52% reduction in mean cortical Li in the non-plaque fraction (Extended Data Fig. 2a–c and Supplementary Fig. 2).

The pathological effects of reducing endogenous Li were determined in the 3xTg AD mouse model¹⁴, which accumulates Aβ deposits and phospho-tau, the J20 AD mouse model¹³, which accumulates abundant Aβ deposits, and ageing wild-type mice without AD-type pathology. The 3xTg and J20 mice maintained on the Li-deficient diet showed a significant elevation in Aβ deposition in the hippocampus (Fig. 2a,b). An increased amyloid plaque burden was observed as early as five weeks on the Li-deficient diet and continued to increase with longer-term treatment (Fig. 2a,b and Extended Data Fig. 2d). In ageing wild-type mice, the Li-deficient diet reduced cortical Li by approximately 50% (Extended Data Fig. 2c). This resulted in a significant elevation of cortical and hippocampal Aβ42, the major pathogenic Aβ species in AD, and a trend towards an increase in Aβ40 (Fig. 2c and Extended Data Fig. 2e). Thus, Li deficiency accelerates Aβ deposition

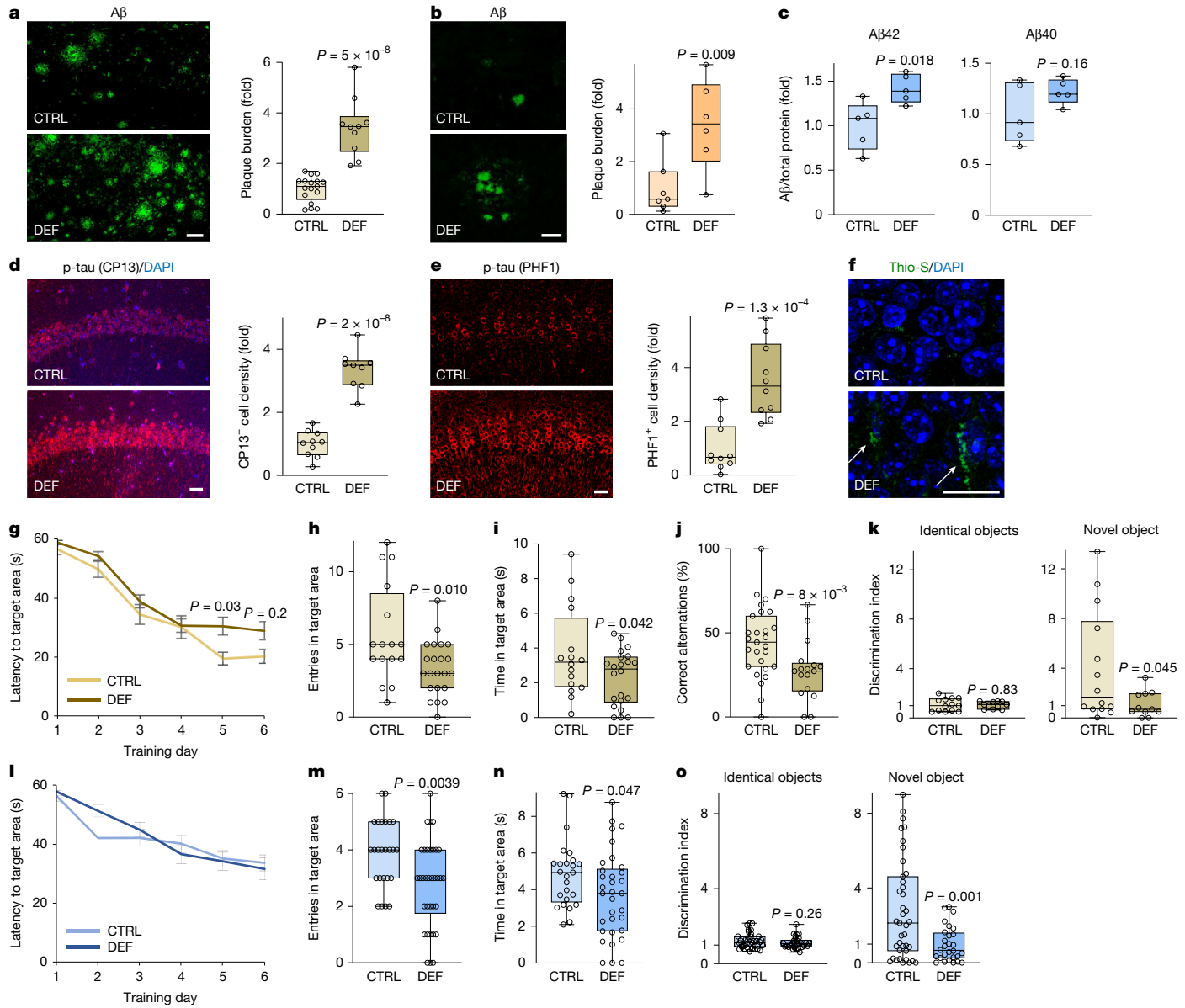


Fig. 2 | Lithium deficiency accelerates AD pathology and cognitive decline. **a,b**, A_β immunolabelling and plaque quantification (right) in the hippocampus of 3xTg (**a**) and J20 (**b**) mice on Li-deficient (DEF) or control (CTRL) diets. **c**, A_β42 and A_β40 levels in the frontal cortex of wild-type (WT) mice on DEF or CTRL diets, normalized to total protein ($n = 5$ per group). **d–f**, Immunolabelling of pSer202-tau (CP13; **d**) or pSer396/Ser404-tau (PHF1; **e**) and thioflavin S labelling (**f**) in the hippocampal CA1 region of 3xTg mice on DEF or CTRL diets, and quantification of phospho-tau-positive cell density (**d–e**, right). In **f**, arrows indicate neurofibrillary tangle-like structures. **g–k**, Behavioural assessment of 3xTg mice on DEF or CTRL diets: Morris water-maze learning (**g**) and memory (**h,i**), Y-maze (**j**) and novel-object recognition (**k**). **l–o**, Behavioural assessment of ageing WT mice on DEF or CTRL diets: Morris water-maze learning (**l**) and memory (**m,n**), and novel-object recognition (**o**). Diets were administered to

in AD mouse models and increases A_β42 levels in ageing wild-type mice.

The role of Li homeostasis in tau pathology was explored in 3xTg mice by assessing the phospho-tau isoforms associated with early (pSer202-tau) and advanced (pSer396/Ser404-tau) stages of neurofibrillary tangle (NFT) formation in AD. Both pSer202-tau and pSer396/Ser404-tau were increased 3–4-fold in hippocampal neurons of Li-deficient 3xTg mice (Fig. 2d,e and Extended Data Fig. 2f,g). A subset of the affected neurons showed elevated phospho-tau in thioflavin

S-positive structures that resemble NFTs (Fig. 2f). As observed for A_β, elevated phospho-tau was evident as early as five weeks into the Li-deficient diet and continued to increase with longer-term treatment (Fig. 2d,e and Extended Data Fig. 2f). These results indicate that Li deficiency promotes neuronal phospho-tau accumulation.

We next assessed whether endogenous Li affects cognitive function in the setting of AD-type pathology and during normal ageing. Administration of the Li-deficient diet to 3xTg mice significantly impaired learning (Fig. 2g) and long-term memory (Fig. 2h,i), as determined in

Article

the Morris water-maze paradigm. There were no significant changes in swimming speed, visible platform recognition or performance in the open-field test, consistent with intact visual perception, locomotor activity and exploratory behaviour (Extended Data Fig. 2h–l). Li deficiency in 3xTg mice also gave rise to significant deficits in the Y-maze and novel-object recognition tests of memory (Fig. 2j,k). Furthermore, ageing Li-deficient wild-type mice also showed significant memory loss in the Morris water maze (Fig. 2m,n) and the novel-object recognition test (Fig. 2o). These cognitive deficits in ageing wild-type mice appeared in the absence of significant changes in spatial learning (Fig. 2l), swimming speed, visible platform recognition or performance in the open-field test (Extended Data Fig. 2m–q). Thus, endogenous Li protects against memory loss in the presence of AD-type pathology, as well as during normal ageing in mice.

The transcriptome of lithium deficiency

We next characterized the effects of Li deficiency on the transcriptome of cell populations in the hippocampus, an early site of disease progression in MCI and AD. Single-nucleus RNA-seq (snRNA-seq) analysis of the hippocampus was done in 3xTg mice after administering the Li-deficient diet for 5 weeks. We analysed 64,772 and 54,374 high-quality nuclei from Li-deficient and control mice, respectively (Supplementary Fig. 3). Based on the expression of previously validated cell-type-specific markers (Supplementary Fig. 4), the relative abundance of the resolved cell types was unchanged after 5 weeks of Li deficiency (Fig. 3a).

Analysis of differentially expressed genes (DEGs) showed significant transcriptome changes in excitatory, granule cell and inhibitory neurons, as well as oligodendrocytes, astrocytes, microglia and oligodendrocyte progenitor cells (OPCs) (Fig. 3b and Supplementary Tables 3 and 4). In excitatory neurons, Gene Ontology (GO) terms for synaptic signalling, organization and transmission were downregulated, whereas electron transport and pathways of neurodegeneration and AD were upregulated (Fig. 3c and Supplementary Tables 5 and 6). Downregulated synaptic genes included *Homer1*, *Grm3*, *Mef2c*, *Lrrk2*, *Grik1*, *Grik3*, *Btbd9*, *Dlgap3* and *Dlgap4* (Fig. 3d). In oligodendrocytes, GO terms for axon ensheathment and myelination, as well as neuron projection development, were strongly downregulated (Fig. 3c and Supplementary Tables 5 and 6). Downregulated myelin-related genes included *Mbp*, *Mog*, *Mag*, *Plp1* and *Opalin* (Fig. 3d). In astrocytes, pathways of neurodegeneration, electron transport chain and monovalent cation transport were upregulated (Supplementary Fig. 5 and Supplementary Tables 5 and 6). Proteomic analysis of the hippocampus in Li-deficient 3xTg mice showed significantly reduced abundance of synaptic and myelin protein components and increased abundance of proteins involved in neuroinflammation, lipid metabolism and mitochondrial membrane organization (Supplementary Fig. 6 and Supplementary Table 7). These results indicate that endogenous Li broadly affects the composition of the brain transcriptome and proteome.

We next investigated whether the transcriptome of Li deficiency overlapped with that of AD by comparing our findings with a recent snRNA-seq study of cortical biopsy samples from living individuals with a range of AD pathology¹⁵. Samples from the human biopsy study that exhibited early stage Aβ deposition showed cell-type-specific overlap of DEGs with 3xTg mice on a Li-deficient diet (Fig. 3e). Concordant DEGs included both upregulated and downregulated genes in excitatory and inhibitory neurons, upregulated genes in microglia and OPCs, and downregulated genes in oligodendrocytes (Fig. 3e and Supplementary Table 8). Overlap with Li-deficient DEGs was more extensive in human cortical samples with both Aβ and phospho-tau pathology that were diagnosed with AD before or within one year of biopsy¹⁵ (Fig. 3e). Concordant DEGs included both upregulated and downregulated genes in excitatory and inhibitory neurons, microglia and oligodendrocytes, and upregulated genes in astrocytes, endothelial cells and OPCs (Fig. 3e

and Supplementary Table 8). Thus, the transcriptome of Li deficiency broadly overlaps with the transcriptome of AD pathology in humans.

Maintenance of synapses and myelin

Genes involved in synaptic signalling and structure were broadly downregulated by Li deficiency (Fig. 3c). Dendritic spine loss was detected by Golgi staining in Li-deficient 3xTg and wild-type mice (Fig. 3f and Extended Data Fig. 3a,b), together with reduced immunolabelling of the presynaptic and postsynaptic proteins synaptophysin and PSD-95, respectively (Fig. 3g,h). Reduced abundance of synaptic proteins was confirmed by proteomic analysis of the Li-deficient 3xTg hippocampus (Supplementary Fig. 6a,b and Supplementary Table 7). Thus, endogenous Li contributes to synapse maintenance in the ageing mouse brain.

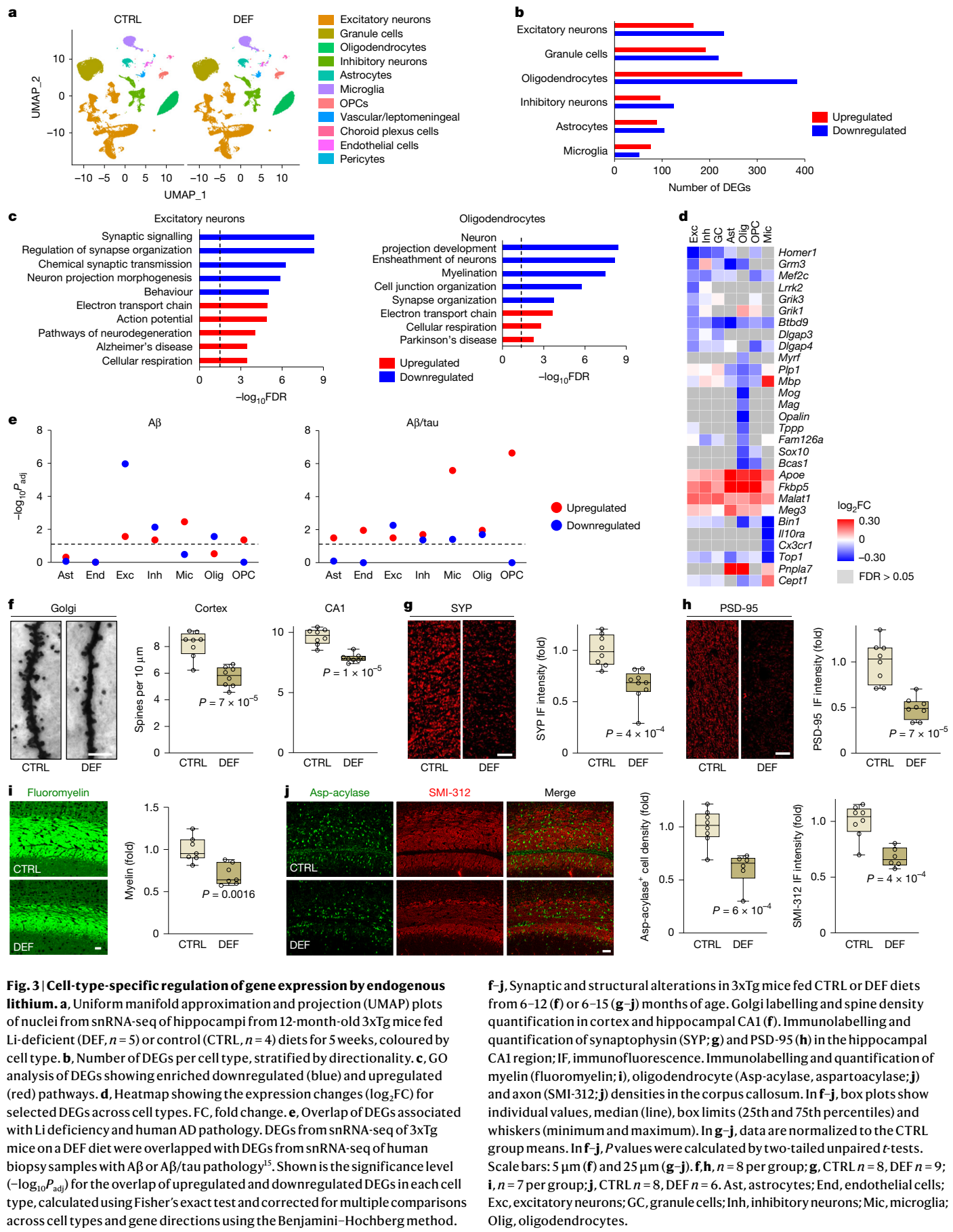
Li deficiency downregulated the expression of myelin-related genes in oligodendrocytes and reduced the abundance of myelin-associated proteins (Fig. 3c,d and Supplementary Fig. 6b). Fluoromyelin labelling indicated a significant loss of myelin in 3xTg mice after long-term Li deficiency (Fig. 3i). This was associated with reduced numbers of oligodendrocytes, OPCs and axons in Li-deficient 3xTg and wild-type mice (Fig. 3j and Extended Data Fig. 3c,d). To assess myelin ultrastructure, transmission electron microscopy was performed on the corpus callosum in Li-deficient and control 3xTg mice (Extended Data Fig. 3e). Li-deficient mice had thinner electron-dense myelin sheaths surrounding neuronal axons and a significantly elevated g-ratio (the ratio of the inner axonal diameter to the total axon plus myelin fibre diameter), consistent with reduced axonal myelin. These results indicate that endogenous lithium contributes to the maintenance of myelin integrity.

Lithium and microglial function

The snRNA-seq analysis of Li deficiency showed a reduction in the number of microglia expressing the gene *Cx3cr1*, which encodes a homeostatic marker, and an increase in microglia expressing *Apoe* (Supplementary Fig. 7a), similar to the reactive microglial state observed in AD¹⁵. To obtain greater insight into the regulation of microglia by Li, viable microglia were isolated from the brain and analysed by deep RNA sequencing. Isolated microglia showed a high degree of purity and did not exhibit stress-related markers¹⁶ (Supplementary Fig. 7b,c). RNA sequencing showed major transcriptome changes in microglia associated with Li deficiency in both 3xTg and wild-type mice with highly significant overlap (Supplementary Tables 9–12). Genes upregulated by Li deficiency in 3xTg and wild-type microglia were enriched in GO terms corresponding to AD and pathways of neurodegeneration, electron transport chain and respiration, regulation of amyloid fibril formation, translation and oxidative stress. Genes downregulated by Li deficiency were enriched in the GO terms DNA damage response, cellular response to stress, import into cell and protein catabolic process (Fig. 4a,b and Supplementary Table 12).

Transcriptome changes in Li-deficient wild-type microglia were enriched for many risk genes for AD identified in genome-wide association studies (GWAS)¹⁷, including *Apoe*, *Trem2*, *Bin1*, *Clu*, *Picalm*, *Cd33*, *H2-Eb1* (*HLA-DRB1* orthologue), *Inpp5d*, *Abca1*, *Abca7* and *Adam10* (Multi-marker Analysis of GenoMic Annotation (MAGMA), false discovery rate (FDR) < 0.05). We also observed significant overlap of the transcriptome signature of Li-deficient microglia with that of microglia in AD, particularly for microglia that express glycoprotein NMB (GPNMB) ($P < 10^{-21}$ for 3xTg and $P < 10^{-14}$ for wild type), which expand with the progression of AD¹⁵. Furthermore, GPNMB expression was significantly upregulated in Li-deficient microglia (Supplementary Table 11). Thus, Li deficiency alters the microglial transcriptome in a manner that overlaps with AD.

We next examined reactive changes in microglia following Li deficiency. Immunolabelling showed that Li deficiency increased CD68-immunoreactive microglia in 3xTg mice (Fig. 4b) and elevated



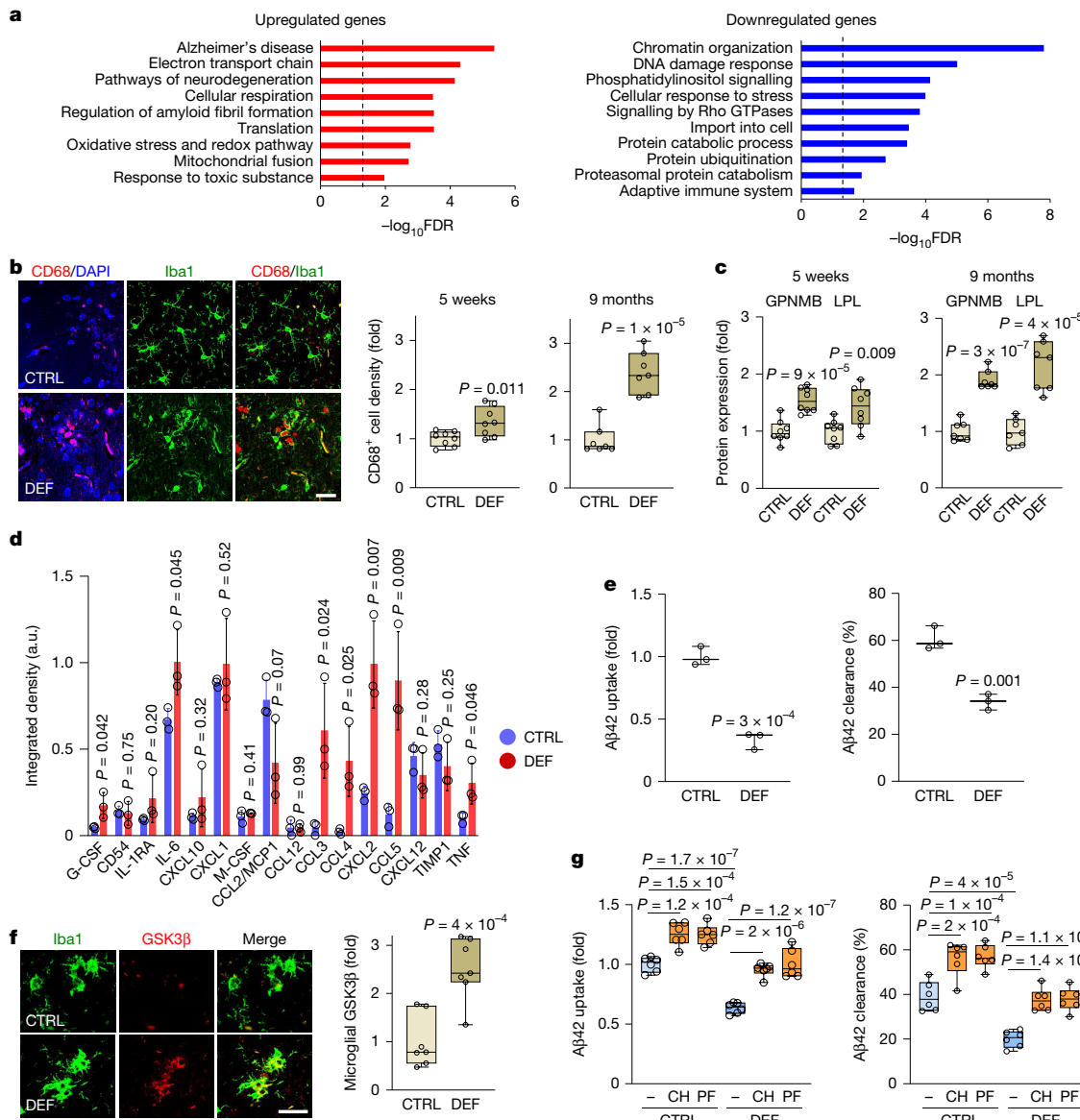


Fig. 4 | Lithium deficiency activates microglia and impairs Aβ clearance. **a**, GO analysis of DEGs shared between Li-deficient (DEF) 3xTg (treatment from 5 to 9 months of age; $n = 4$ mice per group) and wild-type (WT; treatment from 12 to 20 months of age; $n = 4$ per group) microglia. **b, c**, 3xTg mice were fed a DEF or CTRL diet for either 5 weeks (starting at 10.8 months of age; $n = 8$ per group) or 9 months (starting at 6 months of age; $n = 7$ per group). Immunolabelling (**b**, left) of total (Iba1) and activated (CD68) microglia in the hippocampus (9-month treatment). Quantification of CD68⁺ cell density (**b**, right) and GPNMB and LPL microglial expression (**c**) in the hippocampus. **d**, Cytokine levels in culture medium of primary cortical microglia isolated from WT mice on CTRL or DEF diets from 12 to 18 months of age ($n = 3$ per group), after stimulation with 50 ng ml⁻¹ LPS. Signals were normalized to internal controls from the cytokine array. Data are mean \pm s.d. a.u., arbitrary units. **e**, Aβ42

uptake (left) and degradation (right) by primary cortical microglia isolated from 18-month-old WT mice after 6 months on CTRL or DEF diets ($n = 3$ per group). **f**, Immunolabelling (left) and quantification (right) of GSK3β in Iba1⁺ microglia in the hippocampus of 3xTg mice after 9 months on CTRL or DEF diets ($n = 7$ per group). **g**, Aβ42 uptake (left) and degradation (right) by primary microglia isolated from WT mice fed CTRL or DEF diets from 12 to 16 months of age, and then incubated in culture with the GSK3β inhibitors CHIR99021 (CH) or PF-04802367 (PF) ($n = 6$ biological replicates per group). In **b–g**, data were normalized to the mean of CTRL groups. In **b, c, e–g**, box plots show individual values, median (line), box limits (25th and 75th percentiles) and whiskers (minimum and maximum). *P* values calculated by unpaired two-tailed *t*-tests (**a–f**) or two-way ANOVA with Tukey's post-hoc test (**g**). Scale bars, 20 μm.

microglial protein expression of GPNMB and lipoprotein lipase (LPL), which are markers of microglial reactivity in AD¹⁵ (Fig. 4c). Li deficiency also increased the density of CD68⁺ reactive microglia in a second transgenic AD mouse model, J20 (Supplementary Fig. 7d). To explore functional changes, isolated microglia were stimulated in culture with lipopolysaccharide (LPS). Microglia from Li-deficient wild-type mice showed elevated release of the pro-inflammatory cytokines IL-6, TNF and G-CSF, as well as the immune activating chemokines CCL3, CCL4, CCL5 and CXCL2 (Fig. 4d). Finally, microglia isolated from Li-deficient

wild-type mice showed significantly reduced Aβ42 uptake and subsequent degradation of Aβ42 relative to microglia from control mice (Fig. 4e). Thus, Li deficiency leads to a reactive pro-inflammatory state and impaired Aβ clearance.

GSK3β regulation by endogenous lithium

We next identified signalling pathways that are altered by Li deficiency using Ingenuity/IPA network analysis of DEGs. Wnt-β-catenin

signalling was significantly affected and was predicted to be repressed in microglia, excitatory neurons and oligodendrocytes (Extended Data Fig. 4a–c). Immunolabelling showed significantly reduced nuclear β-catenin levels in Li-deficient hippocampal CA1 neurons in 3xTg and wild-type mice (Extended Data Fig. 5a,b). Nuclear β-catenin levels were also reduced in Li-deficient oligodendrocytes and microglia (Extended Data Fig. 5c,d).

A central regulator of β-catenin signalling is the serine-threonine kinase GSK3β, which phosphorylates β-catenin, targeting it for proteasomal degradation. Another GSK3β substrate is tau, which is phosphorylated by GSK3β in AD^{18–21} and showed 3–4-fold elevated phosphorylation in Li-deficient 3xTg mice (Fig. 2d,e). Li deficiency elevated total GSK3β levels in hippocampal CA1 neurons, oligodendrocytes and microglia in 3xTg mice (Fig. 4f and Extended Data Fig. 5e,f). Elevated total GSK3β protein was confirmed by proteomic analysis of the hippocampus in Li-deficient mice (Supplementary Table 7). GSK3β mRNA was also elevated by Li deficiency (Extended Data Fig. 5g), consistent with increased GSK3β expression.

GSK3β is activated by autophosphorylation of tyrosine 216, which is increased in AD^{18,21}. The levels of pTyr216-GSK3β were significantly elevated by Li deficiency in hippocampal CA1 neurons and oligodendrocytes in 3xTg and wild-type mice (Extended Data Fig. 5h,i). Phosphorylation of GSK3β at Ser9, which inhibits GSK3β activity, did not change in absolute level, but the ratio of pSer9:total GSK3β was reduced, consistent with elevated GSK3β activity (Extended Data Fig. 5j,k). By contrast, the level of inositol, which is modulated by Li at pharmacological concentrations through inositol monophosphatase²², was not altered by endogenous Li deficiency (Extended Data Fig. 5l).

To assess the role of GSK3β in the pathogenic effects of Li deficiency, the GSK3β inhibitor CHIR99021 was administered to Li-deficient 3xTg mice. Treatment with CHIR99021 reversed the Li deficiency-associated activation of microglia (Extended Data Fig. 6a) and normalized the levels of multiple pro-inflammatory cytokines and chemokines (Extended Data Fig. 6b). Furthermore, incubation of primary microglia from Li-deficient wild-type mice with CHIR99021 resulted in the restoration of Aβ42 uptake and degradation (Fig. 4g). A similar outcome was achieved using a second GSK3β inhibitor, PF-04802367 (Fig. 4g). Moreover, treatment of Li-deficient 3xTg mice with CHIR99021 reversed the elevated Aβ deposition and tau phosphorylation and restored oligodendrocyte cell number and expression of myelin basic protein (MBP) (Extended Data Fig. 6c–e). Thus, GSK3β activation contributes to a broad range of pathology associated with Li deficiency.

Lithium replacement therapy

The observation that Li is sequestered by amyloid deposits in MCI and AD prompted a search for therapeutic Li salts with reduced amyloid binding. We reasoned that the electrostatic interaction of the Li ion with Aβ deposits would be a function of the ionization capacity of the salt, and that Li salts with reduced ionization might show reduced amyloid sequestration. To assess ionization directly, we measured the conductivity of 16 lithium salts. Inorganic Li salts, including the clinical standard lithium carbonate (Li_2CO_3 , hereafter LiC), showed significantly elevated conductivity, indicative of increased ionization, relative to organic Li salts ($P = 8 \times 10^{-4}$; Fig. 5a and Extended Data Fig. 7a). Of the organic Li salts, lithium orotate ($\text{C}_5\text{H}_3\text{LiN}_2\text{O}_4$, hereafter LiO) showed the lowest conductance across a broad Li concentration range (Fig. 5a and Extended Data Fig. 7a) and was therefore selected for further comparison with the clinical standard LiC.

We next investigated whether conductivity predicts Li binding to the aggregated forms of Aβ that accumulate in AD. Equilibrium dialysis binding assays demonstrated that Li binds to both fibrils and oligomers formed from synthetic human Aβ1–42 in vitro (Fig. 5b,c and Extended Data Fig. 7b). Li binding was saturable and occurred in a high-affinity range that included the physiological concentration range of Li in brain

and serum (0–2 $\mu\text{Eq l}^{-1}$), as well as a lower-affinity range corresponding to clinical pharmacological doses. Notably, LiC exhibited higher binding affinity than LiO for both Aβ42 fibrils and oligomers across a broad Li concentration range (Fig. 5b,c and Supplementary Table 13).

To further explore the Li–Aβ interaction in vivo, LiO and LiC were administered to J20 and 3xTg mice at a low dose in the drinking water (4.3 $\mu\text{Eq l}^{-1}$ Li), resulting in a serum Li level in the physiological concentration range observed in ageing humans and mice (Supplementary Fig. 8a,c,d, Extended Data Fig. 1c and Methods). Serum and hippocampal Li levels were not significantly different after administration of low-dose LiO or LiC (Supplementary Fig. 8a,b). However, Li was highly concentrated in Aβ plaques after the administration of LiC, but to a much smaller extent after administration of LiO in both 3xTg and J20 mice (Extended Data Fig. 7c,d). Moreover, LiO, but not LiC, significantly elevated parenchymal Li in the non-plaque fraction in 3xTg and J20 mice (Extended Data Fig. 7e,f). Thus, LiO shows reduced amyloid sequestration relative to LiC and more effectively elevates non-plaque Li in the brain.

When LiO was administered to adult 3xTg mice, the physiological dose almost completely prevented Aβ plaque deposition and phospho-tau accumulation; by contrast, administration of LiC or the sodium orotate control had no significant effect (Extended Data Fig. 8a,b). We next investigated whether LiO could reverse more-advanced pathology in ageing mice. Administration of LiO to 3xTg mice from 9 to 18 months of age significantly reduced the Aβ plaque burden and the density of phospho-tau-positive NFT-like structures in the hippocampus, whereas LiC had no significant effect at the same dose (Fig. 5d). LiO also reduced the Aβ plaque burden by about 70% in older J20 mice with abundant and widespread Aβ deposition (Fig. 5e). Thus, LiO is highly effective at reducing Aβ deposition and phospho-tau accumulation.

LiO, but not LiC, increased the expression of the synaptic marker PSD-95 (Extended Data Fig. 8c), increased myelin-associated MBP immunoreactivity and elevated oligodendrocyte cell number (Extended Data Fig. 8d,e). LiO was also more effective than LiC in suppressing microgliosis and astrogliosis in aged 3xTg mice (Extended Data Fig. 8f,g). Administration of low-dose LiO, but not LiC, also reduced total GSK3β levels in hippocampal CA1 neurons and white matter (Extended Data Fig. 9a,b), reduced the level of activated pTyr216-GSK3β (Extended Data Fig. 9c) and elevated nuclear β-catenin (Extended Data Fig. 9d).

RNA-seq analysis of the hippocampus of LiO-treated 3xTg mice showed downregulation of genes corresponding to the GO terms translation, electron transport chain, pathways of neurodegeneration, Alzheimer's disease, β-catenin degradation and interleukin-1 signalling, and upregulation of genes corresponding to the GO terms synapse organization and signalling, neuron projection morphogenesis and learning or memory (Fig. 5f and Supplementary Tables 14 and 15). These GO terms are similar to those associated with Li deficiency but with opposite directionality of change (Figs. 3c and 4a).

The effects of LiO on genes involved in learning and memory prompted us to explore cognitive function in 3xTg mice, which show memory loss relative to wild-type mice (Fig. 5g). LiO at the lowest dose (4.3 $\mu\text{Eq l}^{-1}$) almost completely reversed the memory loss, whereas LiC and the sodium orotate control did not show significant effects (Fig. 5g). Furthermore, LiO improved learning and spatial memory in ageing J20 mice with advanced amyloid pathology (Extended Data Fig. 10a–c). LiO did not significantly affect swimming speed, visual platform localization or locomotor performance in the open-field test (Extended Data Fig. 10d–h and Supplementary Fig. 9a–f). Thus, LiO suppresses AD-type pathology, neuroinflammation and synapse loss, and restores memory.

Lithium and brain ageing

To explore the effects of Li on normal brain ageing, low-dose LiO (4.3 $\mu\text{Eq l}^{-1}$ Li) was administered to wild-type mice from 12 to 24 months of age. This resulted in a modest elevation of mean serum and cortical

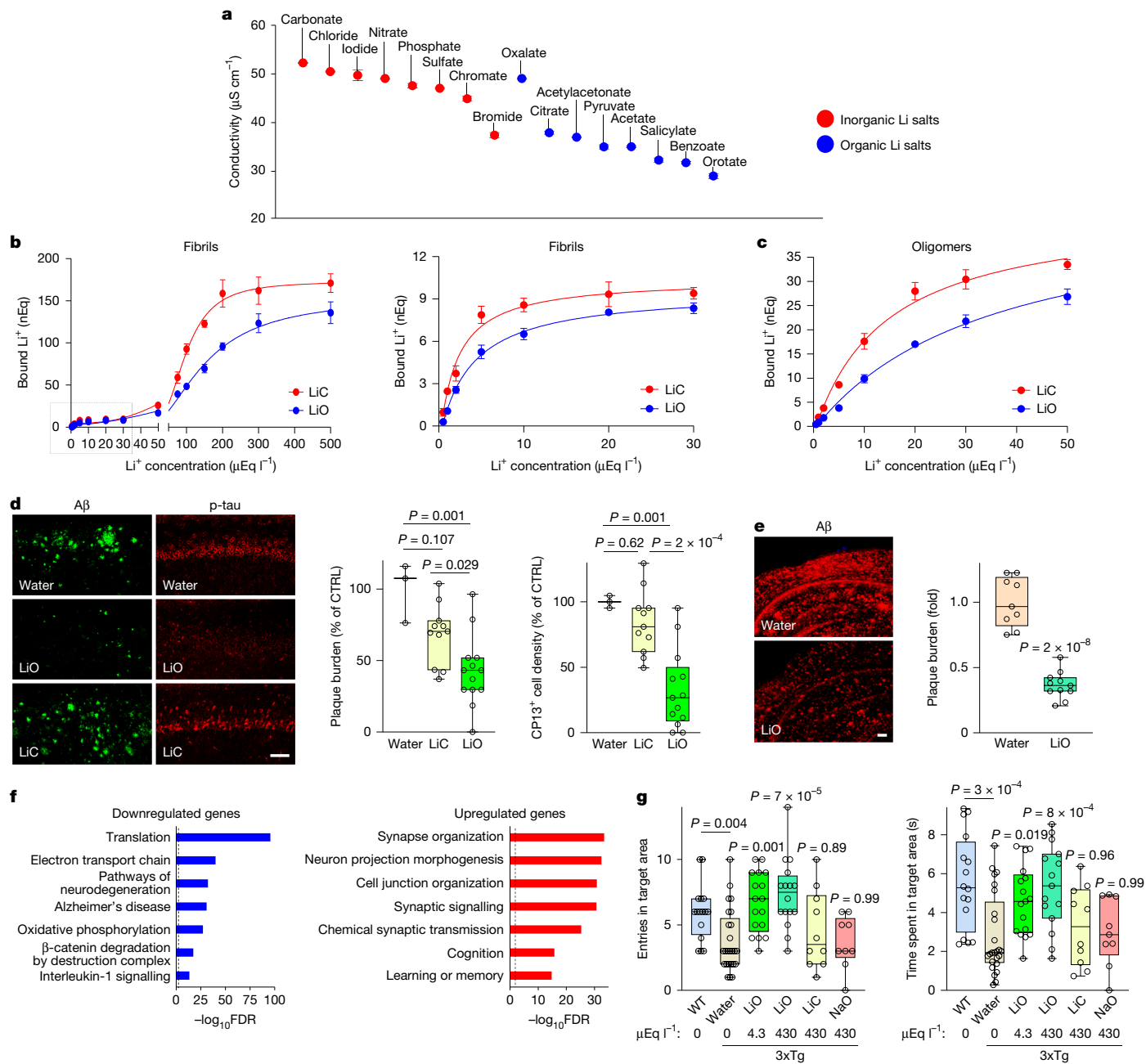


Fig. 5 | Therapeutic efficacy of a plaque-evasive lithium salt. **a**, Organic Li salt solutions exhibit lower conductivity than inorganic Li salts. All solutions contained $430 \mu\text{Eq l}^{-1}$ Li. **b,c**, Li binds to human A β 1–42 fibrils (**b**) and oligomers (**c**). Binding curves are shown for all tested concentrations (**b**, left) and the 0 – $30 \mu\text{Eq l}^{-1}$ range (**b**, right). LiC shows higher affinity than LiO (EC₅₀ values and 95% confidence intervals are in Supplementary Table 13). **d**, Immunolabelling of A β and pSer202-tau in the hippocampus (left) and quantification of plaque burden (middle) and pSer202-tau⁺ cell density (right) in 3xTg mice treated with LiO or LiC ($4.3 \mu\text{Eq l}^{-1}$) from 9 to 18 months of age (vehicle $n = 3$, LiC $n = 11$, LiO $n = 13$). **e**, A β immunolabelling (left) and quantification (right) in J20 mice treated with LiO ($4.3 \mu\text{Eq l}^{-1}$) from 17 to 22 months of age (water $n = 9$, LiO $n = 11$). **f**, GO analysis of DEGs from RNA-seq analysis of the hippocampus of 3xTg mice

treated with LiO ($4.3 \mu\text{Eq l}^{-1}$) or vehicle from 6 to 12 months of age ($n = 9$ per group). **g**, Memory retrieval in the Morris water maze for 3xTg mice treated from 5 to 12 months of age; WT mice (12 months) served as controls. WT $n = 16$, 3xTg $n = 25$, LiO $4.3 n = 17$, LiO $430 n = 16$ (left), $n = 15$ (right), LiC $n = 10$, NaO $n = 9$. In **d,e**, data were normalized to the mean for the water vehicle. In **a–c**, mean \pm s.d. values are shown from $n = 3$ independent solution replicates (**a**) or $n = 3$ biological replicates (**b,c**). In **d,e,g**, box plots show individual values, median (line), box limits (25th and 75th percentiles) and whiskers (minimum and maximum). In **d,e**, *P* values were calculated by one-way ANOVA with Tukey's post-hoc test. In **g**, WT and 3xTg (water) groups were compared using a preplanned unpaired two-tailed *t*-test; all other *P* values were derived from one-way ANOVA with Dunnett's post-hoc comparisons to the 3xTg (water) control. Scale bars, $50 \mu\text{m}$.

Li levels that overlap with the range of endogenous Li in untreated mice (Supplementary Fig. 10a). LiO almost completely prevented age-related microgliosis and astrogliosis in the hippocampus, cortex and corpus callosum (Extended Data Fig. 11a,b). Moreover, LiO reduced the age-related production of the pro-inflammatory cytokines IL-6 and IL-1 β (Extended Data Fig. 12a).

Microglia isolated from aged mice showed a marked reduction in the ability to degrade A β 42 relative to microglia from young adult mice. Treatment with LiO in vivo reversed this age-related loss of A β degradative capacity (Extended Data Fig. 12b). Similar results were obtained by incubating microglial BV2 cells with LiO in culture. LiO significantly elevated A β 42 uptake and degradation in BV2 cells, whereas the control

sodium orotate had no significant effect (Extended Data Fig. 12c–e). Thus, LiO reduces age-related neuroinflammatory changes and restores the ability of microglia to clear A β .

Synapse loss and cognitive decline are characteristic features of brain ageing in mice. Administration of LiO to wild-type mice prevented age-related loss of dendritic spines in CA1 and CA3 hippocampal neurons, whereas the control salt NaO had no significant effect (Supplementary Fig. 10b). Importantly, the decline in learning and memory associated with ageing was largely reversed by LiO, as determined by tests in the Morris water maze (Extended Data Fig. 13a,b). LiO did not affect swimming speed or localization of a visible platform (Extended Data Fig. 13c,d). LiO also prevented age-related decline in novel-object recognition memory (Extended Data Fig. 13e). Notably, long-term administration of LiO to ageing wild-type, 3xTg or J20 mice did not alter serum levels of blood urea nitrogen, creatinine or thyroid-stimulating hormone (TSH) (Supplementary Fig. 11). Thus, low dose LiO prevents age-related pro-inflammatory changes, synapse loss and cognitive decline in mice without evidence of toxicity.

These observations prompted an examination of endogenous brain Li and cognitive resilience in normal ageing humans. Expression levels of the presynaptic proteins complexin 1 and 2, which regulate synaptic vesicle exocytosis, predict resistance to AD^{23,24}. Complexin 1 and 2 expression showed a highly significant positive correlation with Li cortex-to-serum ratio in aged individuals without MCI or AD (Extended Data Fig. 13f). Furthermore, cortical Li was positively correlated with cognitive test scores for working memory ($P = 0.04$) and performance on the Mini Mental State Examination (MMSE; $P = 0.02$). Together, these results in normal ageing mice and humans indicate that Li homeostasis may contribute to cognitive resilience.

Discussion

These observations indicate a physiological role for endogenous Li that affects brain ageing and vulnerability to AD. In humans, Li is used in psychiatry for the treatment of bipolar disorder at a dose range that raises levels in serum to approximately 1,000 times the endogenous level. We found that in normal ageing mice, low micromolar levels of endogenous Li preserve cognitive function, reduce inflammation and suppress A β generation. In AD mouse models, endogenous Li protects against amyloid deposition, tau hyperphosphorylation, neuroinflammation and loss of synapses, axons and myelin. These effects are mediated, at least in part, through repression of the kinase GSK3 β in multiple cell types in the brain.

Metalomic profiling of the brain also uncovered alterations in other metals that have been previously observed in AD, such as increased sodium²⁵ and zinc²⁶ and reduced copper¹². However, decreased cortical Li was the only statistically significant metal alteration observed in both MCI and AD in our dataset. This observation is consistent with a population study in Denmark that found a significant inverse correlation between Li levels in local drinking water and the incidence of dementia²⁷. We were able to recapitulate the reduced Li levels observed in humans with AD in mouse models with a Li-deficient diet. snRNA-seq showed that reduced cortical Li significantly alters the transcriptome of the major brain cell types. Furthermore, DEGs associated with Li deficiency in the mouse models overlapped with DEGs previously identified in snRNA-seq of human brain biopsy samples with AD pathology¹⁵. Overlapping DEGs were enriched in microglia, excitatory and inhibitory neurons, OPCs, oligodendrocytes, endothelial cells and astrocytes. Consistent with these transcriptome alterations, Li deficiency resulted in deleterious effects on neurons, microglia and oligodendrocytes with loss of synapses and axons, impaired A β clearance and reduced myelination.

Li deficiency altered microglial expression of some of the most penetrant risk-factor genes identified in GWAS studies of AD, including *Apoe*, *Trem2*, *Bin1*, *Picalm*, *Clu*, *Cd33* and the mouse orthologues

of human *MS4A6A*¹⁷. These expression changes were associated with elevated markers of microglial activation such as CD68, as well as increased production of multiple pro-inflammatory cytokines and chemokines that are also elevated in AD²⁸. Furthermore, Li deficiency impaired the ability of microglia to phagocytose and degrade A β , a phenotype that has been linked to A β deposition in AD²⁹. These findings indicate that endogenous Li maintains microglial homeostatic function and prevents pro-inflammatory changes associated with AD.

One of the first molecular targets of Li to be characterized at pharmacological doses was the kinase GSK3 β ³⁰. GSK3 β activity is increased in AD and has been implicated in A β and tau pathology^{18,20,21,31}. Moreover, the GSK3 β substrate β -catenin is reduced in AD^{18,32,33}. The reported IC₅₀ of the Li-GSK3 β interaction in vitro is in the millimolar range³⁰, making this a seemingly unlikely interaction at the low micromolar concentration range of endogenous Li in the brain. However, our findings indicate that GSK3 β activation and expression are elevated by endogenous Li deficiency. Moreover, GSK3 β inhibitors can reverse many of the pathological consequences of Li deficiency, including A β deposition, phospho-tau accumulation, myelination and microglial pro-inflammatory activation, as well as restoring the ability of microglia to clear A β . Previous reports have shown that GSK3 β activation can promote cytokine production in monocytic and microglial cells³⁴ and impair oligodendrocyte differentiation and myelination by inhibiting β -catenin signalling³⁵. Together, our findings implicate increased GSK3 β activity in the multisystem effects of Li deficiency in the brain.

Treatment with Li at pharmacologic doses has been shown to reduce A β ^{33,36–45} and tau^{37,38,43,46–49} pathology in various neurodegenerative disease models. Similarly, Li prevented or reversed cognitive decline in several studies^{36–39,43,44}, but not in one short-term study⁴⁷. More direct evidence for a therapeutic role of Li in AD emerged from several small clinical trials. In two initial trials^{50,51}, Li treatment did not improve cognitive function, but in three subsequent trials, Li at lower concentrations (0.25–0.5 mEq l⁻¹ in serum) reduced cognitive decline^{52–55}. A limitation of these clinical trials might have been the use of Li salts with high levels of amyloid binding. We have characterized a Li salt, lithium orotate, with reduced binding that can bypass amyloid sequestration in AD mouse models. Treatment with LiO at a dose that maintains serum and cortical Li levels in the endogenous range prevents and reverses AD pathology, neuroinflammatory changes and memory loss in AD mouse models and ageing wild-type mice. An important limitation in the treatment of aged individuals with pharmacological doses of lithium is kidney and thyroid toxicity⁵⁶. It is encouraging that toxicity could not be detected following long-term treatment of ageing mice with a low dose of LiO.

Disruption of Li homeostasis may contribute to the long prodromal period of neuropathological changes that occur prior to the onset of clinical AD. Our findings indicate that sequestration of Li by amyloid depletes Li in affected brain regions. Li depletion can, in turn, impair microglial clearance of A β , which would accelerate amyloid pathology in a positive feedback loop. In parallel, Li deficiency may promote phospho-tau accumulation, inflammation and the loss of synapses, axons and myelin. The progression of this neurodegenerative process may be modulated by genetic risk variants^{17,57}, as well as environmental factors and dietary Li intake. Li deficiency is therefore a potential common mechanism for the multisystem degeneration of the brain that leads to the onset of AD.

Online content

Any methods, additional references, Nature Portfolio reporting summaries, source data, extended data, supplementary information, acknowledgements, peer review information; details of author contributions and competing interests; and statements of data and code availability are available at <https://doi.org/10.1038/s41586-025-09335-x>.

1. James, B. D. & Bennett, D. A. Causes and patterns of dementia: an update in the era of redefining Alzheimer's disease. *Annu. Rev. Public Health* **40**, 65–84 (2019).
2. Sperling, R., Mormino, E. & Johnson, K. The evolution of preclinical Alzheimer's disease: implications for prevention trials. *Neuron* **84**, 608–622 (2014).
3. De Strooper, B. & Karvan, E. The cellular phase of Alzheimer's disease. *Cell* **164**, 603–615 (2016).
4. Murdock, M. H. & Tsai, L.-H. Insights into Alzheimer's disease from single-cell genomic approaches. *Nat. Neurosci.* **26**, 181–195 (2023).
5. Mathys, H. et al. Single-cell multiregion dissection of Alzheimer's disease. *Nature* <https://doi.org/10.1038/s41586-024-07606-7> (2024).
6. Migliore, L. & Coppedè, F. Gene-environment interactions in Alzheimer disease: the emerging role of epigenetics. *Nat. Rev. Neurol.* **18**, 643–660 (2022).
7. Killin, L. O. J., Starr, J. M., Shue, I. J. & Russ, T. C. Environmental risk factors for dementia: a systematic review. *BMC Geriatr.* **16**, 175 (2016).
8. Kawahara, M., Kato-Negishi, M. & Tanaka, K. Cross talk between neurometals and amyloidogenic proteins at the synapse and the pathogenesis of neurodegenerative diseases. *Metalomics* **9**, 619–633 (2017).
9. Huat, T. J. et al. Metal toxicity links to Alzheimer's disease and neuroinflammation. *J. Mol. Biol.* **431**, 1843–1868 (2019).
10. Bakulski, K. M. et al. Heavy metals exposure and Alzheimer's disease and related dementias. *J. Alzheimers Dis.* **76**, 1215–1242 (2020).
11. Bush, A. I. et al. Rapid induction of Alzheimer A β amyloid formation by zinc. *Science* **265**, 1464–1467 (1994).
12. James, S. A. et al. Elevated labile Cu is associated with oxidative pathology in Alzheimer disease. *Free Radic. Biol. Med.* **52**, 298–302 (2012).
13. Mucke, L. et al. High-level neuronal expression of A β ₁₋₄₂ in wild-type human amyloid protein precursor transgenic mice: synaptotoxicity without plaque formation. *J. Neurosci.* **20**, 4050–4058 (2000).
14. Oddo, S. et al. Triple-transgenic model of Alzheimer's disease with plaques and tangles: intracellular A β and synaptic dysfunction. *Neuron* **39**, 409–421 (2003).
15. Gazestani, V. et al. Early Alzheimer's disease pathology in human cortex involves transient cell states. *Cell* **186**, 4438–4453 (2023).
16. Herron, S., Delpach, J.-C., Madore, C. & Ikezu, T. Using mechanical homogenization to isolate microglia from mouse brain tissue to preserve transcriptomic integrity. *STAR Protoc.* **3**, 101670 (2022).
17. Kunkle, B. W. et al. Genetic meta-analysis of diagnosed Alzheimer's disease identifies new risk loci and implicates A β , tau, immunity and lipid processing. *Nat. Genet.* **51**, 414–430 (2019).
18. Folke, J., Pakkenberg, B. & Brudek, T. Impaired Wnt signaling in the prefrontal cortex of Alzheimer's disease. *Mol. Neurobiol.* **56**, 873–891 (2019).
19. Lauretti, E., Dincer, O. & Praticò, D. Glycogen synthase kinase-3 signaling in Alzheimer's disease. *Biochim. Biophys. Acta Mol. Cell. Res.* **1867**, 118664 (2020).
20. Leroy, K. et al. The active form of glycogen synthase kinase-3 β is associated with granulovacuolar degeneration in neurons in Alzheimer's disease. *Acta Neuropathol.* **103**, 91–99 (2002).
21. Leroy, K., Yilmaz, Z. & Brion, J.-P. Increased level of active GSK-3 β in Alzheimer's disease and accumulation in argyrophilic grains and in neurones at different stages of neurofibrillary degeneration. *Neuropathol. Appl. Neuropatol.* **33**, 43–55 (2007).
22. Guillot, S., Gauthier, S., Touchon, J. & Soto, M. E. Lithium, a treatment option for Alzheimer's disease? A review of existing evidence and discussion on future perspectives. *J. Alzheimers Dis.* **96**, 473–482 (2023).
23. Yu, L. et al. Cortical proteins associated with cognitive resilience in community-dwelling older persons. *JAMA Psychiatry* **77**, 1172–1180 (2020).
24. Ramos-Miguel, A. et al. Presynaptic proteins complexin-I and complexin-II differentially influence cognitive function in early and late stages of Alzheimer's disease. *Acta Neuropathol.* **133**, 395–407 (2017).
25. Graham, S. F. et al. Quantitative measurement of [Na $^+$] and [K $^+$] in postmortem human brain tissue indicates disturbances in subjects with Alzheimer's disease and dementia with Lewy bodies. *J. Alzheimers Dis.* **44**, 851–857 (2015).
26. Religa, D. et al. Elevated cortical zinc in Alzheimer disease. *Neurology* **67**, 69–75 (2006).
27. Kessing, L. V. et al. Association of lithium in drinking water with the incidence of dementia. *JAMA Psychiatry* **74**, 1005–1010 (2017).
28. Heneka, M. T. et al. Neuroinflammation in Alzheimer's disease. *Lancet Neurol.* **14**, 388–405 (2015).
29. Romero-Molina, C., Garretti, F., Andrews, S. J., Marcora, E. & Goate, A. M. Microglial efferocytosis: diving into the Alzheimer's disease gene pool. *Neuron* **110**, 3513–3533 (2022).
30. Klein, P. S. & Melton, D. A. A molecular mechanism for the effect of lithium on development. *Proc. Natl Acad. Sci. USA* **93**, 8455–8459 (1996).
31. Sofola, O. et al. Inhibition of GSK-3 ameliorates A β pathology in an adult-onset *Drosophila* model of Alzheimer's disease. *PLoS Genet.* **6**, e1001087 (2010).
32. Aghaizu, N. D., Jin, H. & Whiting, P. J. Dysregulated Wnt signalling in the Alzheimer's brain. *Brain Sci.* **10**, 902 (2020).
33. Liu, C.-C. et al. Deficiency in LRP6-mediated Wnt signalling contributes to synaptic abnormalities and amyloid pathology in Alzheimer's disease. *Neuron* **84**, 63–77 (2014).
34. Martin, M., Rehani, K., Jope, R. S. & Michalek, S. M. Toll-like receptor-mediated cytokine production is differentially regulated by glycogen synthase kinase 3. *Nat. Immunol.* **6**, 777–784 (2005).
35. Azim, K. & Butt, A. M. GSK3 β negatively regulates oligodendrocyte differentiation and myelination in vivo. *Glia* **59**, 540–553 (2011).
36. Nunes, M. A. et al. Chronic microdose lithium treatment prevented memory loss and neurohistopathological changes in a transgenic mouse model of Alzheimer's disease. *PLoS ONE* **10**, e0142267 (2015).
37. Zhao, L. et al. Beneficial synergistic effects of microdose lithium with pyrroloquinoline quinone in an Alzheimer's disease mouse model. *Neurobiol Aging* **35**, 2736–2745 (2014).
38. Trujillo-Estrada, L. et al. In vivo modification of Abeta plaque toxicity as a novel neuroprotective lithium-mediated therapy for Alzheimer's disease pathology. *Acta Neuropathol. Commun.* **1**, 73 (2013).
39. Zhang, X. et al. Long-term treatment with lithium alleviates memory deficits and reduces amyloid- β production in an aged Alzheimer's disease transgenic mouse model. *J. Alzheimers Dis.* **24**, 739–749 (2011).
40. Fiorentini, A., Rosi, M. C., Grossi, C., Luccarini, I. & Casamenti, F. Lithium improves hippocampal neurogenesis, neuropathology and cognitive functions in APP mutant mice. *PLoS ONE* **5**, e14382 (2010).
41. Phiel, C. J., Wilson, C. A., Lee, V. M.-Y. & Klein, P. S. GSK-3 α regulates production of Alzheimer's disease amyloid- β peptides. *Nature* **423**, 435–439 (2003).
42. Su, Y. et al. Lithium, a common drug for bipolar disorder treatment, regulates amyloid- β precursor protein processing. *Biochemistry* **43**, 6899–6908 (2004).
43. Rockenstein, E. et al. Neuroprotective effects of regulators of the glycogen synthase kinase-3 β signaling pathway in a transgenic model of Alzheimer's disease are associated with reduced amyloid precursor protein phosphorylation. *J. Neurosci.* **27**, 1981–1991 (2007).
44. Wilson, E. N. et al. NP03, a microdose lithium formulation, blunts early amyloid post-plaque neuropathology in McGill-R-Thy1-APP Alzheimer-like transgenic rats. *J. Alzheimers Dis.* **73**, 723–739 (2020).
45. Sofola-Adesakin, O. et al. Lithium suppresses A β pathology by inhibiting translation in an adult *Drosophila* model of Alzheimer's disease. *Front. Aging Neurosci.* **6**, 190 (2014).
46. Leroy, K. et al. Lithium treatment arrests the development of neurofibrillary tangles in mutant tau transgenic mice with advanced neurofibrillary pathology. *J. Alzheimers Dis.* **19**, 705–719 (2010).
47. Caccamo, A., Oddo, S., Tran, L. X. & LaFerla, F. M. Lithium reduces tau phosphorylation but not A β or working memory deficits in a transgenic model with both plaques and tangles. *Am. J. Pathol.* **170**, 1669–1675 (2007).
48. Nakashima, H. et al. Chronic lithium treatment decreases tau lesions by promoting ubiquitination in a mouse model of tauopathies. *Acta Neuropathol.* **110**, 547–556 (2005).
49. Noble, W. et al. Inhibition of glycogen synthase kinase-3 by lithium correlates with reduced tauopathy and degeneration in vivo. *Proc. Natl Acad. Sci. USA* **102**, 6990–6995 (2005).
50. Hampel, H. et al. Lithium trial in Alzheimer's disease: a randomized, single-blind, placebo-controlled, multicenter 10-week study. *J. Clin. Psychiatry* **70**, 922–931 (2009).
51. Macdonald, A. et al. A feasibility and tolerability study of lithium in Alzheimer's disease. *Int. J. Geriatr. Psychiatry* **23**, 704–711 (2008).
52. Forlenza, O. V. et al. Disease-modifying properties of long-term lithium treatment for amnestic mild cognitive impairment: randomised controlled trial. *Br. J. Psychiatry* **198**, 351–356 (2011).
53. Nunes, M. A., Viel, T. A. & Buck, H. S. Microdose lithium treatment stabilized cognitive impairment in patients with Alzheimer's disease. *Curr. Alzheimer Res.* **10**, 104–107 (2013).
54. Forlenza, O. V., Radanovic, M., Talib, L. L. & Gattaz, W. F. Clinical and biological effects of long-term lithium treatment in older adults with amnestic mild cognitive impairment: randomised clinical trial. *Br. J. Psychiatry* **215**, 668–674 (2019).
55. Damiano, R. F. et al. Revisiting global cognitive and functional state 13 years after a clinical trial of lithium for mild cognitive impairment. *Braz. J. Psychiatry* **45**, 46–49 (2023).
56. Kakhi, S. & Ahmadi-Soleimani, S. M. Experimental data on lithium salts: From neuroprotection to multi-organ complications. *Life Sci.* **306**, 120811 (2022).
57. Haney, M. S. et al. APOE4/4 is linked to damaging lipid droplets in Alzheimer's disease microglia. *Nature* **628**, 154–161 (2024).

Publisher's note Springer Nature remains neutral with regard to jurisdictional claims in published maps and institutional affiliations.



Open Access This article is licensed under a Creative Commons Attribution-NonCommercial-NoDerivatives 4.0 International License, which permits any non-commercial use, sharing, distribution and reproduction in any medium or format, as long as you give appropriate credit to the original author(s) and the source, provide a link to the Creative Commons licence, and indicate if you modified the licensed material. You do not have permission under this licence to share adapted material derived from this article or parts of it. The images or other third party material in this article are included in the article's Creative Commons licence, unless indicated otherwise in a credit line to the material. If material is not included in the article's Creative Commons licence and your intended use is not permitted by statutory regulation or exceeds the permitted use, you will need to obtain permission directly from the copyright holder. To view a copy of this licence, visit <http://creativecommons.org/licenses/by-nc-nd/4.0/>.

© The Author(s) 2025

Methods

Human brain samples

Post-mortem human brain and serum samples were obtained in accordance with institutional guidelines and with approval from the Harvard Medical School Institutional Review Board. All procedures complied with relevant ethical regulations. All post-mortem human brain and serum samples were fully deidentified before receipt, and no identifiable private donor information was accessible to the researchers. As such, informed consent was not applicable. Frozen post-mortem samples from the prefrontal cortex (BA9/10/47) were available for all cases included in the analysis. Cerebellar tissue and the most recently collected pre-mortem serum samples were available for a subset of individuals. The primary analysis was performed on tissue samples procured from the Rush Alzheimer's Disease Center, derived from participants in the Religious Orders Study (ROS) or Rush Memory and Aging Project (MAP) (referred to as ROSMAP). The ROSMAP is a longitudinal, clinical-pathological study of ageing, cognitive decline and AD⁵⁸. Study participants agreed to comprehensive annual clinical and neuropsychological evaluation and brain donation at death. To assess cognitive function, 21 cognitive-function tests were used, 19 were in common and 11 were used to inform on clinical diagnoses, as previously described^{59,60}. The follow-up rate exceeded 95% and the autopsy rate exceeded 90%. All individuals who underwent autopsy were subject to a uniform structured neuropathological evaluation of AD. Informed consent, an Anatomic Gift Act and a repository consent were obtained and the studies were approved by an Institutional Review Board of Rush University Medical Center. A second set of frozen frontal cortical brain samples was obtained from brain banks at the Massachusetts General Hospital, Duke University and Washington University, and is referred to as "a second independent cohort". Brain tissue obtained from these sources had a confirmed pathological diagnosis of AD or NCI. Samples were randomly selected by the source institutions based on tissue availability and alignment with the requested diagnostic categories (NCI, MCI and AD). Within each diagnostic group, samples were matched for age and sex to ensure group comparability.

Absolute and relative metal levels were measured by ICP-MS, with relative levels calculated as the ratio of cortical or cerebellar to serum concentrations from the same individual. Post-mortem interval had no significant effect on total or relative Li levels in this cohort. The study population comprised 40.2% male individuals and 59.8% female individuals. Within diagnostic subgroups, NCI cases comprised 40.8% male individuals and 59.2% female individuals; MCI cases, 42% male individuals and 58% female individuals; and AD cases, 36.4% male individuals and 63.6% female individuals. Individuals of both sexes were analysed, and those with MCI and AD, regardless of sex, exhibited significantly reduced cortical-to-serum Li ratios and lower total cortical Li levels. Donor sex was self-reported and provided by Rush Medical Center (ROSMAP study) and by further tissue sources, including Massachusetts General Hospital, Duke University and Washington University.

Isolation of plaque-enriched and non-plaque fractions

To fractionate brain parenchymal homogenates into amyloid plaque-enriched and non-plaque fractions, we modified a previously described protocol^{61,62}. Frozen brain samples were weighed and then Dounce-homogenized (40 strokes per sample) in 5 volumes (v/w) of ultrapure buffer containing 2% SDS (stock of ultrapure SDS 10%, ThermoFisher Scientific, 24730020) and 0.1 M β-mercaptoethanol (VWR, 97064-878) in 50 mM Tris HCl, pH 7.6 (ultrapure Tris-HCl, pH 7.5, Invitrogen, 15567-027) and water (Aristar Ultra, VWR 87003-236). The Li concentration of the complete buffer was below the detection threshold (<0.02 µg l⁻¹). The homogenates were heated at 100 °C for 10 min and then transferred to a 15-ml Falcon tube fitted with a sieve consisting of woven mesh (polyethylene terephthalate) with a pore size of 100 µm (pluriSelect, SKU 43-10100-60). The samples were passed through

the sieve by gravity and the filtrate was then centrifuged (300 g for 30 min). The supernatant (soluble non-plaque fraction) was removed and stored at -80 °C. The pellet was resuspended in water at a ratio of 5 ml per gram of pellet mass and stored at -80 °C (plaque-enriched fraction). To image subfractionated Aβ and phospho-tau (Supplementary Fig. 1), 10 µl of the freshly collected plaque-enriched and non-plaque fractions was layered onto albumin-coated glass slides and allowed to dry overnight. They were then washed with ultrapure PBS (which we determined contained less than 25 parts per trillion (ppt) Li) and incubated with a rabbit monoclonal anti-Aβ antibody (Cell Signaling, 8243) and a mouse monoclonal antibody to pSer202-tau (clone CP13) overnight in 2% BSA, 0.1% Triton X-100 in PBS, followed by labelling with secondary anti-rabbit IgG coupled to Alexa Fluor 594, or anti-mouse IgG coupled to Alexa Fluor 488 (1:300 in blocking buffer). The slides were then washed three times in ultrapure PBS and mounted.

ICP-MS

For the analysis of metals in human and mouse biological samples, we modified previous protocols to optimize the detection of ultra-trace elements. We tested several protocols and found that the use of pre-cleaned polyvinylidene difluoride (PVDF) vials fitted with perfluoroalkoxy alkane (PFA) caps, the use of ultra-trace grade reagents (nitric acid, hydrogen peroxide and water), combined with an extended sample digestion and homogenization, and a highly sensitive ICP-MS instrument (PerkinElmer NexION 2000C), allowed the robust detection of ultra-trace metals in human and mouse samples. The commercial precleaned PVDF vials (Elemental Scientific, V-14-0712-C) and PFA caps (Elemental Scientific, V-14-0309-C) were further processed by fully immersing them in 10% trace-grade nitric acid (Fisher Chemical, A509-P212) for at least 48 h, followed by abundant rinsing with double-distilled and deionized water and drying in a chemical hood for 48 h. The chemical hood was thoroughly cleaned before the experiment and was used exclusively for ICP-MS for the entire duration of the experiment to prevent contamination. We also used a protocol allowing for the simultaneous analysis of a large number of human brain samples (approximately 80–120 mg frozen brain material per region per case). First, we determined that the dry-to-wet ratio was unchanged in AD versus NCI. This was established in *n* = 45 NCI and *n* = 45 AD frozen cortical samples (100–200 mg per sample) that were weighed and then dried to a constant weight (48 h in a dry oven at 60 °C). The dry-to-wet ratios were 0.127 ± 0.048 for NCI and 0.123 ± 0.034 for AD and were not statistically different (*P* = 0.67), in agreement with previous work⁶³.

The frozen cortical and cerebellum samples were first allowed to thaw, and were then weighed and digested in 5 volumes of nitric acid 67% (w/m, relative to wet mass; BDH Aristar Ultra, VWR, 87003-226) for 72 h with regular vortexing (20 s per vial every 12 h). The samples were fully digested after about 36 h. The serum, the brain non-plaque fractions and the aqueous solutions were digested in an equal volume of nitric acid (67%) for 48 h with regular vortexing (20 s per vial every 12 h). After digestion with nitric acid, hydrogen peroxide (30%; BDH Aristar Ultra, VWR, 87003-224) was added for 24 h with regular vortexing (20 s per vial every 12 h). We added one volume of hydrogen peroxide (w/m, relative to starting wet mass) to digested brain tissues and 0.75 volumes (relative to starting sample volume) to digested serum, non-plaque fractions and aqueous solutions. The samples were then diluted using a 2% nitric solution in ultrapure water (BDH Aristar, VWR, 87003-236). Indium was added to each solution as an internal standard (50 parts per billion; ppb). For all ICP-MS runs, we also measured freshly made solutions of element standards (0, 10 ppt, 50 ppt, 100 ppt, 1 ppb, 10 ppb and 50 ppb) using a 30-element ICP standard (Aristar, VWR, 89800-580). Each run included *n* = 10 digestion blanks as well as *n* = 20–30 blank measurements to calculate the detection limits. The samples were injected into a PerkinElmer NexION 2000C ICP-MS instrument fitted with a cross-flow nebulizer and peristaltic pump for sample introduction. The sample delay time was 30 s with a pump speed of 24 rpm.

Article

A wash solution of 2% nitric was used between analyses of samples. The human cortex, cerebellum and serum samples were each measured twice on two consecutive days (two technical replicates per sample) and the average value was obtained for each sample. The correlation coefficients between the lithium concentrations measured on day 1 and day 2 were $r > 0.99$ for frontal cortex, cerebellum and serum, showing that the ICP–MS measurement was highly reproducible. After each run, ICP–MS signal processing was done using GeoPro 2010 Software (Cetac Technologies). We derived the standard curves for each element, calculated the concentration of each element in the diluted solution, and used the dilution factors to derive elemental abundance in the original samples. Li levels in the cortex and cerebellum are reported per unit of wet weight (Fig. 1d,e, Extended Data Fig. 1b and Supplementary Table 1). Limits of detection (LODs) and limits of quantification (LOQs) were calculated as follows: $\text{LOD} = Y_B + 2tS_B$ and $\text{LOQ} = Y_B + 10S_B$, where Y_B is the average blank signal, t is the critical value of the one-tailed t -test (one-tailed, 95% confidence interval; for example, for 27 blank samples, $df = 26$ and $t = 1.706$) and S_B is the standard deviation of a blank signal. LOD and LOQ values for all metals can be found in Supplementary Table 1. All individual Li measurements in human samples (prefrontal cortex, cerebellum and serum) were above the LOQ. In recovery experiments, wet brain samples or fluids were spiked with lithium standard added at three levels ($n = 7$ replicates per spiking level). The recovery of Li from spiked samples ranged from 91% to 105%. All human sample measurements were double-blinded: one lab member not involved in the study relabelled the samples and kept a file with the old and new codes. After the ICP–MS measurements, the samples were unblinded in the presence of the researchers involved in the study, as well as the lab member who was not involved in the study.

The ICP–MS findings from post-mortem human samples were replicated as follows. First, reduced Li content in the cortex of patients with AD was observed using two independent methods, after measurement of total Li levels in frozen cortical material of cases from both ROSMAP (Fig. 1d) and other sources (Fig. 1e), as well as after fractionation and removal of amyloid plaques (Fig. 1g). Second, decreased Li levels in the AD versus NCI prefrontal cortex ($P = 2 \times 10^{-3}$) were also independently confirmed when $n = 60$ NCI and AD cases were processed and analysed by ICP–MS in a different laboratory (the Spectroscopy Core Facility at the University of Nebraska, Lincoln). Third, decreased Li levels in the AD versus NCI prefrontal cortex ($P = 3 \times 10^{-3}$) were also confirmed when $n = 48$ NCI and AD cases were processed using an alternative protocol. Frozen samples were thawed and dried to a constant weight by incubating in a dry oven at 60 °C for 48 h. The dried tissue was then digested in 1 ml of 67% nitric acid using a heating block at 95 °C for 3 h. After digestion, 0.3 ml of 30% hydrogen peroxide was added and the mixture was heated for a further 3 h. Finally, the samples were diluted and analysed using ICP–MS.

Li levels measured in the PFC of ageing NCI cases (ROSMAP cases: mean 2.36 ± 1.23 ng per g, range 0.52–6.0 ng per g; non-ROSMAP cases: mean 3.50 ± 2.27 ng per g, range 0.89–9.94 ng per g; Fig. 1d,e) were similar to those measured in a previous study⁶⁴ (4.1 ± 1.7 ng per g in the prefrontal cortex of aged non-diseased cases; age, 71 ± 12 years). Similarly, Li levels measured in the cerebellum (ROSMAP cases: mean 2.90 ± 1.69 ng per g, range 0.58–8.40 ng per g; Extended Data Fig. 1b) were similar to those measured in the previous study⁶⁴ (2.9 ± 1.3 ng per g). Finally, consistent with previous studies, we observed significantly elevated levels of sodium²⁵ and zinc²⁶, along with reduced copper^{12,65} levels, in the AD cortex (Fig. 1a,b and Supplementary Table 1).

LA-ICP–MS

The Li composition in the human and mouse brains *in situ* was analysed using LA-ICP–MS. Frozen human and mouse brains were first embedded in OCT medium and then sectioned using a cryostat, and the resulting sections (80 µm thick) were mounted onto glass slides. Before data acquisition, the samples were placed vertically in a rack and air-dried

for 1 h. The LA-ICP–MS spectrometer consisted of a laser ablation system (213 nm Nd:YAG, Cetac Technologies) connected to a Perkin Elmer NexION 2000C ICP–MS (Perkin Elmer). Using the line tool, we manually selected the area to be ablated. For human samples, we ablated a region of the prefrontal cortex. For mouse samples, we processed coronal sections where the cortex and hippocampus were readily identifiable. The analyte signal was collected using multiple parallel line scans along the entire selected area, progressing in the direction of ablation cell gas flow, using a spot size of 200 µm at 75 µm s⁻¹. The laser operated at an energy level of 70% and a pulse repetition rate of 20 Hz. The typical run time for one sample was about 4–5 h. We also ablated parts of each section that did include brain tissue but contained embedding medium (OCT) and subtracted this background signal from the total signal. Levels of ⁷Li were normalized to carbon (¹²C) to correct for any variations in the amount of tissue ablated. Similar conclusions were reached when the analysis did not include normalization to ¹²C. Matrix-matched standards were obtained by spiking homogenized samples of human or mouse tissue with three different concentrations of metal standard solution containing the analytes of interest. After homogenization, the mixtures were frozen and 80-µm sections were cut using the cryostat. The final concentrations of these standards were validated by ICP–MS. After LA-ICP–MS data acquisition, signal processing was done using Iolite Software 2018 (Iolite). A Li distribution matrix was generated computationally, using the multiple parallel line rasters. To identify the regions occupied by amyloid plaques, the section immediately adjacent to the section analysed by LA-ICP–MS was processed for Aβ immunofluorescence. In brief, the adjacent section was first fixed with 4% PFA for 2 h then washed three times with PBS. The section was then blocked for 1 h with 2% BSA, 2% fetal bovine serum, 0.1% Triton X-100 in PBS. The anti-Aβ primary antibody (Cell Signaling, 8243), diluted 1:250 in blocking buffer, was then added and the section was incubated overnight at 4 °C. The next day, the section was washed three times with PBS (in total, 30 min), and a secondary anti-rabbit Alexa 594 antibody (diluted 1:300 in blocking buffer) was added for 3 h. The section was finally washed three times with PBS (for 30 min) and mounted. We acquired multiple pictures of Aβ immunofluorescence spanning the entire section using an Olympus FV3000 confocal microscope. The images were then stitched together and imported into Iolite, where the distribution of Aβ immunofluorescence was computationally superimposed on the LA-ICP–MS Li distribution matrix. For each human or mouse sample, we manually selected multiple regions containing Aβ plaques ('plaque' or 'P regions') as well as neighbouring regions devoid of plaques ('non-plaque' or 'NP regions').

The mean Li levels in P and NP regions were determined, and after correcting for background and normalizing to ¹²C, the P:NP ratios were calculated. Three other isotopes were also assessed: ⁵⁷Fe, ⁶³Cu and ⁶⁶Zn. All measurements in P and NP regions exceeded the LOQ, which was 0.82 ng per g for ⁷Li, 0.23 µg per g for ⁵⁷Fe, 0.44 µg per g for ⁶³Cu and 55.1 ng per g for ⁶⁶Zn. As positive controls, ⁵⁷Fe, ⁶³Cu and ⁶⁶Zn were all enriched in plaques relative to non-plaque regions in the AD brain, consistent with previous observations⁶⁶.

Lithium salts

LiO was obtained from Innophos Nutrition and LiC was from Rockwood Lithium. The purity and Li content were verified by mass spectrometry and ICP–MS, respectively. Sources for other Li salts used in conductivity assays are provided in Supplementary Table 16.

Li salts were dissolved in distilled, deionized drinking water and administered ad libitum to mice. The low Li dose corresponded to 4.3 µEq l⁻¹ (equivalent to 0.03 mg (30 µg) of elemental Li per litre). The background Li concentration in the water was minimal (0.109 µg l⁻¹). Solutions of 4.3 µM LiO and 2.15 µM LiC were prepared to deliver equivalent amounts of elemental Li, accounting for the two Li atoms per molecule of LiC (Li₂CO₃). A 4.3 µM sodium orotate (NaO) solution was also prepared to assess the effects of the orotate anion in the absence

of Li. Two more Li doses were also tested: 43 $\mu\text{Eq l}^{-1}$ (delivered as 43 μM LiO) and 430 $\mu\text{Eq l}^{-1}$ (delivered as 430 μM LiO or 215 μM Li₂CO₃). To control for the orotate anion at the high dose, a 430 μM NaO solution was also tested. Average daily water consumption was comparable across all treatment groups and the vehicle (water-only) group. To evaluate Li uptake and its biological effects in the brain, mice received the Li-containing water for defined periods. Animals were randomly assigned to treatment and control groups, with control mice receiving plain drinking water.

Conductivity measurements

To measure the conductivity of Li salts, the salts were dissolved in water to achieve Li concentrations of 4.3 mEq l⁻¹, 430 $\mu\text{Eq l}^{-1}$, 43 $\mu\text{Eq l}^{-1}$ or 21.5 $\mu\text{Eq l}^{-1}$ in each case. Conductivity was measured using an ST300C conductivity meter (OHAUS, 83033964) equipped with a STCON7 electrode (OHAUS, 30080693) calibrated with potassium chloride conductivity standards. For each lithium salt, three independent solution replicates ($n = 3$) were prepared. Conductivity values are reported in $\mu\text{S per cm}$ at 25 °C.

In vitro binding of lithium to A β

To assess the in vitro binding of Li to A β , both oligomeric and fibrillar forms of A β 42 were prepared. Human A β 1–42 peptide (1 mg) was initially dissolved in 80 μl of 1% NH₄OH then diluted with PBS to a final concentration of 1 mg ml⁻¹ (stock solution) and stored at -80 °C. Oligomeric A β 42 was generated by resuspending the stock solution in PBS followed by overnight incubation at 4 °C. Fibrillar A β 42 was obtained by incubating the same stock at 37 °C for 72 h. For Li binding assays, 10 μg of either oligomeric or fibrillar A β 42 (10 μl of the 1 mg ml⁻¹ stock) was added to 90 μl of Li-containing solutions. These solutions included varying concentrations of either LiO or LiC, matched for Li content and dissolved in ultrapure water (BDH Aristar, VWR, 87003-236). Ultrapure water alone served as the negative control. Samples were incubated at 37 °C for 16 h. After incubation, the mixtures were transferred to dialysis membranes for 24 h to remove unbound Li (Pur-A-Lyzer mini dialysis kits were used: 6–8 kDa cut-off for oligomers and 25 kDa for fibrils). After dialysis, the samples were transferred into precleaned PVDF vials and digested by adding an equal volume of 67% nitric acid (final volume, 200 μl), followed by a 24-h digestion period. The digested samples were then diluted to 800 μl with 2% nitric acid prepared in ultrapure water. Li content was quantified using a PerkinElmer NEXION 2000C ICP-MS instrument. Elemental Li standards were prepared and standard curves showed excellent linearity ($r > 0.99$). The bound ⁷Li levels were calculated across a range of Li salt concentrations, and binding curves were plotted using GraphPad Prism (v.9.4.1). Binding affinities (EC₅₀) and 95% confidence intervals for LiO and LiC were determined using nonlinear regression analysis ([agonist] versus response-variable slope, four-parameter model; Supplementary Table 13). Binding to A β 42 oligomers and fibrils was modelled across the full concentration range (0–500 $\mu\text{Eq l}^{-1}$) as well as within the higher-affinity subranges (0–50 $\mu\text{Eq l}^{-1}$ for oligomers and 0–30 $\mu\text{Eq l}^{-1}$ for fibrils; Supplementary Table 13).

Mice

Animal housing and experimental procedures were approved by the Institutional Animal Care and Use Committee of Harvard Medical School. All mice were housed socially (2–4 animals per cage) in a room with a 12 h:12 h light:dark cycle (lights on at 06:00), controlled for temperature (18–22 °C) and humidity (40–60%). Sentinel mice housed in each rack were tested quarterly and confirmed to be free of pathogens. All cages were individually ventilated. The standard diet 5053, as well as the chemically defined control and Li-deficient diets, were irradiated. Reverse osmosis deionized water and deionized water containing LiO, LiC or NaO was provided ad libitum in bottles that were changed at least weekly.

Wild-type mice were on a C57BL/6J background. We analysed both adult (3–6 months old) and aged (up to 26 months old) wild-type mice, treated for varying durations. The 3xTg mice¹⁴ carried APP^{Sw}e and tau^{P301L} mutant transgenes, as well as a PS1 knock-in mutation, and were in a hybrid C57BL/6J and 129Sv/Ev background. The J20 mice¹³ transgenic mice expressed a mutant form of the human amyloid protein precursor bearing both the Swedish (K670N/M671L) and the Indiana (V717F) mutations (APPSwInd) in a C57BL/6J background. For breeding, 10–20 females (all litter-mates derived from the same cross) were typically mated with 8–12 males (all litter-mates derived from the same cross). Mice were identified by numbered ear tags and were randomly selected for behavioural and histological analyses.

To assess treatment effects on disease onset and progression, animals were treated either before pathology emerged (5–6 months old for 3xTg; 3 months old for J20) or after pathology was established (starting at 9 months old for 3xTg and 17 months old for J20). To investigate age-related effects in wild-type mice, chronic treatments were initiated in adulthood (10–12 months old) and continued for 10–14 months during ageing. Experiments included both sexes, and results were consistent between males and females. The number and sex of animals used in each experimental group can be found in the Source Data file. Investigators remained blinded to genotypes and treatment conditions throughout data collection and analysis. No prior sample-size calculations were done, but the number of animals used was consistent with similar studies in the field.

Mouse diet

Li levels in the cortex were comparable between human NCI cases (RUSH cohort: range 0.52–6.0 ng per g; non-RUSH cohort: range 0.89–9.94 ng per g) and mice (wild type and J20: range 1.61–4.59 ng per g). Similarly, serum Li levels in human NCI cases (range 1.53–10.41 ng ml⁻¹) overlapped with those in mice (wild type, J20, 3xTg: range 0.75–4.50 ng ml⁻¹), supporting the relevance of mouse models for studying the biological effects of lithium.

The regular mouse 5053 is a grain-based diet that does not allow Li levels to be manipulated experimentally. To obtain a Li-deficient diet, we used a standard, chemically defined mouse AIN-93M diet that is calorically and nutritionally equivalent to the 5053 diet and was formulated as a standard diet for laboratory rodents by the American Institute of Nutrition in 1993. We tested 5 samples of the regular mouse 5053 diet and 5 samples of the AIN-93M diet and found that the average Li content was 104.8 ng per g in the 5053 diet and 103 ng per g in the AIN-93M diet. The AIN-93M chemically defined diet was modified to exclude Li. The Li-deficient and control AIN-93M diets were formulated by Dyets. We measured Li levels in the Li-deficient diet and confirmed that Li was depleted by 92.0% relative to the chemically defined control diet. The abundances of the other 26 metals that we measured by ICP-MS were identical (data not shown). The solid diets were irradiated before administration to animals. The diets were stored in closed plastic bags that were placed inside cardboard boxes (devoid of light) at -20 °C for up to 4 months before administration to animals.

DNA extraction and genotyping by PCR

We collected about 0.5–1.0 cm of mouse tails in clean Eppendorf tubes; 500 μl of tail lysis buffer (10 mM Tris pH 8, 100 mM NaCl, 10 mM EDTA, 0.5% SDS) containing 0.4 mg ml⁻¹ Proteinase K was added to each tube, and the tubes were incubated overnight in a 56 °C water bath. The next day, 500 μl of isopropanol was added to precipitate the DNA, and the tubes were shaken vigorously for 20 s. Tubes were centrifuged for 10 min at 18,000g and the isopropanol was carefully removed, avoiding the DNA pellet. We then added 70% ethanol and shook the tubes to wash the DNA pellet. We next centrifuged the tubes for 10 min at 18,000g. We removed the ethanol and air-dried the DNA pellet for 2–16 h. The DNA was resuspended in 100 μl acetate-EDTA buffer and placed in a 56 °C water bath overnight. To amplify DNA regions by PCR,

Article

we mixed 3 µl of DNA sample with corresponding amounts of forward and reverse PCR primers, PCR master mix and nuclease-free water, and ran the reactions in a thermocycler. Sample loading dye was added to the PCR products and the samples were run on 1–3% agarose gels (prepared by dissolving agarose in TAE buffer, to which Gel Red was added to allow DNA visualization). We also loaded a 100-bp DNA ladder. Gels were visualized using a UV transilluminator.

Quantitative RT-PCR

Total RNA was extracted from cells and tissues using TRIzol reagent (Invitrogen) followed by DNase treatment to remove genomic DNA contamination. Primers were obtained from Harvard's Primer-Bank: for mouse *Gsk3b*, forward 5'-TGGCAGCAAGGTAAACCACAG-3' and reverse 5'-CGGTTCTTAAATCGCTTGCCTG-3'; for mouse *Gapdh*, forward 5'-CTTGTCAGCTCATTCCTGG-3' and reverse 5'-TCTTGCTCAGTGTCTTG-3'. Real-time PCR was performed for 40 cycles. The specificity and purity of PCR and RT-PCR products were confirmed by the presence of single-peak melting curves.

GSK3β inhibitor treatment

Li-deficient and control 3xTg mice 12 months old, maintained on their respective diets for three months, were treated with the GSK3β inhibitor CHIR-99021 or a vehicle control. A stock solution of CHIR-99021 was prepared in DMSO and diluted in 0.9% saline to a final concentration of 10 mg ml⁻¹, containing 2% DMSO. The solution was warmed to 70 °C to ensure dissolution of the compound. Mice received intraperitoneal injections of CHIR99021 at a dose of 50 mg per kg body weight, once daily for 14 consecutive days. Control animals received equivalent volumes of vehicle (2% DMSO in saline). All animals tolerated the treatment without visible abnormalities and were included in the analysis.

Blood chemistry

BUN and creatinine measurements were done by IDEXX Laboratories, using mouse serum samples. TSH levels in the mouse serum were assessed by ELISA (Elabscience, E-EL-M1153).

Behavioural testing

Open field. Mice were placed in an open field box (75 cm × 75 cm) and movements were tracked in real-time using TopScan Lite software (CleverSys) coupled to a camera. Each mouse was recorded for 10 min, and the average speed and distance travelled were automatically recorded. Mice had no prior exposure to the open-field arena (spontaneous test). All behavioural experiments were performed by researchers who were blinded to the experimental conditions.

Morris water maze. To assess spatial learning and memory, we trained and tested mice in a large circular pool (1.1 m in diameter) filled with 21 °C water, which was rendered opaque by the addition of non-toxic white paint. We placed four distinct visual cues (representing different geometric shapes, patterns and colours) on each wall, to facilitate spatial orientation and the acquisition of spatial memory. Mice were given four training trials a day for 5–7 consecutive days. Each training trial lasted for 1 min. Mice were trained to remember the location of a hidden platform that was submerged 2.5 cm below the water surface. The location of the hidden platform (south-east) remained the same during the 5–7-day training period. If, after a 60-second trial, the animal failed to locate the platform, it was placed on the platform and allowed to remain on the platform for 15 s. Mice were trained four times a day and entered the pool in a randomized order of rotating entrance points (compass directions N, S, E, W, NE and SW). During each training trial, the latency to find the hidden platform was recorded. Then, 24 h after the last training trial, a probe trial was conducted. The platform was removed and mice entered the arena from the NW location (opposite from the platform). The number of entries in the target area (representing the area where the platform had been located during the training

trials), the total time spent in the target area, as well as the time spent in all quadrants, and the swimming speed were recorded during the 60-s probe trial. We also conducted separate trials in which a visible platform (platform elevated above the water level, on which a small red flag had been placed) was presented. Mice were given several training sessions and the time (latency) to reach the visible platform was recorded. Mouse movements, as well as average speed, distance travelled, latency to reach a quadrant or target area and number of entries in the target area, were tracked in real time using TopScan Lite software (Clever Sys) and the different measures were automatically recorded. For measurements of learning (latency to reach the platform during the training trials), mice underwent repeated measurements (four measurements a day for 6–7 consecutive days).

Novel-object recognition. Mice were placed in the same open-field box with two novel identical objects for 10 min and allowed to freely explore the identical objects. The next day, mice were reintroduced in the open-field box and presented with a novel object, as well as one of the two objects they explored the previous day. The mice were allowed to explore the objects for 10 min and their movements were tracked in real time using TopScan Lite software (Clever Sys) coupled to a camera. The box and items were cleaned with 70% ethanol between mice. We automatically recorded the time each mouse spent exploring each object, on both day 1 (two identical objects) or day 2 (one novel object and one familiar object), and derived a novelty (discrimination) index, defined as the ratio of time spent exploring the novel object relative to the familiar one.

Y maze. Spontaneous alternation, which is a measure of spatial working memory, was assessed by allowing the mice to freely explore a Y-shaped maze for 8 min. The Y maze consisted of 3 arms (each 40 cm × 8 cm × 15 cm) at an angle of 120° from each other. Mice typically preferred to investigate a new arm of the maze, rather than returning to one that was previously visited. Using TopScanLite software, we recorded each entry in one of the three arms (A, B and C) and then derived the percentage of total correct alternations over the 8-min duration of the trial. A correct alternation (triad) is a succession of entries into three different arms (A–B–C, A–C–B, B–A–C, B–C–A, C–A–B or C–B–A).

Mouse neuropathology

Mice were anaesthetized with isoflurane and carbon dioxide and then perfused with PBS at 4 °C for 20 min. Brains were rapidly removed and the two hemispheres were separated. One hemisphere was dissected into subregions (frontal cortex, temporal cortex, occipital cortex, hippocampus and cerebellum). Each subregion was placed in a separate Eppendorf tube, snap-frozen in liquid nitrogen and then stored in a freezer at –80 °C. The second hemisphere was placed in 4% paraformaldehyde for 48 h. The fixed brain was then processed for paraffin embedding, using standard procedures. Paraffin-embedded blocks were sectioned and 6-µm sections were mounted on glass slides and used for histological analyses.

Paraffin-embedded mouse brain blocks were sectioned and the sections were mounted on glass slides. We deparaffinized the sections by immersion in two xylene baths for a total of 10 min, followed by a 5-min immersion in a 50% xylene:50% ethanol solution. The sections were then rehydrated by immersion in solutions of decreasing concentrations of ethanol (95%, 90%, 70% and 50%) and then placed in water. Sections then underwent antigen retrieval using the Diva decloaker (BioCare). Sections were blocked with 3% BSA, 3% fetal bovine serum (FBS) and 0.1% Triton X-100 in PBS for 45 min at room temperature. Primary antibodies (Supplementary Table 16 has a list of antibodies used for immunolabelling) were diluted in 3% BSA, 3% FBS and 0.1% Triton X-100 in PBS. After overnight incubation at 4 °C, sections were washed three times with PBS. Secondary antibodies, diluted in 3% BSA, 3% FBS and 0.1% Triton X-100 in PBS were either biotin-coupled (1:200; Vector Labs) or coupled to

Alexa fluorophores (1:300, Invitrogen). After three 10-min washes with PBS, sections were mounted with Pro-Long anti-fade mounting medium with DAPI (Invitrogen) and then imaged using confocal microscopy. For the A β labelling shown in Extended Data Fig. 1e, we incubated sections with an anti-rabbit biotinylated IgG secondary antibody (VectorLabs) for 1 h, followed by three washes in PBS (1 min each) and the addition of avidin-streptavidin-HRP-coupled complex (1:200 in 2% BSA and 0.1% Triton X-100 in PBS; VectorLabs). After three washes with PBS, we added diaminobenzidine (DAB) substrate (prepared by dissolving DAB and peroxide tablets in PBS; Sigma-Aldrich) and incubated for several minutes, until a brown precipitate formed. Sections were then washed with PBS, dehydrated with increasing ethanol concentrations (50%, 70%, 90%, 95% and 100%), followed by incubation with a 50% ethanol:50% xylene solution and two immersions in 100% xylene (5 min each). Sections were mounted with a hydrophobic mounting medium (Permount). For Thioflavin S staining, after deparaffinization the brains were incubated with filtered 1% aqueous Thioflavin-S for 8 min at room temperature, then washed twice (3 min each) in 80% ethanol, once in 95% ethanol (3 min), three times in distilled water and finally mounted. For sections labelled by immunofluorescence, multiple confocal images were acquired using an Olympus Fluoview Confocal Microscope FV3000. For DAB-stained sections, we acquired pictures using a bright-field microscope coupled with a camera.

For analysis of the A β plaque burden, pictures of A β immunoreactivity (using the rabbit anti-A β monoclonal antibody, clone D54D2, Cell Signaling, 8243, dilution 1:250) in the hippocampus were processed using a macro developed for use with Fiji/ImageJ 2.9.0. In brief, confocal pictures were all saved in the same folder and were all automatically opened in Fiji and processed serially. For each picture, the background was subtracted (rolling ball radius was set for 25). Pictures then underwent de-noising, using a Gaussian blur filter (radius of one pixel). The images were then thresholded using the Default Fiji threshold set at 120. Particles with a minimal size of 5 μm^2 were retained and their number, average size and mean fluorescence intensity were automatically recorded for each picture in an Excel file. To calculate the A β plaque burden, the total area occupied by A β plaques was divided by the area of the selection. Three coronal sections (6 μm thick) were sampled for each animal, in the rostral, intermediate and ventral hippocampus. Two 20 \times images were acquired per section, using an Olympus FluoView LV1000 confocal microscope. The average A β burden was obtained by averaging the A β plaque density (area occupied by A β plaques divided by the total area analysed) in all pictures acquired for each animal.

For analysis of tau pathology, pictures of p-Ser202 tau (CP13, dilution 1:150) or p-Ser396/Ser404 tau (PHF1, dilution 1:200) immunoreactivity in the hippocampus CA1 were processed using a macro developed for use with Fiji/ImageJ 2.9.0. In brief, confocal pictures were all saved in the same folder and were all automatically opened in Fiji and processed serially. Pictures underwent de-noising, using a Gaussian blur filter (radius of one pixel). The images were then thresholded using the Default Fiji threshold set at 150. The number of tau-positive neurons in the selected CA1 area was then manually counted for each thresholded picture and the area was measured. For each picture, we calculated the average density of tau-positive neurons (the total number of tau-positive neurons divided by the area of the region). The average tau-positive neuron densities were calculated for each animal by averaging all the pictures acquired.

Fluorescent image analysis was also performed using MetaMorph NX 2.5 (Meta Series, Molecular Devices). Mean fluorescence intensity for specific markers was quantified in each animal either in the nucleus (β -catenin) or across the entire cell body (for example, GSK3 β , pSer9-GSK3 β , pTyr216-GSK3 β , GPNMB and LPL), based on co-labelling with cell-type-specific markers (such as MAP2, aspartoacylase and Iba1). Between 50 and 300 cells per mouse were analysed, and background signal was subtracted. Synaptophysin and PSD-95 fluorescence intensities were quantified in the CA1 region of the hippocampus, and

FluoroMyelin, MBP and SMI-312 intensities were measured in the corpus callosum, with background subtraction applied in all cases. Cell densities of Iba1 $^+$, CD68 $^+$, aspartoacylase $^+$, PDGFR α $^+$ and GFAP $^+$ populations were also determined in relevant brain regions by quantifying 50–500 cells per mouse. For each measurement, multiple images were acquired at 4 \times , 10 \times , 20 \times or 40 \times magnification per animal, spanning the region of interest. Values were averaged for each animal before statistical analysis. The following primary antibodies were also used: anti-aspartoacylase [NIC3-2] (GeneTex, GTX113389; rabbit polyclonal, dilution 1:200), anti-aspartoacylase (clone D-11; Santa Cruz Biotechnology, sc-377308, mouse monoclonal, dilution 1:50), anti- β -catenin (clone E247; Abcam, ab32572; rabbit recombinant monoclonal, dilution 1:250), anti- β -catenin (clone 1B8A1; PTGlab, 66379-1-Ig, mouse monoclonal, dilution 1:200), anti-CD68 (clone KP1; Abcam, ab955; mouse monoclonal, dilution 1:200), anti-GFAP (Sigma-Aldrich, G9269; rabbit polyclonal, dilution 1:200), anti-GSK3 β (clone 3D10; Novus Bio, NBP1-47470SS; mouse monoclonal, dilution 1:200), anti-pTyr216-GSK3 β (Millipore Sigma, SAB4300237; rabbit polyclonal, dilution 1:100), anti-pSer9-GSK3 β (Abcam, ab131097; rabbit polyclonal, dilution 1:100), anti-Iba1 (clone EPR16588; Abcam ab178846; rabbit recombinant monoclonal, dilution 1:2,000), anti-PSD-95 (clone K28/43; Biologen, 810401; mouse monoclonal, dilution 1:250), anti-synaptophysin (clone SY38; Millipore Sigma, mouse monoclonal, MAB5258-I; dilution 1:200), anti-neurofilament marker (pan axonal marker; clone SMI-312; Biologen, 837904; mouse monoclonal, dilution 1:200), anti-GPNMB (clone 2B10B8; PTGlab, 66926-1-Ig; mouse monoclonal, dilution 1:200), anti-LPL (Novus Bio, AF7197-SP; goat polyclonal, dilution 1:200), anti-MAP2 (Phosphosolutions, 1099-MAP2; goat polyclonal, dilution 1:500), anti-MBP (clone D8X4Q; Cell Signaling, 78896; rabbit monoclonal, dilution 1:200) and anti-PDGFR α (R&D Systems, AF1062; goat polyclonal, dilution 1:200). Secondary antibodies were used at a 1:300 dilution: donkey anti-goat Alexa 594 (Invitrogen, A-11058), donkey anti-rabbit IgG (H+L) Highly Cross-Adsorbed antibody, Alexa 488 (ThermoFisher Scientific, A21206), donkey anti-mouse IgG (H+L) Highly Cross-Adsorbed antibody, Alexa 594 (ThermoFisher Scientific, A21203), donkey anti-mouse Alexa 647 (Invitrogen, A-31571), donkey anti-rabbit Alexa 647 (Invitrogen, A-31573) and donkey anti-goat Alexa 488 (Invitrogen, A-11055).

Golgi labelling. The brains were processed and stained using the FD Rapid Golgistain Kit (FD Neurotechnologies, PK401) following the manufacturer's protocol with minor modifications. Immediately after dissection, the brains were fixed overnight in 4% PFA. After cryosectioning, free-floating sections of 100 μm were shortly (10 min) fixed in 4% PFA, then stained using the kit's reagents and mounted using a glycerin-containing medium. Then 12 dendrites per mouse were imaged in the hippocampus or the cortex using a confocal microscope. Dendritic spine density was quantified using Fiji software v.2.9.0.

Transmission electron microscopy. The 3xTg mice were fed either a Li-deficient diet ($n = 8$) or a control diet ($n = 8$) from 6 to 12 months of age. At the end point, mice were perfused with a fixative containing 2.5% glutaraldehyde and 2.5% paraformaldehyde in 0.1 M sodium cacodylate buffer, pH 7.4 (Electron Microscopy Sciences, 15949). After perfusion, 1–2-mm 3 brain sections were generated and post-fixed overnight at 4 °C in fresh fixative. The corpus callosum was subsequently dissected and processed for embedding in TAAB Epon resin at the Harvard Electron Microscopy Core Facility. In brief, tissue was washed in 0.1 M cacodylate buffer, post-fixed in 1% osmium tetroxide and 1.5% potassium ferrocyanide for 1 h, rinsed in distilled water and incubated in 1% aqueous uranyl acetate for 1 h. After two further water rinses, samples were dehydrated through graded ethanol (50%, 70%, 90% and twice in 100%, for 10 min each) followed by 1 h in propylene oxide. Samples were then infiltrated overnight in a 1:1 mixture of propylene oxide and TAAB Epon (Marivac), embedded in pure TAAB Epon the next day and polymerized at 60 °C

Article

for 48 h. Ultrathin sections (approximately 80 nm thick) were cut on a Reichert Ultracut-S microtome, mounted on copper grids, stained with lead citrate and imaged using either a JEOL 1200EX or a Tecnai G² Spirit BioTWIN transmission electron microscope. Images were captured using an AMT 2k CCD camera and saved in TIFF format. Quantification of myelin sheath thickness, axon diameter and g-ratio was performed using MetaMorph NX 2.5 software (Meta Series, Molecular Devices). A total of 1,376 axons (control group) and 1,396 axons (Li-deficient group) were analysed from eight randomly selected fields per animal ($\times 4,800$ magnification) spanning the corpus callosum.

A β detection by ELISA

Mouse endogenous A β x-40 and A β x-42 levels were measured using a previously established protocol⁶⁷. In brief, hippocampi or cortices were homogenized in 20 volumes (v/w) of tissue lysis buffer consisting of 20 mM Tris-HCl (pH 7.4), 1 mM EDTA, 1 mM EGTA and 250 mM sucrose, supplemented with protease inhibitors (Roche) and 100 μ M AEBSF. Soluble A β species were extracted from tissue homogenates by diethanolamine treatment. Mouse A β (x-40) and A β x-42 were quantified using Wako ELISA kits (292-64501 and 294-62501, respectively). The LOQs were 7.44 pmol l⁻¹ for A β (x-40) and 4.75 pmol l⁻¹ for A β x-42. Sample concentrations ranged from 26.21 to 52.98 pmol l⁻¹ for A β (x-40) and from 11.72 to 22.40 pmol l⁻¹ for A β x-42, all above the respective LOQs.

Assessment of microglial function in vitro

Microglial purification for cell-culture assays. Wild-type Li-deficient and control mice were transcardially perfused with 1 \times cold PBS. The cortex and hippocampus were dissected and minced using a scalpel before transferring them to 5 ml digestion buffer (2 U ml⁻¹ of Dispase II, 20 U ml⁻¹ DNase I, 10 μ M HEPES in HBSS without calcium or magnesium). Samples were incubated for 30 min at 37 °C on an orbital shaker. The tissue was then homogenized by successive trituration with a Pasteur pipette followed by a 1 ml pipette. An equal volume of 1 \times HBSS was added to the homogenate and the resulting mix was passed through a 70- μ m cell strainer, then centrifuged at 300g for 10 min at 4 °C. Samples were resuspended with 40% Percoll (GE Healthcare, 17-0891-02) to remove myelin, and microglia were enriched using CD11b beads, as described above. Microglia were resuspended in pre-warmed media (DMEM/F12 with 2% FBS, 100 ng ml⁻¹ IL-34, 50 ng ml⁻¹ TGF β 1, 25 ng ml⁻¹ M-CSF) and counted using a haemocytometer. Microglia were seeded into 96-well glass-bottom plates precoated with poly-L-ornithine (Sigma, P4957) at 5,000 cells per well using 100 μ l of medium. A half-medium change was performed on day 2 and the downstream assay was done on day 3.

Primary microglia were also purified using an alternative protocol. After perfusion, the cortex and hippocampus were dissected, placed in 3 ml buffer (0.9% Hepes, 50 mM NaCl, pH 7.4) and minced with small scissors for 4 min. Then, 7 ml Dispase buffer (2 U ml⁻¹ Dispase II in 0.9% Hepes, 50 mM NaCl, pH 7.4) was added and the tissue was incubated for 1 h at 37 °C on an orbital shaker. The tissue was then homogenized by gently triturating with a 10 ml pipette with a wide bore, to prevent cell shearing. The enzyme activity was halted by the 1:1 addition of 10% fetal bovine serum in PBS (10 ml) at 4 °C. The homogenate was passed through a 70- μ m cell strainer to remove meninges and clumped cells. The homogenate was then spun for 10 min at 1,000g and 4 °C, and the supernatant was discarded. The pellet was resuspended in 6 ml of 75% isotonic percoll in PBS (high percoll; GE Healthcare, 17-0891-02). Then 5 ml of 35% isotonic percoll in PBS (low percoll) was added, followed by 4 ml of PBS. The resulting discontinuous gradient was allowed to settle for 15 min at 4 °C. We then centrifuged the tubes at 800g for 45 min at 4 °C. We then aspirated the top (PBS-containing) layer and part of the upper percoll layer. The band containing microglia (approximately 1.5 ml), situated at the interface between the 35% percoll and 75% percoll layers, was gently collected. Then 50 ml of PBS was gently added and the tube was inverted 20 times. The microglia were then centrifuged at 1,000g for 10 min. The supernatant was discarded and the pellet was

resuspended in a pre-warmed (at 37 °C) buffer containing 2% fetal bovine serum, 50 U ml⁻¹ penicillin and 50 μ g ml⁻¹ streptomycin in RPMI medium.

The BV2 microglial cell line has been maintained in the Yankner laboratory for more than 20 years and stored long-term in liquid nitrogen at -180 °C. After revival, the BV2 cells were authenticated based on their characteristic microglial morphology (small, round to slightly elongated shape, clear cytoplasm and occasional short processes) as well as positive immunolabelling for the microglial markers CD11b and Iba1. Mycoplasma contamination testing was not done.

Microglial A β uptake and degradation assays. Microglial A β uptake and degradation assays were done as previously described⁶⁸. Human amyloid A β 1-42 was purchased from Anaspec (AS-20276). Next, 1 mg of A β 1-42 peptide was dissolved in 80 μ l 1% NH₄OH, followed by dilution with PBS to 1 mg ml⁻¹ (stock) and storage at -80 °C. Oligomeric A β 1-42 was prepared by resuspending the stock solution in DMEM/F12 to 500 μ g ml⁻¹ (100 μ M) and overnight incubation at 4 °C. On day 3, the medium was replaced with DMEM/F12 containing 2% FBS and A β 42 oligomers diluted to a final concentration of 2 μ g ml⁻¹ (0.4 μ M). To assess A β 42 uptake, cells were incubated for 3 h at 37 °C, followed by three washes with 1 \times PBS and fixation with 4% PFA for 15 min. To assess microglial A β 42 degradation, cells incubated with A β 42 oligomers for 3 h were first washed three times with warm medium. The cells were then incubated with warm medium devoid of A β 42 for an extra 3 h. They were then washed with 1 \times PBS and fixed with 4% PFA for 15 min. The fixed cells were washed twice with PBS and blocked with 2% BSA, 2% FBS, 0.1% Triton X-100 in PBS for 1 h. Anti-Iba1 and anti-A β (6E10) antibodies, diluted 1:500 in the blocking buffer, were then added and incubated overnight at 4 °C. The next day, the cells were washed three times with PBS 1 \times and incubated with secondary antibodies (1:300 in blocking buffer) at room temperature for 2 h. Cells were washed three times with 1 \times PBS, then mounted and analysed by confocal microscopy. We also assessed A β 42 uptake and clearance by microglia using fluorescently labelled (HiLyte Fluor 555) human A β 1-42 (AnaSpec, AS-60480). The fluorescently labelled A β 42 was directly added to the medium containing 2% FBS to reach a concentration of 2 ng μ l⁻¹, and the uptake and degradation assays were conducted as detailed above.

Microglial stimulation and treatment with GSK3 β inhibitors.

To assess cytokine release, primary microglia isolated from control and Li-deficient mice were treated with 50 ng ml⁻¹ LPS on day 2 for 16 h followed by supernatant collection. Inflammatory cytokines were detected and measured using a mouse cytokine array kit (R&D Systems, ARY006). To assess the effects of GSK3 β inhibitors on microglial function, microglia were pretreated with 3 μ M CHIR99021 or 1 μ M of PF-04802367 on day 2 for 24 h before A β 42 uptake and clearance or cytokine-detection assays.

snRNA-seq

Sample preparation. We performed snRNA-seq on the hippocampus of 12-month-old 3xTg mice that were fed a Li-deficient ($n = 5$ mice) or chemically defined control ($n = 4$ mice) diet for five weeks. Mice were transcardially perfused with ice-cold PBS at a speed of 6 ml min⁻¹ for 8 min to repress the transcriptional response during the brain dissection and sample preparation^{69,70}. Hippocampal tissue was dissected on ice and flash frozen in liquid nitrogen. Both frozen hippocampal tissues were subsequently thawed together in 500 μ l HB buffer (0.25 M sucrose, 25 mM KCl, 5 mM MgCl₂, 20 mM Tricine-KOH, pH 7.8, 1 mM DTT, 0.15 mM spermine and 0.5 mM spermidine) and homogenized with the tight pestle of a dounce homogenizer in the same HB buffer with the addition of 0.32% of IGEPAL (Sigma) (average of 25–30 times per sample) on ice. Subsequently, single nuclei were diluted to 9 ml in HB buffer, passed through a 40- μ m filter and separated from debris and multinuclei by iodixanol gradient centrifugation. Specifically, we prepared a 50% iodixanol solution by diluting 60% iodixanol (Optiprep

density gradient medium, Sigma D1556) with diluent (150 mM KCl, 30 mM MgCl₂, 120 mM Tricine-KOH, pH7.8), and subsequently diluted them with HB buffer and supplemented with 0.04% BSA and 64 U ml⁻¹ RNasin Plus ribonuclease inhibitor (Promega, N2611) to prepare 40% iodixanol and 30% iodixanol. We layered 1 ml of 40% iodixanol in the bottom, 1 ml of 30% iodixanol in the middle and gently layered 9 ml of the diluted nuclei suspension on top of the 30% iodixanol layer. The three layers were visually confirmed to be distinct and were subjected to 18 min of 10,000g centrifugation. Single nuclei were carefully recovered from the 30% iodixanol layer in between the 30% and 40% interface. An aliquot was taken for trypan blue staining and visual inspection of nucleic morphology under a microscope, which showed a homogeneous size distribution and absence of major debris or doublets. The numbers of nuclei were determined initially by haemocytometer and subsequently confirmed with an automated counter. The remainder of the nucleic suspension was diluted for nuclei encapsulation and sequencing library preparation at the Harvard Single Cell Core, according to the 10X Genomics manual. The size and quality of the prepared libraries were confirmed on Agilent high-sensitivity TapeStation and the library was independently quantified by qPCR. The prepared libraries were sequenced by Nova-Seq S4 at the Harvard Biopolymers Facility, at an average coverage of 32,897 reads per nucleus (Supplementary Table 3). Sequencing data and individual animal metadata have been deposited at the NCBI Gene Expression Omnibus GSE272344 and linked to BioProject PRJNA1136488.

Single-nucleus RNA-seq quality control. We aligned the demultiplexed raw sequencing reads to the mouse genome (mm10 from 10X Genomics) using Cell Ranger (v.6.1.2)⁷¹, with the –include-introns option, to account for nuclear pre-mRNAs. The generated counts table was loaded to Seurat (v.4)⁷² to generate Seurat objects. Cells with more than 10% of reads being attributed to mitochondrial transcripts were filtered out. Cells that expressed fewer than 200 features (low-quality cells) or more than 8,000 features (apparent doublets) were also filtered out. These thresholds were determined by visual inspection of the distribution of features among cells (Seurat, VlnPlot) and are generally consistent with previous reports^{57,73}. The cells that passed quality controls were log-normalized using the NormalizeData function from Seurat with a scale factor of 10,000. Variable features were identified using the FindVariableFeatures function from Seurat with the vst selection method and 2,000 features. Data were scaled using ScaleData and principal component analysis (PCA) was performed using RunPCA with the identified variable features using Seurat. Nearest neighbours were found using FindNeighbors with dimension 1:30, which was determined by ElbowPlot following the Seurat manual. The number of clusters was determined by the FindClusters function using Seurat v.4. UMAP and TSNE were performed using RunUMAP and RunTSNE using Seurat with dimensions 1:30 and do.fast=TRUE parameter. Potential doublets were removed using DoubletFinder (v.3)⁷⁴ following the default parameters. After filtration, cluster-specific markers were determined using the FindAllMarkers function (Seurat v.4), with parameters only.pos = F, min.pct = 0.25 and max.cell.per.ident = 500.

Cell-type-specific annotation and differential gene expression analyses. Cell types were identified by cross-referencing the transcriptome of each individual cell to the Mouse Cell Atlas⁷⁵ and independently validated by confirming the expression of established cell-type-specific markers on a cluster-to-cluster basis. Violin and heat scatter plots to demonstrate the expression distribution of selected established markers were plotted using the VlnPlot and FeaturePlot functions of Seurat. Examples of cell-type markers include *Slc17a7* (excitatory neurons), *Prox1* (granule cells), *Gad1* and *Gad2* (inhibitory neurons), *Mbp* (oligodendrocytes), *Aldoc*, *Aqp4* (astrocytes), *Pdgfra* (OPCs), *Vtn* (pericytes), *Cx3cr1* and *Tgfb1* (microglia), *Cldn5* and *Flt1* (endothelial cells), *Prlr* and *Folr1* (choroid plexus cells; Supplementary Fig. 4).

Cell type-specific abundance and differential gene expression analyses were performed on the main cell types (excitatory neurons, inhibitory neurons, granule cells, microglia, astrocytes, oligodendrocytes, OPCs and endothelial cells). Clusters of the same cell types were combined to increase the statistical power, as described previously^{69,70,76}, and clusters with mixed cell types (less than 80% homogenous) were removed for cell-type-specific analyses. The relative abundance of each cell type was computed by dividing the number of cells of the particular cell type by the total number of cells. Two-tailed unpaired Student's *t*-tests were done to determine whether there were significant differences in the relative abundance of each cell type between the control and Li-deficient conditions. DEGs were computed by the MAST⁷⁷ test in Seurat. Genes expressed in fewer than 1% of the cells in each cell type were filtered out. All the DEGs (FDR < 0.05) are reported in Supplementary Table 4. DEGs with FDR < 0.05 and |log₂fold change| > 0.1 were used for Gene Ontology enrichment analyses using Metascape⁷⁸ v.3.5.20240101. The heat scatter plot for DEGs (Fig. 3d) was generated using the FeaturePlot function of Seurat.

Purified microglia RNA-seq

Purification of microglia. Li-deficient or control wild-type and 3xTg mice were perfused transcardially using PBS at 4 °C. The cortex and hippocampus were quickly dissected and pooled, then minced using a scalpel, before transferring to 5 ml dissection buffer (HBSS without calcium and magnesium) and Protector RNase inhibitor (Sigma) at 4 °C in a dounce homogenizer. Brain samples were dounced 20 times with a loose pestle and 10 times with a tight pestle. The cell suspension was passed through a pre-wetted 70-µm cell strainer into a pre-chilled 15 ml tube. Cells were then spun down at 300g for 10 min at 4 °C. Cell pellets were resuspended in 10 ml ice-cold 40% Percoll and centrifuged at 800g for 20 min at 4 °C. Myelin debris was removed by vacuum suction and the cell pellet was washed with 5 ml ice-cold HBSS and spun again for 5 min at 300g at 4 °C. The pellets were resuspended in 180 µl ice-cold MACs buffer (0.5% BSA, 2 mM EDTA, Protector RNase inhibitor in PBS) with 20 µl of CD11b microbeads (Miltenyi Biotec, 130-049-601) and incubated on ice for 15 min. After incubation, 1 ml of MACs buffer was added to samples and cells were centrifuged for 5 min at 300g and 4 °C. Microglia were then isolated using LS columns with QuadroMACS Separator following the manufacturer's instructions. In brief, LS columns were pre-washed three times with 3 ml MACs buffer. Samples were resuspended in 500 µl MACs buffer and transferred to LS columns, followed by three more washes with 3 ml MACs buffer. Finally, microglia were released with 5 ml MACs buffer (without EDTA), then used for RNA extraction.

Microglial RNA sequencing quality control and analysis. Total microglial RNA was extracted from MACs-purified microglia using RNaZol RT (Sigma, R4533). RNA extracted from each microglial preparation was quantified using an Agilent Tapestation 4200 instrument, with a corresponding Agilent Tapestation High Sensitivity RNA assay (5067-5579). The samples were normalized to 4 ng of input in 9.5 µl, and the polyadenylated mRNA was selected for using 3' SMART-Seq CDS Primer II A as part of the Takara SMART-Seq v.4 Ultra Low Input RNA (634894) workflow, which generated cDNA. From there, an Agilent Bioanalyzer High Sensitivity DNA assay (5067-4626) was used to quantify the cDNA concentration. Libraries were obtained using the Illumina NexteraXT kit (FC-131-1096). Adapter ligation, indexing and amplification were done subsequently as part of the same workflow. After amplification, residual primers were eluted away using KAPA Pure Beads (07983298001) in a 0.6× SPRI-based clean-up. The resulting purified libraries were run on an Agilent 4200 Tapestation instrument, with a corresponding Agilent D5000 ScreenTape assay (5067-5588 and 5067-5589) to visualize the libraries and check the size and concentration of each library. Molarity values obtained from this assay were used to normalize all samples in equimolar ratio for

Article

one final pool. The pooled library was denatured and loaded onto a single lane of an Illumina NovaSeq 6000 S4 flow cell to generate 100-bp paired-end reads. The pool was loaded at 200 pM (normalized to 1 nM pre-denaturation), with 1% PhiX spiked in as a sequencing control. The base-call files were demultiplexed through the Harvard BPF Genomics Core pipeline and the resulting fastq files were used in subsequent analysis. Raw RNA-sequencing data in FASTQ format were subjected to quality assessment using FastQC (v.0.11.9) and sequencing reads were aligned to mouse genome (mm10) using a STAR aligner⁷⁹ with the following options: --outFilterMismatchNmax 999 --outFilterMismatchNoverLmax 0.04 --alignSJDBoverhangMin 1 --alignSjoverhangMin 8 --outFilterMultimapNmax 20 --outFilterType BySJout --alignIntronMin 20 --alignIntronMax 1000000 --alignMates GapMax 1000000. Microglia RNA-seq yielded an average of 100 million uniquely mapped reads for each sample, and gene expression levels were quantified using htseq-count⁸⁰. To reduce the computational burden and focus on biologically relevant genes, we initially prefiltered the count data. Genes were retained if they had at least five counts in at least three samples. To validate the purity of the isolated microglia, we determined that microglial markers (*Csf1r*, *P2ry12* and *Tmem119*) were strongly enriched, whereas neuronal (*Map2* and *Nsg2*), astrocytic (*Gfap* and *Aldh1l1*) and oligodendrocyte (*Olig2* and *Mog*) marker genes were negligibly expressed (Supplementary Fig. 7b,c). We also verified that markers of ex vivo microglia activation⁸¹ (*Fos*, *Jun*, *Hspa1a* and *Zfp36*) were minimally expressed in our samples (Supplementary Fig. 7b,c). Differential gene expression analysis was done using DESeq2 (ref. 82) to identify DEGs between Li-deficient and control microglia, with an adjusted *P* value cut-off of 0.05 (Supplementary Tables 10 and 11). Upregulated and downregulated DEGs from Li-deficient wild-type and 3xTg microglia were further analysed for overlapping DEGs, and the overlapping DEGs were subjected to Gene Ontology enrichment analysis using Metascape⁷⁸ v.3.5.20240101. Results are summarized in Fig. 4a and provided in Supplementary Table 12.

Ingenuity Pathway Analysis. Signalling pathway and molecular network analyses were done on DEGs identified from the snRNA-seq and microglia RNA-seq datasets (FDR < 0.05) using Ingenuity Pathway Analysis (IPA)⁸³. Significantly enriched pathways and disease or function annotations were identified and ranked based on the FDR, calculated using a one-sided Fisher's exact test followed by a Benjamini–Hochberg correction for multiple comparisons. To visualize the results, the top pathway-enriched DEGs were integrated into a signalling network using IPA's build and overlay function (Extended Data Fig. 4b,c).

RNA-seq of hippocampus from 3xTg mice treated with LiO

RNA extraction. Twelve-month-old 3xTg mice that were treated with 4.3 μ M LiO ($n = 9$ females) or vehicle (water; $n = 9$ females) from 6 to 12 months of age were transcardially perfused with cold PBS 1× and the hippocampi were rapidly dissected and snap frozen. The total hippocampal RNA was extracted using Trizol reagent (Ambion, 15596018) and purified using a Direct-zol RNA Mini Prep kit (Zymo Research, R2050) according to the manufacturer's instructions. RNA integrity and concentration were assayed using an Agilent 2100 Bioanalyzer instrument. All RNA samples had an RNA integrity number of more than 8.2.

RNA library preparation and sequencing. Libraries were prepared using Illumina TruSeq Stranded mRNA sample-preparation kits from 500 ng of purified total RNA according to the manufacturer's protocol. The finished dsDNA libraries were quantified using a Qubit fluorometer, Agilent TapeStation 2200, and RT-qPCR using a Kapa Biosystems library quantification kit according to the manufacturer's protocols. Uniquely indexed libraries were pooled and sequenced on an Illumina NextSeq 500 instrument with paired-end 75-bp reads by the Dana-Farber Cancer Institute Molecular Biology Core Facilities.

Samples were pooled with multiple samples per lane and sequenced. There were two sequencing batches (batch 1, $n = 5$ mice per group; batch 2, $n = 4$ mice per group).

RNA sequencing quality control and quantification of gene expression. Quality control of sequencing reads (Supplementary Table 14) was done using FastQC v.0.11.5 (<https://www.bioinformatics.babraham.ac.uk/projects/fastqc/>). Reads were aligned to the Mouse GRCm38 genome with GENCODE M21 gene models using STAR⁷⁹ v.2.7.0f with options --outSAMunmapped Within --alignSJDBoverhangMin 1 --alignSjoverhangMin 8 --outFilterMultimapNmax 20 --outFilterType BySJout --alignIntronMin 20 --alignIntronMax 1000000 --alignMates GapMax 5000000 --twoPassMode Basic. The expression of genes was quantified as gene counts using STAR at the same time as alignment with option --quantMode GeneCounts.

Gene-expression normalization and covariate adjustment. Gene counts were input to edgeR. Genes were deemed expressed if at least $n = 9$ samples (where n is the group size) had more than one count per million (CPM). Genes not satisfying these criteria were removed, keeping the original library sizes. This filtering retained $n = 14,862$ expressed genes out of 55,536 annotated genes for subsequent analyses. Counts were then normalized using the TMM method in edgeR. Finally, log(CPM) values were calculated for analyses other than differential expression.

To adjust gene expression for covariates, we fit the linear regression model for each gene and cohort separately using lm() in R: gene expression - group + covariates, where gene expression is log(CPM), and using the group and covariates: factor, two levels: LiO and water (reference level), covariates (sequencing batch (factor, two levels)) and one RUV with residuals (RUVr) covariate (continuous). The final normalized and adjusted gene-expression values were derived from adding the regression residuals to the estimated effect of the group level to preserve the effect of the group on expression. These normalized and adjusted gene-expression values were used to perform gene–gene regression analysis and gene–gene group regression analysis, and to visualize gene expression.

To adjust for technical variation, we used the RUVr method⁸⁴ implemented in the RUVSeq v.1.18.0 Bioconductor package. We performed a first pass edgeR analysis, up to and including the glmFit() step with the covariates listed above, excluding the RUVr covariates. Then we used residuals() with argument type = 'deviance' to obtain a matrix of deviance residuals. The specified number of unwanted factors (RUVr covariates) used in final analyses were then estimated by the RUVr function using log(CPM) expression values and the residuals. The number of unwanted factors was selected based on separation of groups in PC plots using normalized and adjusted gene-expression values and checking that histograms of differential expression *P* values showed a uniform or anti-conservative pattern.

Differential expression and gene set enrichment analysis. Differential expression analysis between groups with covariate adjustment using the covariates listed above was performed for expressed genes using edgeR (estimateDisp, glmFit and glMLRT with default arguments) in R. Genes were considered differentially expressed if FDR < 0.05. Gene Ontology enrichment analysis was done separately for upregulated genes and downregulated genes using Metascape v.3.5.20240101 and is summarized in Supplementary Table 15 and Fig. 5f.

GWAS-DEG enrichment analysis

Before doing the GWAS-DEG enrichment analysis, we converted the mouse gene symbols to their human orthologues, using a two-step process. First, we used the alias2SymbolTable function in the Limma R package⁸⁵ v.3.58.1 to map any gene aliases to their corresponding main symbols. Subsequently, the resulting gene symbols were converted to

human orthologues using the MGI orthologue table⁸⁶. If there were multiple mapping candidates, all possible conversions were applied. For example, if a mouse gene had multiple human orthologues, records with all the relevant human gene symbols were generated. This standardized gene nomenclature enabled cross-species comparisons in subsequent analyses.

To do the GWAS-DEG enrichment analysis for microglia isolated from Li-deficient mice, we used MAGMA⁸⁷ v.1.10. The gene set of DEGs identified by microglia bulk RNA-seq analysis was used and the summary statistics from the GWAS catalogue AD (accession ID: MONDO_0004975)⁸⁸ were obtained and formatted for MAGMA input. The GWAS catalogue AD contains GWAS records from multiple studies. If multiple records were found for the same variant, we retained the entry with the lowest *P* value. Gene-set analysis was conducted using the default MAGMA settings, with multiple testing correction applied to account for the number of gene sets tested. Enrichment results were considered significant at a false discovery rate (FDR) of 0.05.

Overlap of mouse and human DEGs

To assess the overlap between DEGs derived from our transcriptomic analyses and DEGs derived from the analysis of human brain samples with varying degrees of AD pathology¹⁵ (Fig. 3d), we first converted mouse gene symbols to their human orthologues, as described above. We matched the cell types analysed in our mouse studies with those analysed in humans¹⁵. To assess the statistical significance of the overlap between the two DEG sets, we did a Fisher's exact test. To control for multiple comparisons arising from the analysis of different cell types and DEG directions (upregulated and downregulated), we adjusted the *P* values using the Benjamini–Hochberg procedure. Two sets of adjusted *P* values were calculated (Fig. 3d and Supplementary Table 8): one set for the overlap of genes upregulated in both datasets (indicated in red), and another for the overlap of genes downregulated in both datasets (indicated in blue).

Proteome analysis by mass spectrometry

The proteomic analysis was done at the Harvard Center for Mass Spectrometry. Hippocampal homogenates from Li-deficient and control 3xTg mice containing an equal amount (100 µg) of protein were reduced with 200 mM tris[2-carboxyethyl] phosphine (TCEP) at 55 °C for 1 h, then alkylated with 375 mM iodoacetamide at room temperature for 30 min in the dark. Proteins were precipitated using the methanol/chloroform/water precipitation method and then digested with trypsin overnight at 37 °C. TMT labelling of digested samples was done according to the manufacturer's instructions (ThermoFisher). In brief, TMT labelling reagents were dissolved with 41 µl anhydrous acetonitrile, and an equal volume of TMT reagent mix was added to each sample. After incubation for 1 h at room temperature, the reaction was quenched with 8 µl of 5% hydroxylamine. Equal amounts of peptides from each sample were combined and dried in a SpeedVac. The peptides were then separated using an Agilent 1200 HPLC system with a PolyWAX LP column (PolyLC), 200 × 2.1 mm, 5 µm and 300 Å running under electrostatic repulsion–hydrophilic interaction chromatography (ERLIC) mode conditions. Peptides were separated across a 90-minute gradient from 0% buffer A (90% acetonitrile, 0.1% acetic acid) to 75% buffer B (30% acetonitrile, 0.1% formic acid) with 20 fractions collected by time. Each fraction was dried in a SpeedVac and resuspended in 0.1% formic acid solution before analysis by mass spectrometry. Each ERLIC fraction was submitted for a single liquid chromatography–tandem mass spectrometry (LC-MS/MS) experiment that was done on a Q Exactive HF-X High Resolution Orbitrap (Thermo Fisher) coupled with an Ultimate 3000 nanoLC (Thermo Fisher) at the Harvard Center for Mass Spectrometry. Peptides were first isolated on a trapping cartridge (300 µm × 5 mm PepMap Neo C18 trap cartridge, Thermo Scientific) before separation on an analytical column (µPAC, C18 pillar surface, 50-cm bed, Thermo Scientific). The LC gradient was

as follows: 2–27% in mobile phase B (0.1% formic acid in acetonitrile) for 70 min and increased to 98% mobile phase B for 15 min at a flow rate of 300 nL min⁻¹. The mass spectrometer operated in data-dependent mode for all analyses. Electrospray-positive ionization was enabled with a voltage of 2.1 kV. A full scan ranging from 400 to 1,600 *m/z* was done with a mass resolution of 12 × 10⁴ and an automated gain control (AGC) target set to 1 × 10⁶.

Proteomics quality control. The top three most intensive precursor ions from each scan were used for MS2 fragmentation (normalized collision energy of 32) at a mass resolution of 3.0 × 10⁴ and an AGC of 1 × 10⁵. The dynamic exclusion was set at 50 s with a precursor isolation window of 1.2 *m/z*. Raw data were submitted for analysis in Proteome Discoverer 3.0 software (Thermo Scientific). The MS/MS data were searched against the UniProt reviewed *Mus musculus* (mouse) database along with known contaminants, such as human keratins and common lab contaminants. Sequest HT searches were performed using the following guidelines: a 10-ppm MS tolerance and 0.02-Da MS/MS tolerance; trypsin digestion with up to two missed cleavages; carbamidomethylation (+57.021 Da) on cysteine, TMT 6-plex tags on peptide amino termini and lysine residue (+229.163 Da) were set as static modification; oxidation (+15.995 Da) of methionine was set as variable modification; minimum required peptide length was set to ≥6 amino acids. At least one unique peptide per protein group was required to identify proteins. Of 13,404 proteins identified, only *n* = 3,392 proteins were identified with high confidence (MS2 spectra assignment, FDR < 0.01 on both protein and peptide level by applying the target-decoy database search by Percolator) and were included in the statistical analysis, as per the standard procedures of the Harvard Center for Mass Spectrometry^{89–91}. The sample labels were control (samples 1, 3, 5 and 7) and Li-deficient (samples 2, 4, 6 and 8) and were all 3xTg homozygous females, aged 15 months (treatment from 6 to 15 months of age). An ANOVA followed by Tukey's post-hoc test was used to assess differences in protein abundance between Li-deficient and control samples. *P* values were adjusted for multiple comparisons using the Benjamini–Hochberg method to control the FDR. Proteins with an adjusted *P* < 0.05 were considered differentially abundant (Supplementary Table 7). The proteins identified with high confidence and included in the statistical analysis are listed in Supplementary Table 7. All other proteins, identified with lower confidence, can be accessed from the files deposited at the ProteomeXchange Consortium through the PRIDE partner repository with the dataset identifier PXD063039. This represents 21 files, including one .msf file (containing all search results: peptide-spectrum matches, peptide groups, protein groups, modifications, scores, FDR and metadata) and 20 .raw files (containing MS1/2 spectra and metadata), one for each of the 20 fractions analysed by mass spectrometry.

Statistics and reproducibility

Statistical analysis was done using GraphPad software v.10.3.0 (507). The statistical tests used are noted in the figure legends. Throughout the paper, all tests are two sided and unpaired unless stated otherwise. A significance level of 0.05 was used to reject the null hypothesis. The sample size, age and sex of experimental animals, as well as the summary of each statistical test (including degrees of freedom, confidence intervals and *P* values) can be found in the Source Data file. All animal experiments were done once per condition using biologically independent samples (individual animals), with group sizes indicated in the corresponding figure legends. Representative immunolabelling images shown in the figures are from one animal per group, selected from multiple animals that consistently showed similar results.

Reporting summary

Further information on research design is available in the Nature Portfolio Reporting Summary linked to this article.

Data availability

The snRNA-seq, microglia RNA-seq and LiO RNA-seq data have been deposited in the Gene Expression Omnibus repository (GSE272344, GSE275326 and GSE295788). The mass-spectrometry proteomics data have been deposited in the ProteomeXchange Consortium through the PRIDE⁹² partner repository with the dataset identifier PXD063039. The MS/MS proteomic data were searched against the UniProt *Mus musculus* protein database (FASTA format, including isoforms) and were downloaded on 17 July 2022. For the GWAS DEG enrichment analysis using MAGMA, summary statistics for Alzheimer's disease (accession ID: MONDO_0004975) were obtained from the GWAS Catalog (https://www.ebi.ac.uk/gwas/efotraits/MONDO_0004975). Clinico-pathological data on post-mortem human samples from ROSMAP can be requested at <https://www.radc.rush.edu>. Source data are provided with this paper.

Code availability

The code used in this study is available from the corresponding author upon reasonable request.

58. Bennett, D. A. et al. Religious Orders Study and Rush Memory and Aging Project. *J. Alzheimers Dis.* **64**, S161–S189 (2018).
59. Bennett, D. A. et al. Decision rules guiding the clinical diagnosis of Alzheimer's disease in two community-based cohort studies compared to standard practice in a clinic-based cohort study. *Neuroepidemiology* **27**, 169–176 (2006).
60. Bennett, D. A. et al. Natural history of mild cognitive impairment in older persons. *Neurology* **59**, 198–205 (2002).
61. Ihara, Y., Abraham, C. & Selkoe, D. J. Antibodies to paired helical filaments in Alzheimer's disease do not recognize normal brain proteins. *Nature* **304**, 727–730 (1983).
62. Selkoe, D. J., Abraham, C. R., Podlisny, M. B. & Duffy, L. K. Isolation of low-molecular-weight proteins from amyloid plaque fibers in Alzheimer's disease. *J. Neurochem.* **46**, 1820–1834 (1986).
63. Xu, J. et al. Evidence for widespread, severe brain copper deficiency in Alzheimer's dementia. *Metalomics* **9**, 1106–1119 (2017).
64. Ramos, P. et al. Alkali metals levels in the human brain tissue: anatomical region differences and age-related changes. *J. Trace Elem. Med. Biol.* **38**, 174–182 (2016).
65. Squitti, R. et al. Copper imbalance in Alzheimer's disease: meta-analysis of serum, plasma, and brain specimens, and replication study evaluating ATP7B gene variants. *Biomolecules* **11**, 960 (2021).
66. Hutchinson, R. W. et al. Imaging and spatial distribution of β-amyloid peptide and metal ions in Alzheimer's plaques by laser ablation-inductively coupled plasma-mass spectrometry. *Anal. Biochem.* **346**, 225–233 (2005).
67. Teich, A. F., Patel, M. & Arancio, O. A reliable way to detect endogenous murine β-amyloid. *PLoS ONE* **8**, e55647 (2013).
68. Griciuc, A. et al. Alzheimer's disease risk gene CD33 inhibits microglial uptake of amyloid beta. *Neuron* **78**, 631–643 (2013).
69. Kalish, B. T. et al. Single-cell transcriptomics of the developing lateral geniculate nucleus reveals insights into circuit assembly and refinement. *Proc. Natl. Acad. Sci. USA* **115**, E1051–E1060 (2018).
70. Qiu, C. et al. Cis P-tau underlies vascular contribution to cognitive impairment and dementia and can be effectively targeted by immunotherapy in mice. *Sci. Transl. Med.* **13**, eaaz7615 (2021).
71. Zheng, G. X. Y. et al. Massively parallel digital transcriptional profiling of single cells. *Nat. Commun.* **8**, 14049 (2017).
72. Hao, Y. et al. Integrated analysis of multimodal single-cell data. *Cell* **184**, 3573–3587 (2021).
73. Yang, A. C. et al. A human brain vascular atlas reveals diverse mediators of Alzheimer's risk. *Nature* **603**, 885–892 (2022).
74. McGinnis, C. S., Murrow, L. M. & Gartner, Z. J. DoubletFinder: doublet detection in single-cell RNA sequencing data using artificial nearest neighbors. *Cell Syst.* **8**, 329–337 (2019).
75. Sun, H., Zhou, Y., Fei, L., Chen, H. & Guo, G. scMCA: a tool to define mouse cell types based on single-cell digital expression. *Methods Mol. Biol.* **1935**, 91–96 (2019).
76. Pálavics, R. et al. Molecular hallmarks of heterochronic parabiosis at single-cell resolution. *Nature* **603**, 309–314 (2022).
77. Finak, G. et al. MAST: a flexible statistical framework for assessing transcriptional changes and characterizing heterogeneity in single-cell RNA sequencing data. *Genome Biol.* **16**, 278 (2015).
78. Zhou, Y. et al. Metascape provides a biologist-oriented resource for the analysis of systems-level datasets. *Nat. Commun.* **10**, 1523 (2019).
79. Dobin, A. et al. STAR: ultrafast universal RNA-seq aligner. *Bioinformatics* **29**, 15–21 (2013).
80. Anders, S., Pyl, P. T. & Huber, W. HTSeq—a Python framework to work with high-throughput sequencing data. *Bioinformatics* **31**, 166–169 (2015).
81. Marsh, S. E. et al. Dissection of artifactual and confounding glial signatures by single-cell sequencing of mouse and human brain. *Nat. Neurosci.* **25**, 306–316 (2022).
82. Love, M. I., Huber, W. & Anders, S. Moderated estimation of fold change and dispersion for RNA-seq data with DESeq2. *Genome Biol.* **15**, 550 (2014).
83. Krämer, A., Green, J., Pollard, J. Jr & Tugendreich, S. Causal analysis approaches in Ingenuity Pathway Analysis. *Bioinformatics* **30**, 523–530 (2014).
84. Risso, D., Ngai, J., Speed, T. P. & Dudoit, S. Normalization of RNA-seq data using factor analysis of control genes or samples. *Nat. Biotechnol.* **32**, 896–902 (2014).
85. Ritchie, M. E. et al. limma powers differential expression analyses for RNA-sequencing and microarray studies. *Nucleic Acids Res.* **43**, e47 (2015).
86. Baldarelli, R. M. et al. Mouse Genome Informatics: an integrated knowledgebase system for the laboratory mouse. *Genetics* **227**, iyae031 (2024).
87. de Leeuw, C. A., Neale, B. M., Heskes, T. & Posthuma, D. The statistical properties of gene-set analysis. *Nat. Rev. Genet.* **17**, 353–364 (2016).
88. Sollis, E. et al. The NHGRI-EBI GWAS Catalog: knowledgebase and deposition resource. *Nucleic Acids Res.* **51**, D977–D985 (2023).
89. Elias, J. E. & Gygi, S. P. Target-decoy search strategy for increased confidence in large-scale protein identifications by mass spectrometry. *Nat. Methods* **4**, 207–214 (2007).
90. Chen, M. et al. Common proteomic profiles of induced pluripotent stem cell-derived three-dimensional neurons and brain tissue from Alzheimer patients. *J. Proteomics* **182**, 21–33 (2018).
91. Lee, H.-K. et al. Three dimensional human neuro-spheroid model of Alzheimer's disease based on differentiated induced pluripotent stem cells. *PLoS ONE* **11**, e0163072 (2016).
92. Perez-Riverol, Y. et al. The PRIDE database at 20 years: 2025 update. *Nucleic Acids Res.* **53**, D543–D553 (2025).

Acknowledgements We thank A. Johnston, A. Stebbins and J. Seravalli for assistance with ICP-MS; M. Chen for assistance with mass spectrometry; S. Valentin and A. Thompson for assistance with tissue processing; G. Klein for assistance with sample selection; and S. Nadarajan for technical assistance. This work was supported by NIH grants RO1AG046174 and RO1AG069042 to B.A.Y.; K01AG051791 and DP2AG072437 to E.A.L.; P30AG10161, P30AG72975, R01AG15819, R01AG17917, U01AG46152 and U01AG61356 to D.A.B.; and grants from the Ludwig Family Foundation, the Glenn Foundation for Medical Research and the Aging Mind Foundation to B.A.Y.

Author contributions L.A. performed metallomic analysis of human and mouse brain by ICP-MS, with assistance from M.L., analysed human and mouse brain by quantitative immunohistochemistry, did cell-culture studies with BV2 cells and carried out mouse behavioural studies with assistance from M.L., S.E.H., E.K.L., P.R., M.Y. and S.S.H. Z.K.N. isolated and characterized primary microglia, did RNA sequencing and analysis of cytokine production and Aβ clearance, and did Li-Aβ equilibrium binding assays. C.Q. prepared single-nucleus libraries and did RNA sequencing. J.C., Z.K.N., C.Q., D.M.D., L.A. and B.A.Y. did computational and statistical analyses, with input from E.A.L., D.A.B. provided human brain samples and phenotypic data from the ROSMAP study. L.A. and B.A.Y. wrote the manuscript with input from all authors. B.A.Y. supervised all aspects of the work.

Competing interests The authors declare no competing interests.

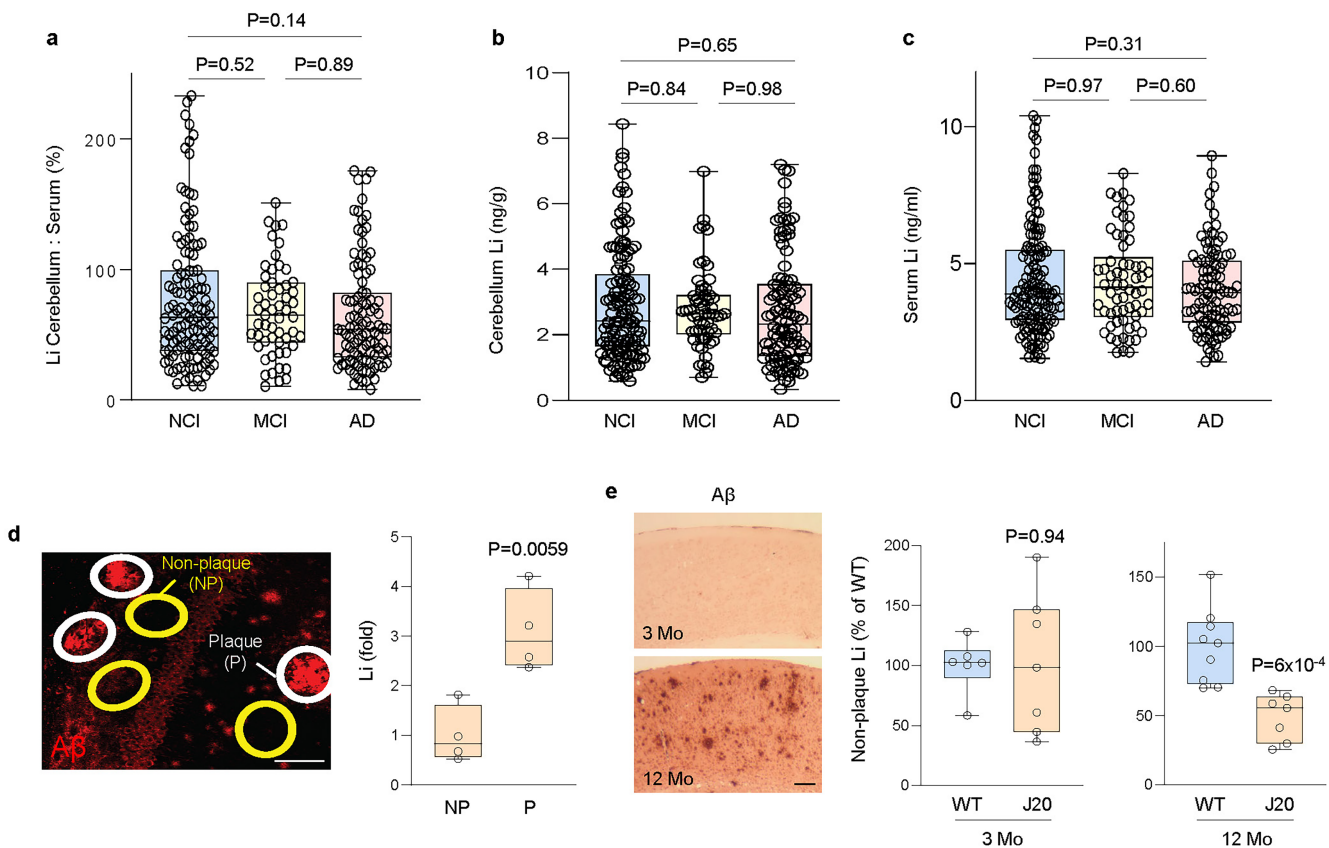
Additional information

Supplementary information The online version contains supplementary material available at <https://doi.org/10.1038/s41586-025-09335-x>.

Correspondence and requests for materials should be addressed to Bruce A. Yankner.

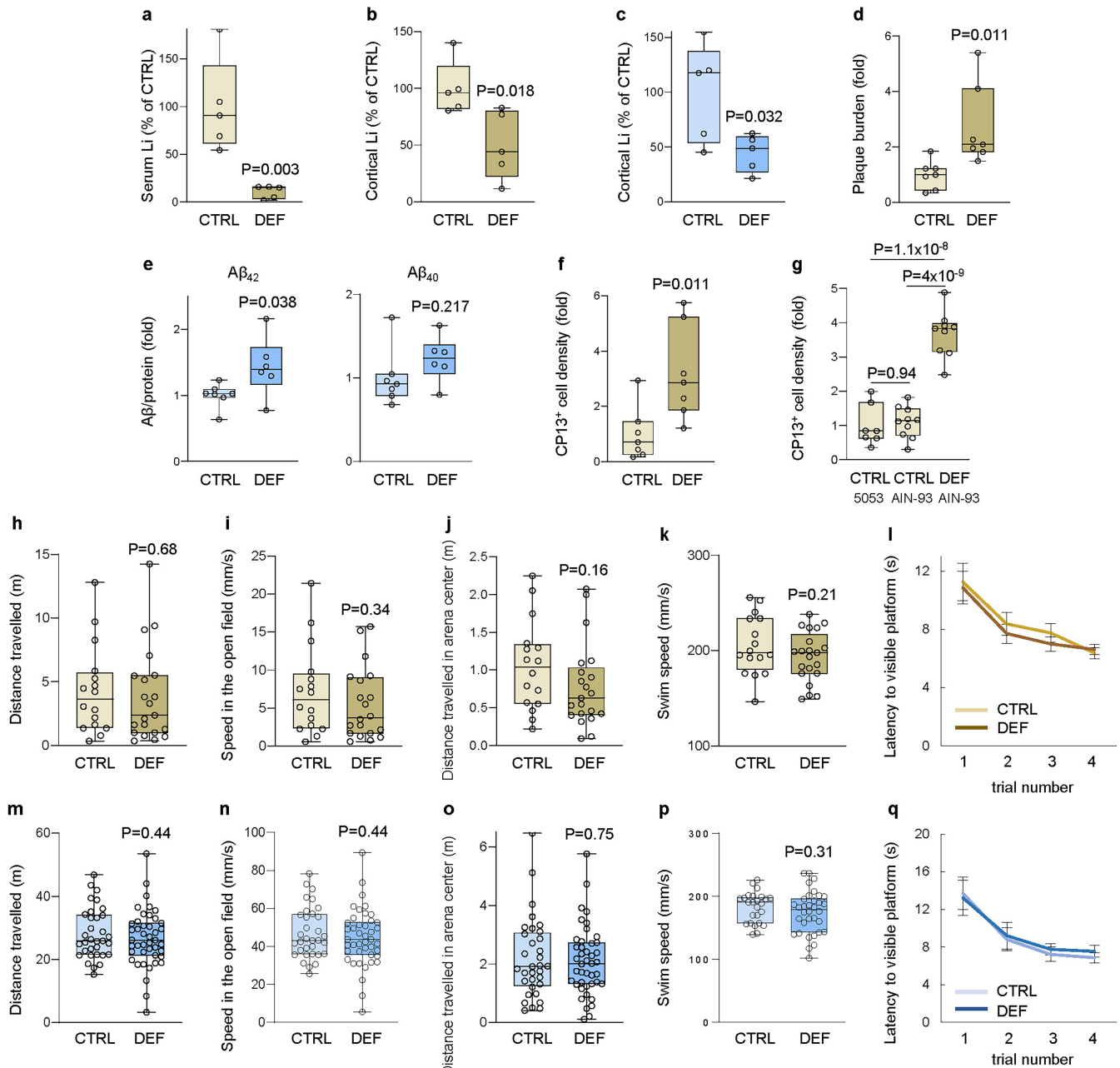
Peer review information *Nature* thanks Ashley Bush, Junmin Peng and the other, anonymous, reviewer(s) for their contribution to the peer review of this work. Peer review reports are available.

Reprints and permissions information is available at <http://www.nature.com/reprints>.



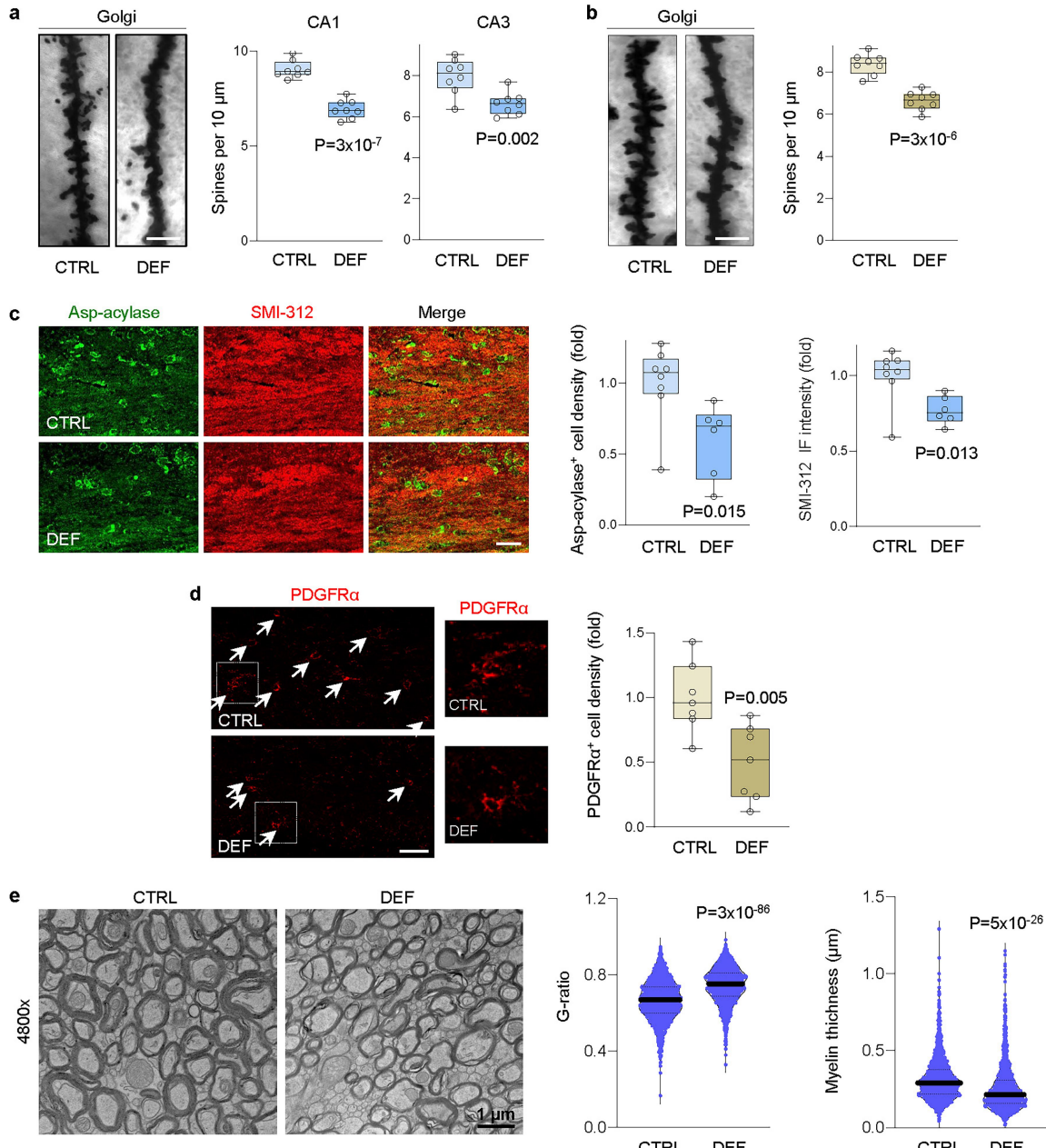
Extended Data Fig. 1 | Analysis of brain and serum lithium levels. **a–c**, Li cortex-to-serum ratio in the cerebellum (**a**), total Li levels in the cerebellum (**b**), and serum Li levels (**c**) are not significantly different in NCI, MCI, and AD. **a**, n = 125 NCI, n = 55 MCI and n = 101 AD cases. **b**, n = 129 NCI, n = 58 MCI and n = 102 AD cases. **c**, n = 141 NCI, n = 62 MCI and n = 101 AD cases. **d**, Lithium is concentrated in A β plaques in AD mice. A β immunolabeling in the cortex of 12-month-old J20 mice. Laser ablation ICP-MS was performed on an adjacent unfixed section to quantify Li in A β plaques (P; white circles) and in neighboring non-plaque regions (NP; yellow circles). The ratios of Li levels in P to NP regions are shown

(right) for n = 4 mice. **e**, A β immunolabeling of the cortex in J20 mice at 3 months of age, prior to onset of A β deposition, and 12 months of age, following widespread A β deposition. Cortical samples were subfractionated from 3-month-old (WT n = 6; J20 n = 7) and 12-month-old (WT n = 9, J20 n = 7) mice and Li in non-plaque fractions was measured by ICP-MS (middle and right panels). The data was normalized to the mean of WT. Box plots show individual values, median (line), box limits (25th–75th percentiles), and whiskers (min–max). P-values by one-way ANOVA with Tukey's post-hoc test (**a–c**) or two-tailed unpaired t-tests (**d,e**). Scale bars, 50 μ m.



Extended Data Fig. 2 | Lithium deficiency does not impair exploratory behavior or motor function in mice. **a–c**, Li levels measured by ICP-MS in serum (**a**) and cortex (**b**) of 15-month-old 3xTg mice, and in cortex of 20-month-old WT mice (**c**) fed CTRL or DEF diets (n = 5 per group). **d**, Amyloid plaque burden in the hippocampus of 12-month-old 3xTg mice after 5 weeks of CTRL or DEF diet (n = 7 per group). **e**, A β x-40 and A β x-42 levels in the hippocampus of 26-month-old WT mice (treated from 12–26 months of age; CTRL n = 7; DEF n = 6), normalized to total protein. **f**, Immunofluorescence for pSer202-tau (CP13) in CA1 of 12-month-old 3xTg mice after 5 weeks of CTRL or DEF diet (n = 7 per group). **g**, pSer202-tau pathology in 15-month-old 3xTg mice fed either standard PicoLab® Rodent Diet 20 (CTRL 5053, n = 7) or a chemically-defined control diet (CTRL AIN-93M, n = 10), compared to those on Li-deficient

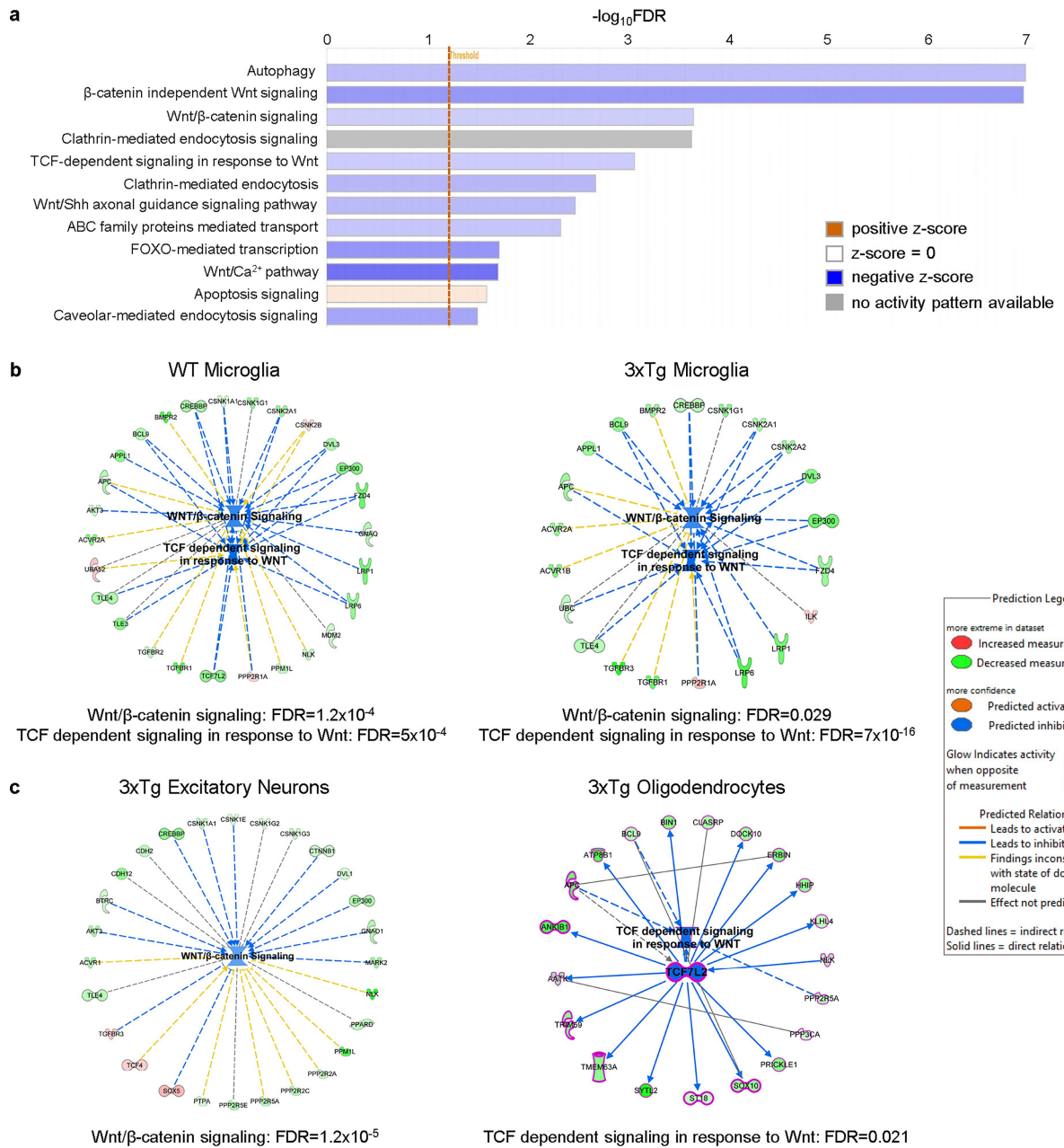
chemically-defined AIN-93M diet (n = 9) for 9 months. **h–l**, Behavioral testing of 3xTg mice fed CTRL or DEF diets from 6–13.5 months of age: Open field activity (**h–j**), Morris water maze swim speed (**k**), and latency to reach a visible platform elevated above water level (**l**). **m–q**, Behavioral testing of 20-month-old WT mice fed CTRL or DEF diets from 12–20 months of age: Open field activity (**m–o**), swim speed (**p**), and latency to reach a visible platform (**q**). **a–g**, Data normalized to CTRL group means. **l,q**, Data are the mean \pm s.e.m. **a–k,m–p**, Box plots show individual values, median (line), box limits (25th–75th percentiles), and whiskers (min–max). P-values by unpaired two-tailed t-test, except **g** (one-way ANOVA with Tukey's post-hoc test). **h–l**, n = 16 CTRL. **h,j–l**, n = 21 DEF. **i**, n = 20 DEF. **m–o**, n = 33 CTRL, n = 43 DEF. **p,q**, n = 25 CTRL, n = 34 DEF.



Extended Data Fig. 3 | Li deficiency results in loss of dendritic spines, axons and oligodendrocytes. **a**, Golgi staining and quantification (right) of dendritic spine density in hippocampus CA1 (middle) and CA3 (right) subdomains of WT mice fed Li-deficient (DEF) or CTRL diets from 12–24 months of age (n = 8 mice per group). **b**, Golgi staining and quantification of spine density (right) in the hippocampus CA1 of 12-month-old 3xTg mice after 5 weeks of CTRL or DEF diet (n = 8 mice/group) for 5 weeks. **c**, Immunolabeling and quantification (right) of mature oligodendrocytes (marker Aspartoacylase) and axons (marker SMI-312) in the corpus callosum of WT mice treated from 12–24 months of age (CTRL n = 8; DEF n = 6). **d**, Immunolabeling of OPCs (marker PDGFRα) in the hippocampus

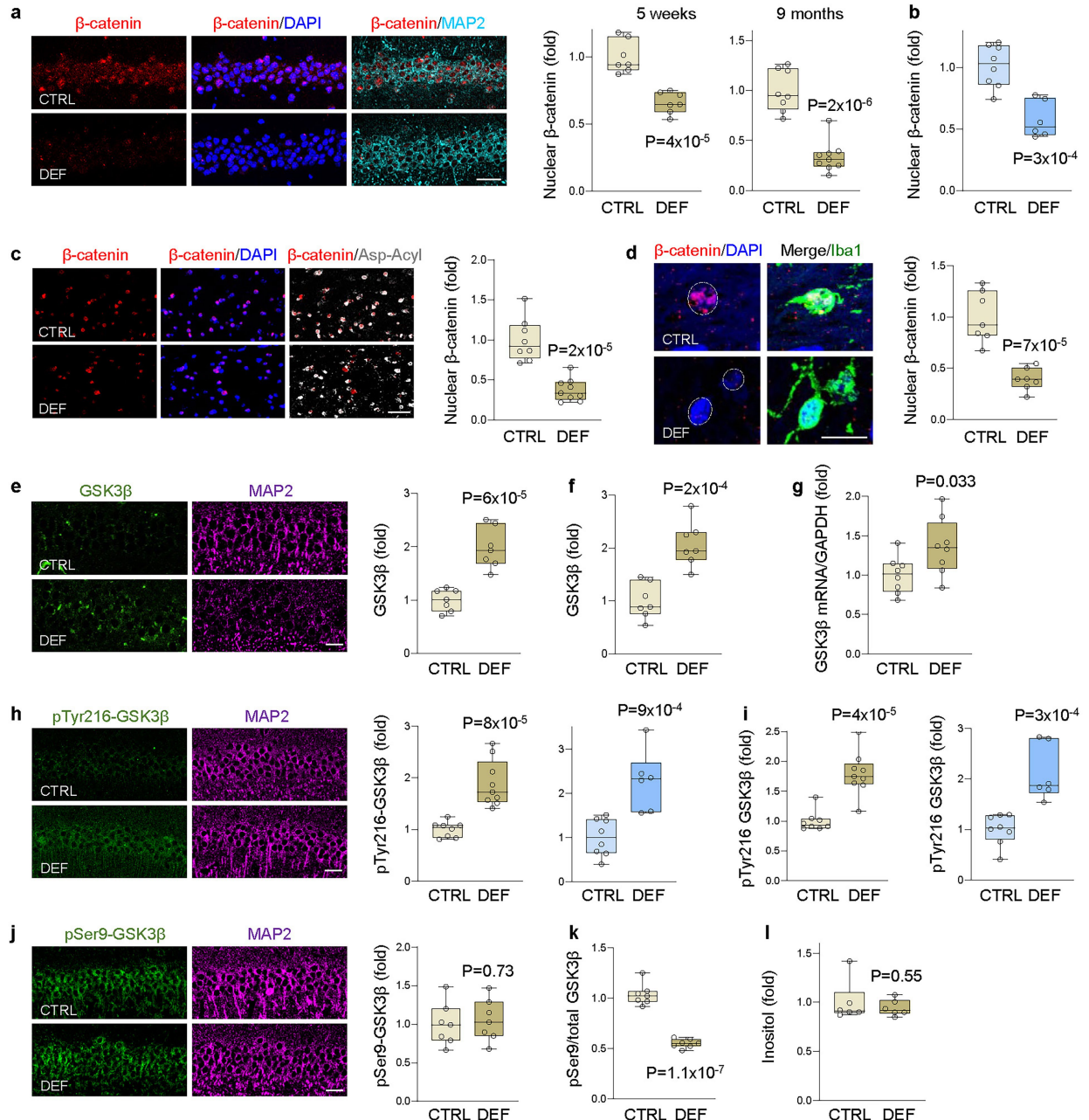
of 3xTg mice treated with CTRL and DEF diets from 6–15 months of age and quantification of OPC density (n = 7 per group). **e**, Lithium deficiency impairs myelin integrity. Transmission electron microscopy (left panel) showing structural abnormalities in the myelin of the corpus callosum of Li-deficient 3xTg mice (treatment from 6–12 months). Violin plots show g-ratios (middle) and myelin sheath thickness (right) for individual axons (CTRL n = 1,376; DEF n = 1,396; pooled from n = 8 mice per group). **a–d**, Box plots show individual values, median (line), box limits (25th–75th percentiles), and whiskers (min–max). **c,d**, The data was normalized to the mean of CTRL groups. **a–e**, P-values by unpaired two-tailed t-tests. Scale bars, 5 µm (**a,b**) or 25 µm (**c,d**).

Article



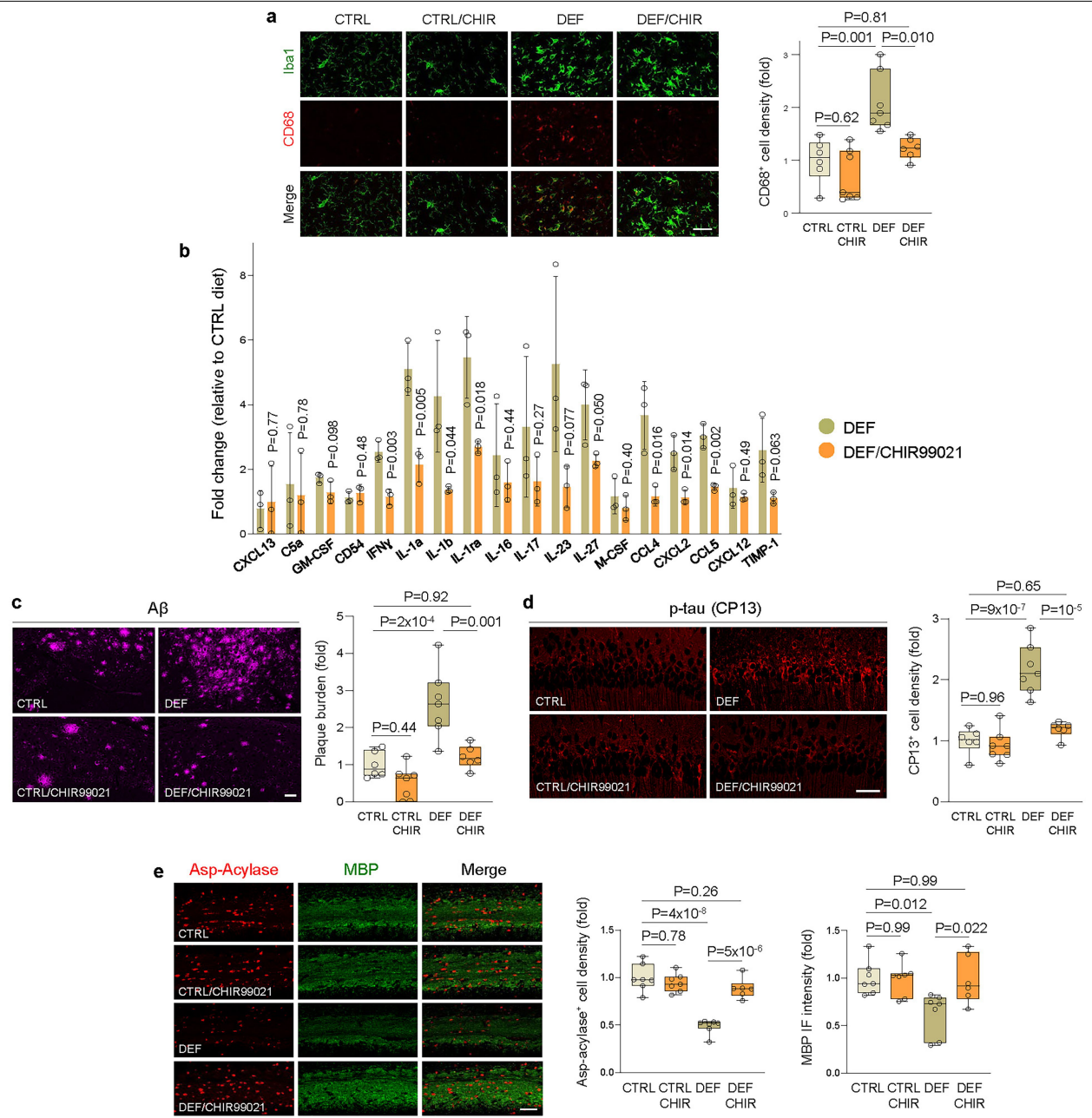
Extended Data Fig. 4 | Lithium deficiency and Wnt/β-catenin signaling. **a**, Pathways associated with Li deficiency in WT microglia. Wnt/β-catenin/TCF signaling is among the most significantly enriched signaling pathways and is predicted to be inhibited (predicted activation and inhibition are depicted as orange and blue, respectively). **b,c**, Functional network diagrams of Wnt/β-catenin/TCF signaling in Li-deficient WT and 3xTg microglia (**b**), and in excitatory neurons (**c**, left panel) and oligodendrocytes (**c**, right panel) from

Li-deficient 3xTg mice. In each network, associated DEGs (FDR < 0.05) are highlighted in red (upregulated) or green (downregulated). In **a**, color intensity reflects z-score strength. Analysis was performed using the Ingenuity Pathway Analysis (IPA) platform. False discovery rate (FDR) was determined using a one-sided Fisher's exact test followed by Benjamini-Hochberg correction for multiple comparisons.



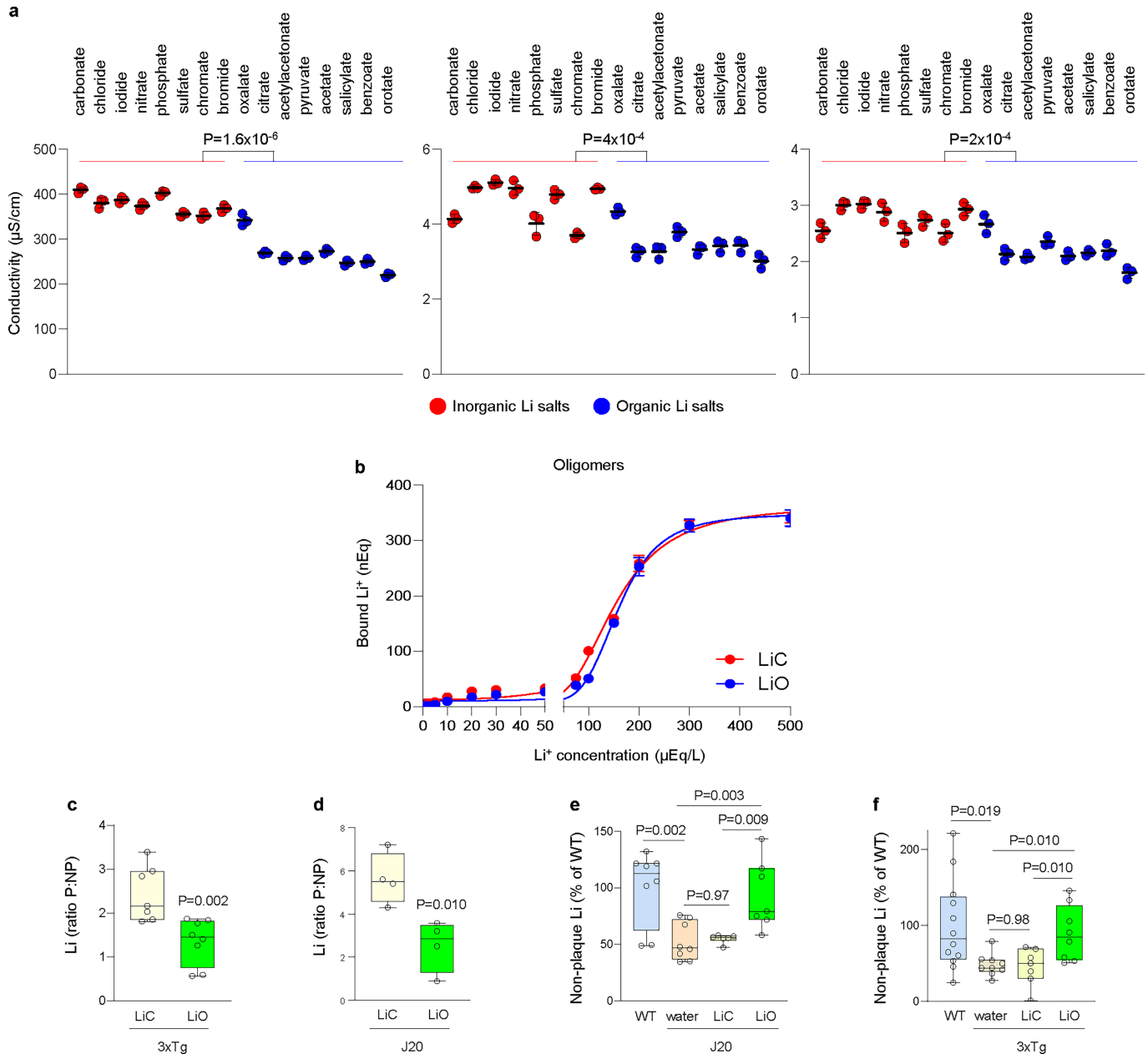
Extended Data Fig. 5 | Regulation of GSK3β and β-catenin by endogenous lithium. **a-d**, Immunolabeling and quantification of nuclear β-catenin in hippocampal CA1 neurons (**a, b**), corpus callosum oligodendrocytes (**c**), and microglia (**d**), co-labeled for MAP2, aspartoacylase (Asp-Acy), and Iba1, respectively. Additional β-catenin quantification shown for CA1 neurons after 5 weeks of DEF diet (**a**, middle). WT mice fed CTRL or DEF diets from 12–24 months of age shown in **b**. **e-f**, Immunolabeling (**e**, CA1 neurons) and quantification (**e**, right panel; **f**) of total GSK3β levels in CA1 neurons (**e**, MAP2 co-labeling) and oligodendrocytes (**f**, Aspartoacylase co-labeling) in 15-month-old 3xTg mice. **g**, *Gsk3b* mRNA in hippocampus of 12-month-old 3xTg mice was measured by qRT-PCR and normalized to *Gapdh*. **h-i**, pTyr216-GSK3β immunolabeling (**h**, 3xTg CA1 neurons) and quantification (**h**, middle and right panels; **i**) in CA1 neurons (**h**, MAP2 co-labeling) and oligodendrocytes (**i**, Aspartoacylase co-labeling) of 15-month-old 3xTg (**h**, middle; **i**, left) and 24-month-old WT

(**h**, right; **i**, right) mice on CTRL or DEF diets. **j-k**, Immunolabeling of pSer9-GSK3β (**j**, left) and quantification of absolute (**j**, right) and relative (**k**) levels of inhibitory pSer9-GSK3β in the hippocampal CA1 region of 15-month-old 3xTg mice. **l**, Inositol levels measured by mass spectrometry in the hippocampus of 15-month-old 3xTg mice. 3xTg mice were fed CTRL or DEF diets for 9 months (from 6–15 months of age: **a**, left and right; **c, d, f, h-l**) or 5 weeks (from 10.85–12 months of age: **b, h**, right; **i**, right). WT mice were treated from 12–24 months of age (**b**; **h**, right; **i**, right). Box plots show individual values, median (line), box limits (25th–75th percentiles), and whiskers (min-max). Data was normalized to CTRL group means. P-values by unpaired two-tailed *t*-test. WT CTRL n = 8, DEF n = 6. 3xTg CTRL (n = 6 in **l**, n = 7 in **a**, middle, **d-f, j, k**; n = 8 in **a**, right and **c, g-i**), 3xTg DEF (n = 6 in **l**, n = 7 in **a**, middle and **d-f, j, k**; n = 8 in **g**; n = 9 in **a**, right, and **c, h, i**). Scale bars, 25 μm.



Extended Data Fig. 6 | Inhibition of GSK3 β rescues Li deficiency. 12-month-old 3xTg mice, maintained on Li-deficient (DEF) or CTRL diets for 3 months, received CHIR99021 (CHIR; 50 mg/kg body weight, intraperitoneally) or vehicle, once daily for 14 days. **a**, Immunolabeling and quantification (right) of CD68 $^+$ /Iba1 $^+$ microglia density in the hippocampus. **b**, Cytokine and chemokine levels in the hippocampus ($n = 3$ mice per group), normalized to the mean of CTRL/Vehicle group. Means \pm s.d. shown. **c**, A β immunolabeling and quantification (right) of plaque burden in the hippocampus. **d**, Phospho-Ser202-tau (CP13 antibody) labeling and quantification (right) of CP13 $^+$ cell density in the hippocampus

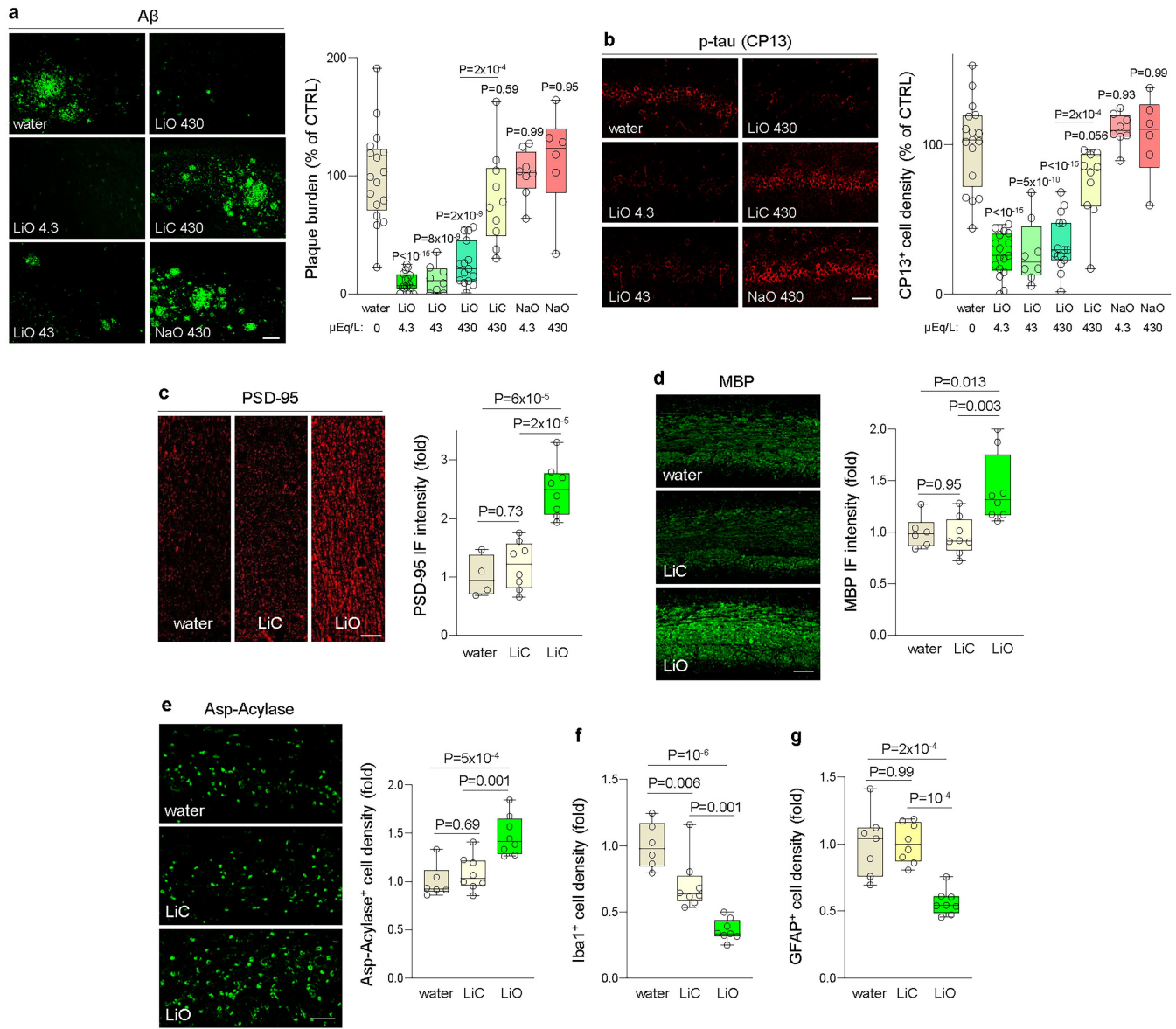
CA1 region. **e**, Immunolabeling of oligodendrocytes (Aspartoacylase $^+$) and myelin basic protein (MBP) labeling of myelin in the corpus callosum with quantification (middle and right) of oligodendrocyte density and MBP immunofluorescence (IF) intensity. **a,c-e**, Box plots show individual values, median (line), box limits (25th-75th percentiles), and whiskers (min-max). Data was normalized to CTRL/Vehicle and analyzed by two-way ANOVA with Tukey's post hoc (**a,c-e**) or two-tailed unpaired t-test (**b**); p-values indicated. Sample sizes: CTRL/Vehicle $n = 6$ (**a,c,d**), $n = 7 (**e**); CTRL/CHIR99021, DEF/Vehicle $n = 7$ (**a,c-e**); DEF/CHIR99021 $n = 6$ (**a,c-e**). Scale bars, 25 μ m.$



Extended Data Fig. 7 | Lithium orotate exhibits reduced conductivity and $\text{A}\beta$ binding compared to lithium carbonate. **a**, Organic Li salts show reduced conductivity relative to inorganic Li salts. Solution conductivities are shown for Li concentrations of 4.3 mEq/L (left panel), 43 $\mu\text{Eq}/\text{L}$ (middle panel), and 21.5 $\mu\text{Eq}/\text{L}$ (right panel). P-values by unpaired two-tailed t-tests comparing organic versus inorganic salts. **b**, Binding of LiO and LiC to $\text{A}\beta$ 42 oligomers across a concentration range of 0–500 $\mu\text{Eq}/\text{L}$ Li. **c,d**, LiO exhibits less sequestration in $\text{A}\beta$ plaques than LiC. The plaque to non-plaque (P/NP) Li ratios were quantified by laser ablation ICP-MS in 18-month-old 3xTg (**c**) and J20 (**d**) mice treated with LiO or LiC (4.3 μEq Li/L) for 7 days. 3xTg/LiC n = 7, 3xTg/LiO n = 8; J20/LiC n = 4; J20/LiO n = 4. **e,f**, Treatment with LiO achieves higher Li

levels in non-plaque fractions relative to treatment with LiC. Subfractionation of the hippocampus was performed in 18-month-old J20 (**e**) and 3xTg (**f**) mice that were administered LiO or LiC (4.3 μEq Li/L) for 7 days. Age-matched WT mice without $\text{A}\beta$ deposition served as controls. **e**, WT n = 8, J20 n = 8, J20/LiC n = 6, J20/LiO n = 7. **f**, WT n = 12, 3xTg n = 9, 3xTg/LiC n = 7, 3xTg/LiO n = 8. **a,b**, Shown are means \pm s.d. for n = 3 independent solution replicates (**a**) or n = 3 biological replicates (**b**). **c,f**, Box plots show individual values, median (line), box limits (25th-75th percentiles), and whiskers (min-max). Data was normalized to the mean of NP (**c,d**) or WT (**e,f**). P-values by unpaired two-tailed t-tests (**a,c,d**; pre-planned comparisons: WT vs. J20 in **e**; and WT vs 3xTg in **f**) or one-way ANOVA with Tukey's post-hoc test (**e,f**).

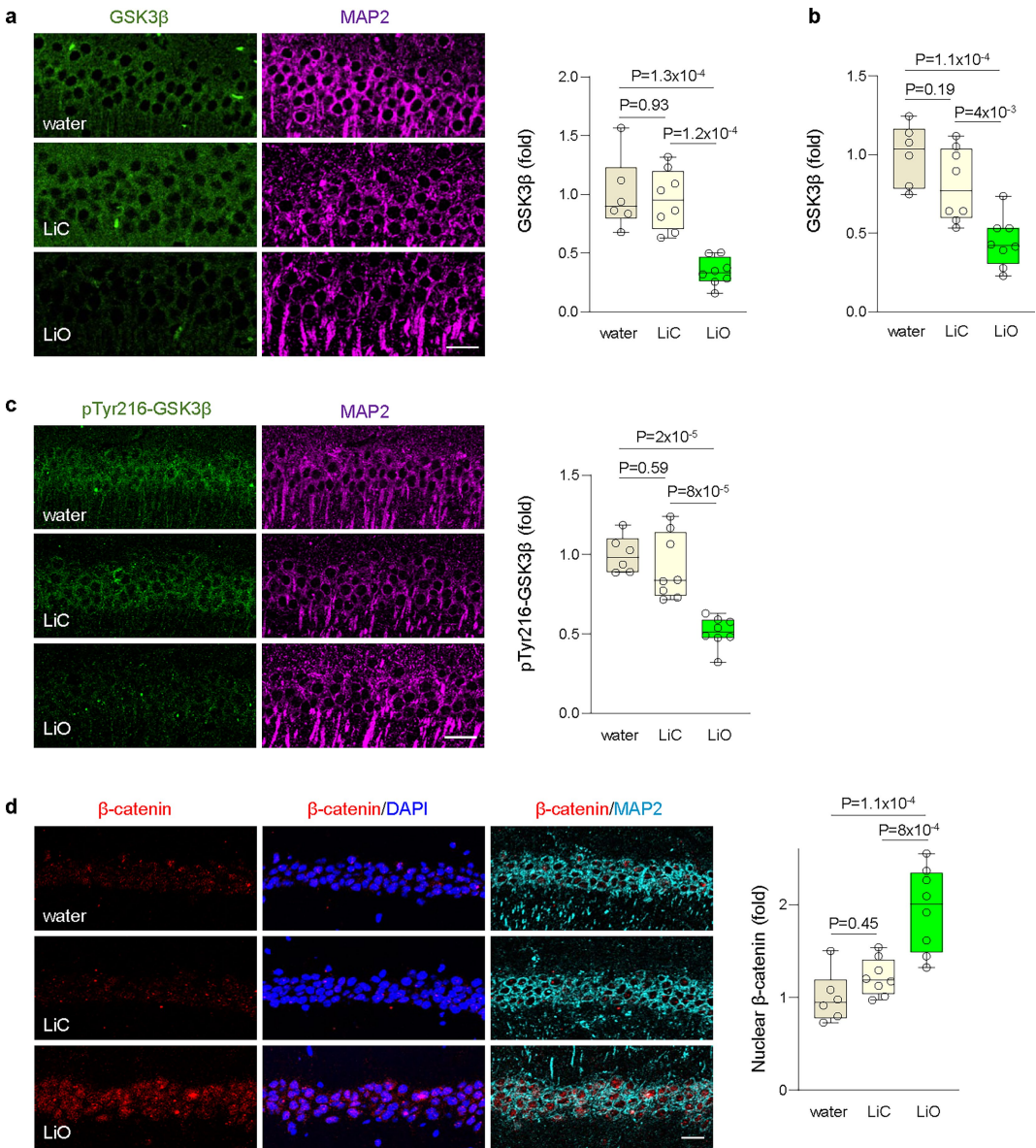
Article



Extended Data Fig. 8 | Suppression of AD patholog by lithium orotate.

a,b, Immunolabeling of A_β (**a**) and pSer202-tau (p-tau/CP13, **b**) and quantification of A_β plaque burden (**a**, right) and CP13⁺ cell density (**b**, right) in the hippocampus of 3xTg mice treated with the indicated concentrations of LiO, LiC, NaO or vehicle (water) from 5–12 months of age. **c**, Immunolabeling and quantification (right) of postsynaptic PSD-95 in hippocampus CA1 of 3xTg mice administered LiO or LiC (4.3 μEq/L), or vehicle from 9–18 months of age. **d,e**, Immunolabeling of myelin basic protein (MBP) (**d**) and oligodendrocytes (Aspatoacylase labeling) and quantifications of MBP expression (**d**, right) and

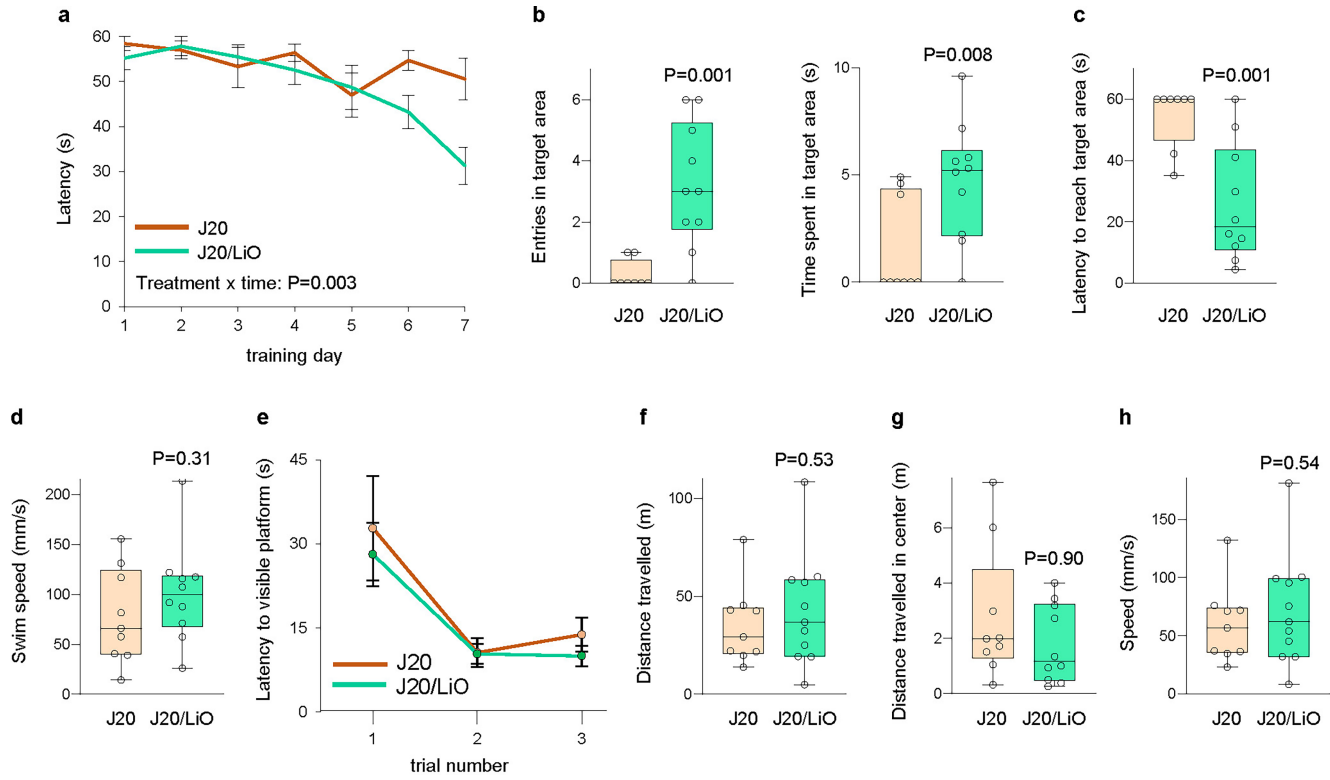
oligodendrocyte density (**e**, right) in the corpus callosum of 3xTg mice. **f,g**, Quantification of Iba1⁺ microglia (**f**) and GFAP⁺ astrocyte (**g**) densities in the hippocampus of 18-month-old 3xTg mice treated with LiO or LiC (4.3 μEq/L) or vehicle from 9–18 months of age. Box plots show individual values, median (line), box limits (25th-75th percentiles), and whiskers (min-max). **a-g**, Data was normalized to the vehicle group means and analyzed by one-way ANOVA with Tukey's post-hoc test. Scale bars, 25 μm. **a,b**, vehicle n = 17, LiO 4.3 n = 17, LiO 43 n = 8, LiO 430 n = 15, LiC 430 n = 10, NaO 4.3 n = 8, NaO 430 n = 6. **c-g**, water n = 4 (**c**), n = 6 (**d-f**), n = 7 (**g**); LiC n = 8, LiO n = 8.



Extended Data Fig. 9 | Lithium orotate suppresses GSK3 β activity.

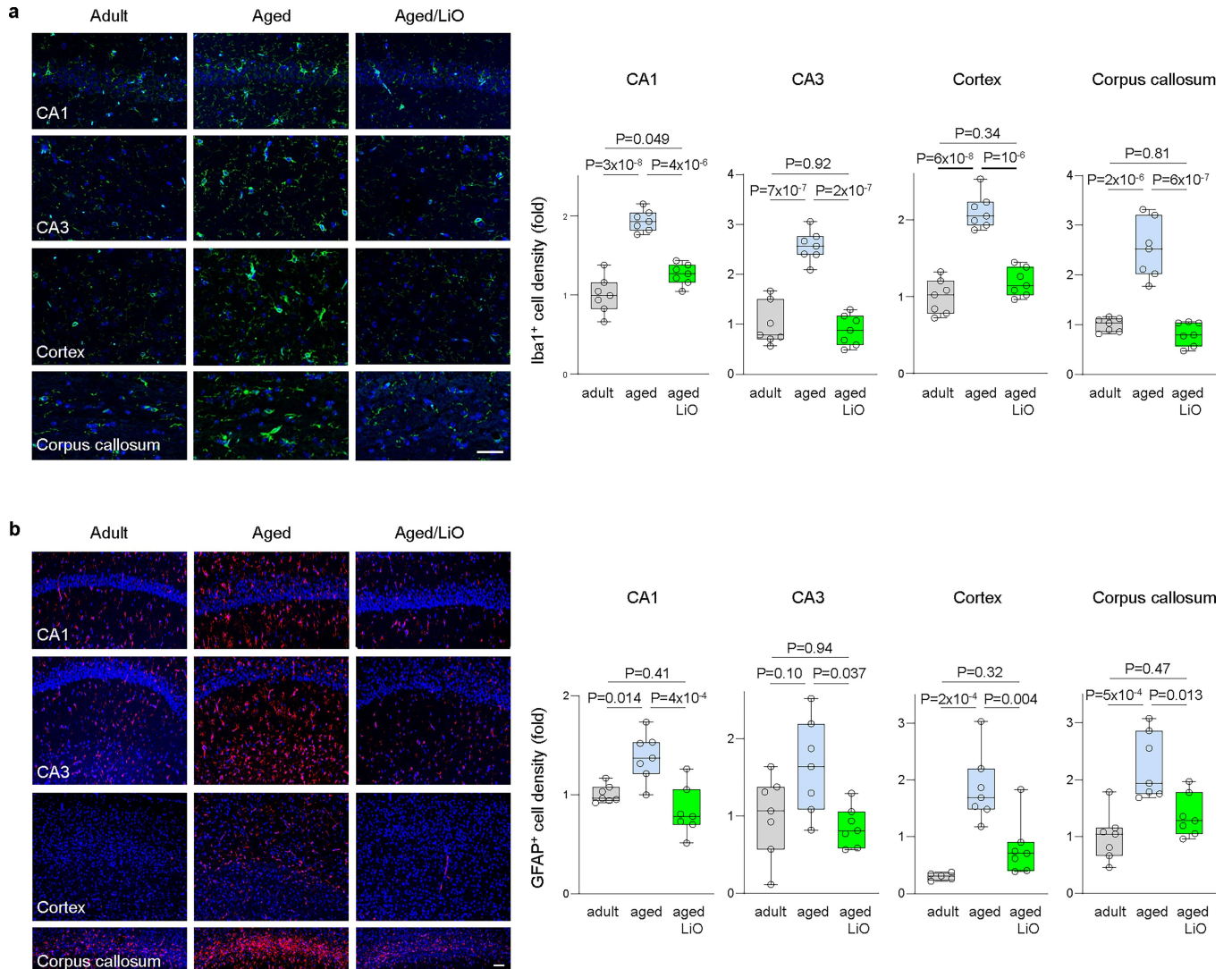
a-d, Treatment with LiO broadly reduces both total and activated GSK3 β . 3xTg mice were treated from 9–18 months of age with LiO, LiC (4.3 μ Eq/L), or vehicle (water). **a,c,d**, Left panels show representative immunolabeling of total GSK3 β (**a**), pTyr216-GSK3 β (**c**), and nuclear β -catenin (**d**) in hippocampal CA1 neurons double-labeled for MAP2. Nuclei were labeled with DAPI (**d**). **a,c,d**, Right panels

show quantification of total GSK3 β , pTyr216-GSK3 β and nuclear β -catenin in hippocampal CA1 neurons. **b**, Quantification of total GSK3 β in corpus callosum oligodendrocytes (double-labeled for GSK3 β and Aspartoacylase). **a-d**, Box plots show individual values, median (line), box limits (25th-75th percentiles), and whiskers (min-max). Data was analyzed by one-way ANOVA with Tukey's post-hoc test; P-values are shown. water n = 6, LiO n = 8, LiC n = 8. Scale bars, 50 μ m.



Extended Data Fig. 10 | Lithium orotate restores spatial memory in J20 mice with advanced amyloid pathology. **a**, Time course of spatial learning in the Morris water maze for J20 mice administered LiO (4.3 µEq/L) or vehicle (water) from 17–22 months of age. Shown are means ± S.E.M. **b,c**, Memory retrieval in the probe trial of the Morris water maze. Shown is the number of entries and time spent in the target area (**b**), and the latency to reach the target area (**c**). **d,e**, Swim speed and the latency to find a visible platform. **f-h**, LiO does not affect exploratory behavior in the open field test. Shown is distance

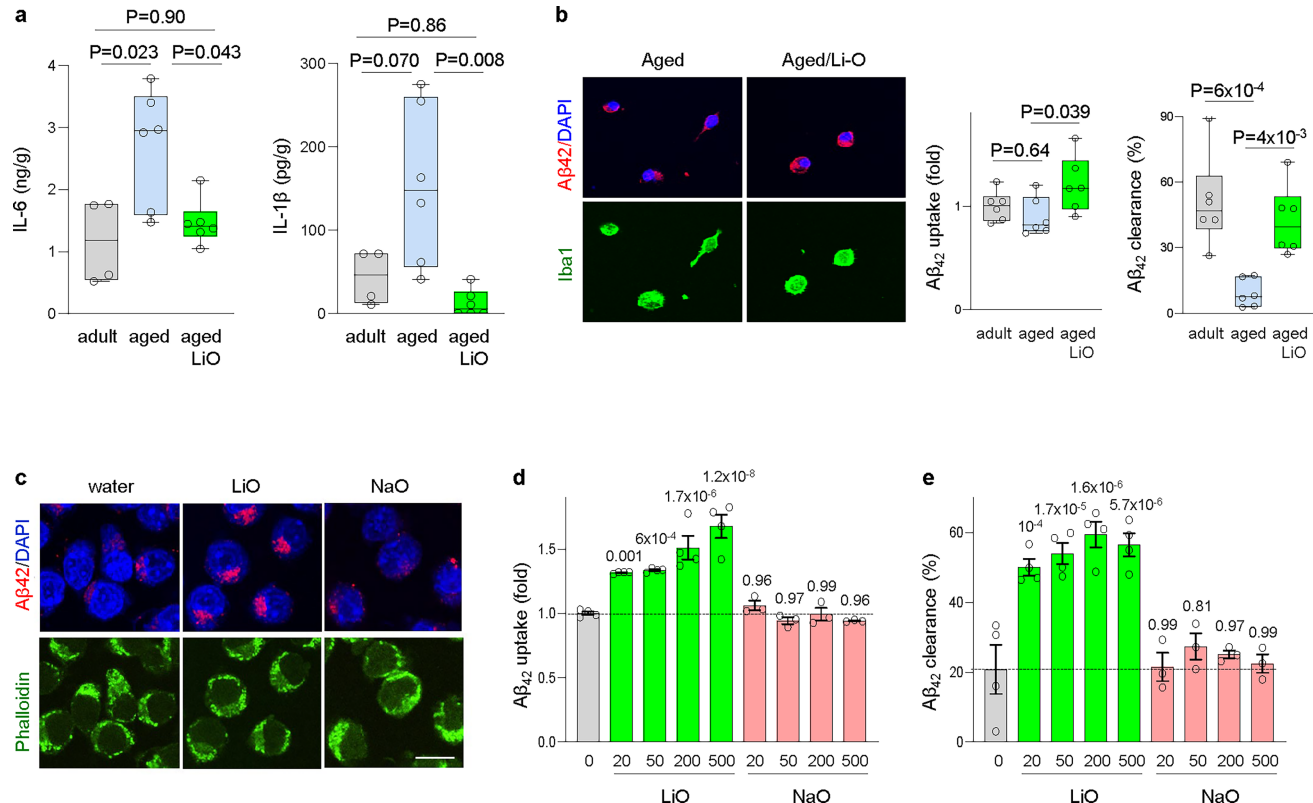
travelled, distance travelled in the center of the arena, and the speed in the open field. **b-h**, Box plots show individual values, median (line), box limits (25th-75th percentiles), and whiskers (min-max). **a**, Learning data were analyzed using mixed-effects models with repeated measures, followed by Šídák's post-hoc test. **b-h**, P-values by two-tailed unpaired Mann Whitney U test (**b**) or two-tailed unpaired t-tests (**c-h**). **e**, no significant differences were found. Vehicle n = 8 (**b**, left; **c**, n = 9 (**a,b** right, **d-h**); LiO n = 10 (**a-e,g**), n = 11 (**f,h**).



Extended Data Fig. 11 | Lithium orotate prevents age-related neuroinflammation. **a,b**, LiO prevents age-related neuroinflammatory changes in the hippocampal CA1 and CA3 regions, cortex, and corpus callosum of WT mice. **Top panels:** Microglia (**a**, Iba1 labeling) and astrocytes (**b**, GFAP labeling) were immunolabeled in 6-month-old WT mice (adult), 24-month-old WT mice (aged), and 24-month-old WT mice administered LiO (4.3 µEq/L) from

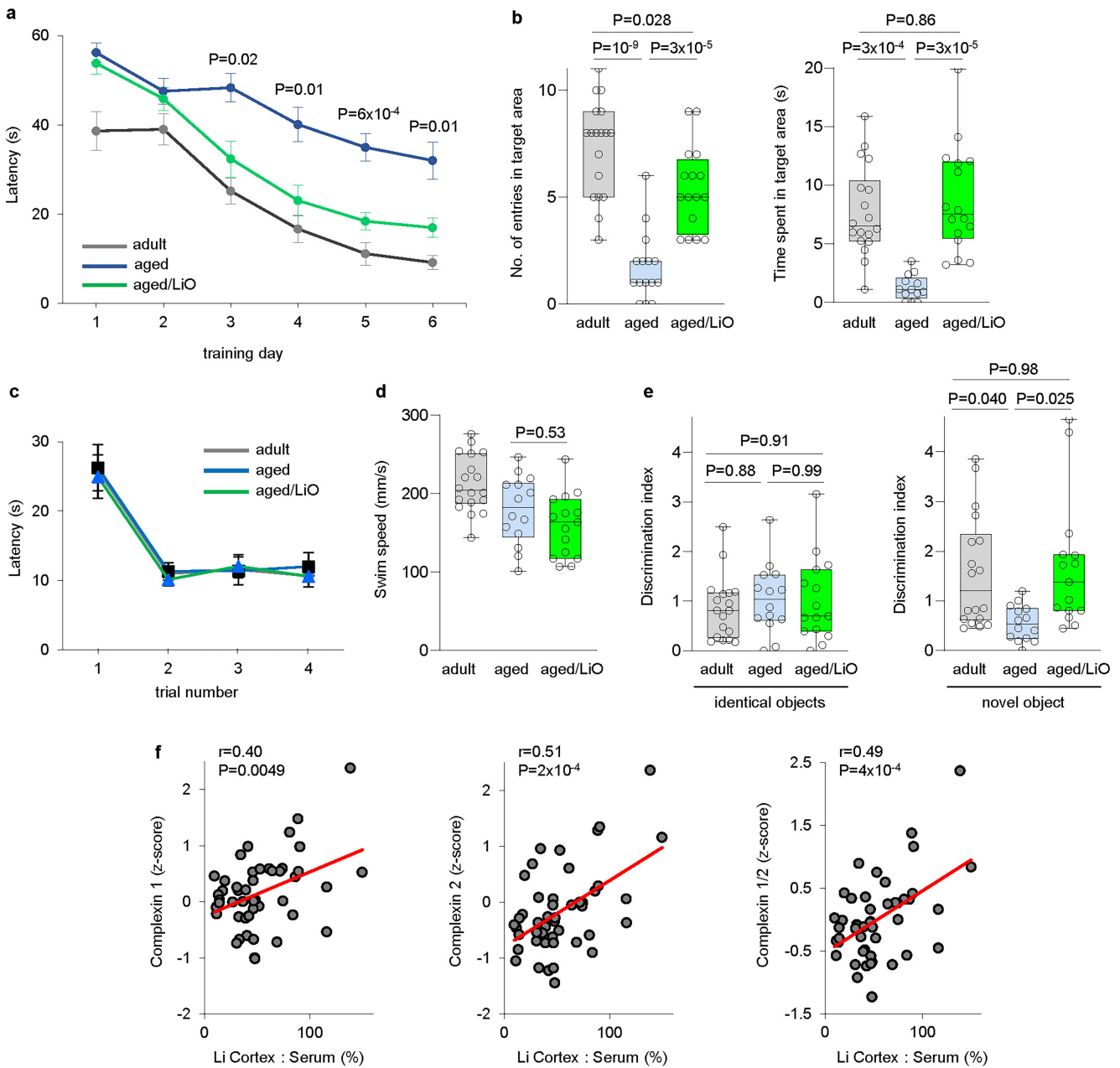
12–24 months of age (Aged/LiO). **Bottom panels:** Quantification of Iba1- (**a**) and GFAP-positive (**b**) cell densities. DAPI labeled cell nuclei. Box plots show individual values, median (line), box limits (25th-75th percentiles), and whiskers (min-max). The data was analyzed by two-way ANOVA with Tukey's post-hoc test and the P-values for comparisons are indicated. n = 7 mice/group, except in panel **b** (cortex: adult n = 5). Scale bars, 25 µm.

Article



Extended Data Fig. 12 | Lithium orotate promotes microglial clearance of A β . **a**, LiO reverses age-related elevation of the proinflammatory cytokines IL-6 and IL-1 β . Adult n = 4, Aged n = 6, Aged/LiO n = 6. **b**, LiO rescues the ability of aged microglia to clear A β . Left panel: Uptake of fluorophore-labeled human A β_{42} (red) by Iba1 $^+$ microglia (green). Right: Quantification of uptake and clearance. Microglia from 6-month-old WT controls (adult) were also analyzed. To assess A β_{42} uptake, microglia were incubated for 3 hr with A β_{42} -containing medium. After the 3 hr preincubation, the medium was replaced with A β_{42} -free medium and cells were incubated for an additional 3 hr to assess A β_{42} clearance. Microglia were purified from n = 6 mice per group. **c-e** LiO promotes microglial uptake and degradation of A β_{42} . BV2 cells were pre-treated with 20–500 μ M

LiO or NaO for 6 hr, then incubated for 3 hr with fluorophore-labeled human A β_{42} in the continued presence of the respective compound. **c**, Shown is A β_{42} (red) and phalloidin (green) labeling. **d,e** Quantification of A β_{42} uptake (**d**) and clearance (**e**). Water n = 4, LiO n = 4, NaO n = 3 biological replicates. The LiO and NaO concentrations (20–500) were in μ M. The data was normalized to the mean of adult controls (**b**, left) or water vehicle (**d**). **a,b**, Box plots show individual values, median (line), box limits (25th–75th percentiles), and whiskers (min–max). **d,e**, Shown are individual values, as well as means \pm S.E.M. Data was analyzed by one-way (**d,e**) or two-way (**a,b**) ANOVA with Tukey's (**a**), Šídák's (**b**) or Dunnett's (**d,e**) post-hoc tests and P-values are indicated. **d,e**, P-values are for comparisons to the water control. Scale bars, 15 μ m.



Extended Data Fig. 13 | Lithium and cognitive resilience during aging.

a-e LiO prevents age-related cognitive decline in WT mice. WT mice were treated with LiO (4.3 µEq/L) or vehicle from 12–24 months of age and then assessed behaviorally, together with 6-month-old WT mice (adult). **a**, Time course of spatial learning in the Morris water maze. **b**, Spatial memory was assessed in the probe trial of the Morris water maze. Shown are entries and time spent in the target area. **c-d**, Administration of LiO does not affect the latency to find a visible platform (**c**) or swim speed (**d**) in the Morris water maze. **e**, LiO restores the ability of aged WT mice to recognize a novel object. Shown is the discrimination index for identical objects (left) and for a novel object (right). **a,c**, Shown are means ± S.E.M. **b,d,e**, Box plots show individual values, median (line), box limits (25th-75th percentiles), and whiskers (min-max). **a-e**, Adult

n = 18; Aged n = 14 (**d,e**) n = 15 (**a-c**); Aged/LiO n = 15 (**d,e**), n = 16 (**a-c**). **a,c**, Data was analyzed using mixed-effects models with repeated measures, followed by Tukey's post-hoc test. **b,d,e**, Data was analyzed by two-way ANOVA with Tukey's post-hoc test. **a**, shown are adjusted P-values for comparisons between Aged/LiO vs. Aged. **c**, No significant differences were seen between the 3 groups. **f**, Linear regression curves between cortical Li cortex-to-serum ratios and expression of cortical Complexin1 (ROSMAP variable: *synap_3cort_complex1*), Complexin2 (ROSMAP variable: *synap_3cort_complex2*), as well as a measure of mean Complexin1/2 expression in 3 brain regions (mid-cortex, inferior temporal cortex, and hippocampus; (ROSMAP variable: *zcomplexin_3cort*) for n = 47 aged cases with no cognitive impairment (NCI). Pearson correlation coefficients (r) and P-values are indicated.

Corresponding author(s): Bruce A. Yankner

Last updated by author(s): Jun 18, 2025

Reporting Summary

Nature Portfolio wishes to improve the reproducibility of the work that we publish. This form provides structure for consistency and transparency in reporting. For further information on Nature Portfolio policies, see our [Editorial Policies](#) and the [Editorial Policy Checklist](#).

Statistics

For all statistical analyses, confirm that the following items are present in the figure legend, table legend, main text, or Methods section.

n/a Confirmed

- The exact sample size (n) for each experimental group/condition, given as a discrete number and unit of measurement
- A statement on whether measurements were taken from distinct samples or whether the same sample was measured repeatedly
- The statistical test(s) used AND whether they are one- or two-sided
Only common tests should be described solely by name; describe more complex techniques in the Methods section.
- A description of all covariates tested
- A description of any assumptions or corrections, such as tests of normality and adjustment for multiple comparisons
- A full description of the statistical parameters including central tendency (e.g. means) or other basic estimates (e.g. regression coefficient) AND variation (e.g. standard deviation) or associated estimates of uncertainty (e.g. confidence intervals)
- For null hypothesis testing, the test statistic (e.g. F , t , r) with confidence intervals, effect sizes, degrees of freedom and P value noted
Give P values as exact values whenever suitable.
- For Bayesian analysis, information on the choice of priors and Markov chain Monte Carlo settings
- For hierarchical and complex designs, identification of the appropriate level for tests and full reporting of outcomes
- Estimates of effect sizes (e.g. Cohen's d , Pearson's r), indicating how they were calculated

Our web collection on [statistics for biologists](#) contains articles on many of the points above.

Software and code

Policy information about [availability of computer code](#)

Data collection

For ICP-MS, the samples were injected into a PerkinElmer NexION 2000C ICP-MS instrument. The LA-ICP-MS spectrometer consisted of a laser ablation system (213 nm Nd:YAG, Cetac Technologies, Omaha, Nebraska, USA) connected to a Perkin Elmer NexION 2000C ICP-MS (Perkin Elmer, Norwalk, CT, USA).

To acquire immunofluorescence images, an Olympus FluoViewTM LV3000 confocal microscope and 10x, 20x or 40x objectives were used. For DAB-stained sections, pictures were acquired using a brightfield microscope coupled to a camera. Transmission electron microscopy images were acquired using either a JEOL 1200EX or a Tecnai G² Spirit BioTWIN transmission electron microscope.

Real time PCR data was collected using Bio Rad's CFX Connect Real-Time PCR detection system.

Behavioral data was collected by monitoring the mice in real time, using the TopScanLite software from CleverSys Inc., coupled to a camera. Behavioral data was collected automatically for each animal (TopScanLite), except the latency to reach the visible platform in the Morris water maze, which was recorded manually using a stopwatch.

For snRNA-seq, nuclei encapsulation and sequencing library preparation were performed at the Harvard Single Cell Core, according to the 10X Genomics manual. The size and quality of the prepared libraries were confirmed on Agilent high sensitivity TapeStation, and the library was independently quantified by qPCR. The prepared libraries were sequenced by Nova-Seq S4 at Harvard Biopolymers Facility.

For microglia RNA-seq, total microglial RNA was extracted from MACs-purified microglia and quantified using an Agilent Tapestation 4200 instrument, with a corresponding Agilent Tapestation High Sensitivity RNA assay. Agilent Bioanalyzer High Sensitivity DNA assay (was used to quantify cDNA concentration. Libraries were obtained using the Illumina NexteraXT kit. Purified libraries were run on an Agilent 4200

Tapestation instrument, with a corresponding Agilent D5000 ScreenTape assay to check the size and concentration of each library. Samples were loaded onto an Illumina NovaSeq 6000 instrument, with a single lane of an S4 flowcell to obtain Paired-End 100bp reads.

For Li-orotate RNA-seq, hippocampal RNA was purified using the Direct-zol RNA Mini Prep kit (Zymo Research), RNA integrity and concentration were assayed using an Agilent 2100 Bioanalyzer instrument, and libraries were prepared using Illumina TruSeq Stranded mRNA sample preparation kits from 500 ng of purified total RNA. dsDNA libraries were quantified using Qubit fluorometer, Agilent TapeStation 2200, and RT-qPCR using the Kapa Biosystems library quantification kit. Uniquely indexed libraries were pooled and sequenced on an Illumina NextSeq 500 with paired-end 75-bp reads by the Dana-Farber Cancer Institute Molecular Biology Core Facilities.

For mass spectrometry proteomic analysis, the fractions were processed at the Harvard Center for Mass Spectrometry; each fraction was submitted for a single LC-MS/MS experiment that was performed on Q Exactive HF-X High Resolution Orbitrap (Thermo Fisher, Waltham, MA) coupled with Ultimate 3000 nanoLC (Thermo Fischer, Waltham, MA).

The conductivity of Li salt solutions was measured using a ST300C conductivity meter (OHAUS, Catalog No. 83033964) equipped with a STCON7 electrode (OHAUS, Catalog No. 30080693) calibrated with potassium chloride conductivity standards. For each lithium salt, three independent solution replicates ($n = 3$) were prepared. Conductivity values are reported in $\mu\text{S}/\text{cm}$ at 25°C.

Data analysis

ICP-MS signal data was analyzed using GeoPro 2010 Software (Cetac Technologies) and LA-ICP-MS data was analyzed using the Iolite Software 2018 (Iolite).

$\text{A}\beta$ plaque burden and p-tau pathology were analyzed using Fiji/ImageJ 2.9.0. Fluorescent image analysis was also performed using MetaMorph NX 2.5 (Meta Series, Molecular Devices).

Quantification of myelin sheath thickness, axon diameter, and g-ratios was performed using Metamorph software (Meta Series). A total of 1,376 axons (CTRL group) and 1,396 axons (Li-deficient group) were analyzed from 8 randomly selected fields per animal (4800x magnification) spanning the corpus callosum.

For Golgi labeling, dendritic spine density was quantified using the Fiji software 2.9.0.

For snRNA-seq, the demultiplexed raw sequencing reads were aligned to the mouse genome (mm10 from 10X genomics) using Cell Ranger (6.1.2), with --include-introns option, to account for nuclear pre-mRNAs. The generated counts table was loaded to Seurat (v4) to generate Seurat objects. Cells with more than 10 percent of reads being attributed to mitochondrial transcripts were filtered out. Cells that expressed less than 200 features (low-quality cells) or higher than 8,000 features (apparent doublets) were also filtered out. These thresholds are determined by visual inspection of the distribution of features among cells (Seurat, VInPlot) and generally consistent with other reports. The cells that passed quality controls were log normalized using NormalizeData function from Seurat with a scale factor of 10,000. Variable features were identified using FindVariableFeatures function from Seurat with vst selection method and 2000 features. Data was scaled using ScaleData, and PCA was performed using RunPCA with the identified variable features using Seurat. Nearest neighbors were found using FindNeighbors using dimension 1:30, which was determined by ElbowPlot following Seurat's manual. The number of clusters was determined by FindClusters function using Seurat v4. UMAP and TSNE were performed using RunUMAP or RunTSNE using Seurat with dimensions 1:30 and do.fast=TRUE parameter. Potential doublets were removed using DoubletFinder (v3) following the default parameters. After filtration, cluster-specific markers were determined by FindAllMarkers function (Seurat v4), with parameters only.pos = F, min.pct = 0.25 and max.cell.per.ident = 500. Cell types were identified by cross-referencing the transcriptome of each individual cell to the Mouse Cell Atlas and independently validated by confirming the expression of established cell type-specific markers, on a cluster-to-cluster basis. Cell type-specific abundance and differential gene expression analyses were performed on the major cell types (excitatory neurons, inhibitory neurons, granule cells, microglia, astrocytes, oligodendrocytes, oligodendrocyte precursor cells and endothelial cells). Clusters of the same cell types were combined to increase the statistical power, and clusters with mixed cell types (<80% homogenous) were removed for cell type-specific analyses. Relative abundance of each cell type was computed by dividing the number of cells of the particular cell type by the total number of cells. Two-tailed unpaired Student's t-tests were performed to determine if there were significant differences in the relative abundance of each cell type between the control and lithium deficient conditions. Differentially expressed genes (DEGs) were computed by the MAST test in Seurat. Genes expressed in less than 1% of the cells in each cell type were filtered out.

For microglia RNA-seq, raw RNA-sequencing data in FASTQ format was subjected to quality assessment using FastQC (version 0.11.9) and sequencing reads are aligned to mouse genome (mm10) using STAR aligner with the following options: --outFilterMismatchNmax 999 --outFilterMismatchNoverLmax 0.04 --alignSJDBoverhangMin 1 --alignSjoverhangMin 8 --outFilterMultimapNmax 20 --outFilterType BySJout --alignIntronMin 20 --alignIntronMax 1000000 --alignMatesGapMax 1000000. Microglia RNAseq yielded an average of 148 million uniquely mapped reads; gene expression levels were quantified using htseq-count. Differential gene expression analysis was conducted using DESeq2 to identify DEGs between Li-def and control microglia, with an adjusted p-value cutoff of 0.05. Upregulated and downregulated DEGs from Li-deficient WT and 3xTg microglia were further analyzed for overlapping DEGs and the overlapping DEGs were subjected to gene ontology enrichment analysis using Metascape v3.5.20240101.

For Lithium orotate RNA-seq, quality control of sequencing reads was performed with FastQC version 0.11.5. Reads were aligned to the Mouse GRCm38 genome with GENCODE M21 gene models using STAR version 2.7.0f with options --outSAMunmapped Within --alignSJDBoverhangMin 1 --alignSjoverhangMin 8 --outFilterMultimapNmax 20 --outFilterType BySJout --alignIntronMin 20 --alignIntronMax 5000000 --alignMatesGapMax 5000000 --twoPassMode Basic. The expression of genes was quantified as gene counts using STAR at the same time as alignment with option --quantMode GeneCounts. Gene counts were input to edgeR. Genes were deemed expressed if at least $n=9$ samples (where n is the group size) had >1 CPM. Genes not satisfying these criteria were removed, keeping the original library sizes. This filtering retained $n=14,862$ expressed genes out of 55,536 annotated genes for subsequent analyses. Counts were then normalized using the TMM method in edgeR. To adjust gene expression for covariates we fit the linear regression model for each gene and cohort separately using lm() in R: gene expression ~ group + covariates where gene expression is log(CPM), and using the group and covariates: factor, two levels: Lithium Orotate and Water (reference level), covariates (sequencing batch (factor, two levels) and 1 RUVr covariate (continuous). The final normalized and adjusted gene expression values were derived from adding the regression residuals to the estimated effect of the group level to preserve the effect of the group on expression. These normalized and adjusted gene expression values were used to perform gene–gene regression analysis and gene–gene group regression analysis, and to visualize gene expression. To adjust for technical variation, we used the RUV with residuals (RUVr) method implemented in the RUVSeq version 1.18.0 Bioconductor package. We performed a first pass edgeR analysis as described in section “Differential expression analysis” up to and including the glmFit() step with the covariates listed above

excluding the RUVr covariates. Then we used residuals() with argument type='deviance' to obtain a matrix of deviance residuals. The specified number of unwanted factors (RUVr covariates) used in final analyses were then estimated by the RUVr function using log(CPM) expression values and the residuals. The number of unwanted factors was selected based on separation of groups in principal components plots using normalized and adjusted gene expression values and checking that histograms of differential expression P values showed a uniform or anti-conservative pattern. Differential expression analysis between groups with covariate adjustment using the covariates listed above was performed for expressed genes using edgeR (estimateDisp, glmFit, and glmLRT with default arguments) in R. Genes were considered differentially expressed if FDR < 0.05. Gene ontology enrichment analysis was performed separately for upregulated genes and downregulated genes using Metascape v3.5.20240101.

To conduct the GWAS-DEG enrichment analysis, we converted the mouse gene symbols to human orthologs, using a two-step process. First, the "alias2SymbolTable" function within the "Limma" R package 3.58.1 was utilized to map any gene aliases to their corresponding main symbols. Subsequently, the resulting gene symbols were converted to human orthologs using the MGI ortholog table. If there were multiple mapping candidates, all possible conversions were applied. For example, if a mouse gene has multiple human orthologs, records with all relevant human gene symbols were generated. This standardized gene nomenclature facilitated cross-species comparisons in subsequent analyses. To conduct the GWAS-DEG enrichment analysis microglia isolated from Li-deficient mice, we utilized MAGMA v1.10. Gene-set analysis was conducted using the default MAGMA settings, with multiple testing correction applied to account for the number of gene sets tested. Enrichment results were considered significant at a false discovery rate (FDR) of 0.05.

To examine the overlap of human DEGs and mouse DEGs derived from our transcriptomic analyses, we first converted mouse gene symbols to human orthologs, as described above. We matched the cell types analyzed in our mouse studies with those analyzed in humans. To assess the statistical significance of the overlap between the two DEG sets, we conducted a Fisher's exact test. To control for multiple comparisons arising from the analysis of different cell types and DEG directions (upregulated and downregulated), we adjusted the p-values using the Benjamini-Hochberg procedure. Two sets of adjusted p-values were calculated: One set for the overlap of genes upregulated in both datasets (indicated in red), and another for the overlap of genes downregulated in both datasets (indicated in blue).

To analyze the proteomics data, raw data was submitted for analysis in Proteome Discoverer 3.0 software (Thermo Scientific). The MS/MS Data was searched against the UniProt reviewed *Mus musculus* (Mouse) database along with known contaminants such as human keratins and common lab contaminants. Sequest HT searches were performed using the following guidelines: a 10 ppm MS tolerance and 0.02 Da MS/MS tolerance; Trypsin digestion with up to two missed cleavages; carbamidomethylation (+57.021 Da) on cysteine, TMT 6-plex tags on peptide N-termini and lysine residue (+229.163 Da) were set as static modification; oxidation (+15.995 Da) of methionine set as variable modification; minimum required peptide length set to ≥ 6 amino acids. At least one unique peptide per protein group was required for identifying proteins. Of 13,404 proteins identified, only n=3,392 proteins were identified with high confidence (MS2 spectra assignment FDR<0.01 on both protein and peptide level by applying the target-decoy database search by Percolator) and were included in the statistical analysis, as per standard procedures at the Harvard Center for Mass Spectrometry. The sample labels were control (samples 1,3,5,7) and Li-deficient (samples 2,4,6,8) and were all 3xTg homozygous females, age 15 months (duration of the treatment: from 6 to 15 months). An ANOVA followed by Tukey's post hoc test was used to assess differences in protein abundance between Li-deficient and control samples. P-values were adjusted for multiple comparisons using the Benjamini-Hochberg method to control the false discovery rate. Proteins with an adjusted P-value < 0.05 were considered differentially abundant. T

Statistical analysis was performed using the GraphPad software v 10.3.0 (507). Statistical tests used are noted in the figure legends or in the relevant Methods section. Throughout the paper, all tests are two sided and unpaired unless stated otherwise. A significance level of 0.05 was used to reject the null hypothesis unless stated otherwise. The sample size, the age and sex of experimental animals, as well as the summary of each statistical test (including degrees of freedom, confidence intervals and P-values) can be found in the Source Data file.

For manuscripts utilizing custom algorithms or software that are central to the research but not yet described in published literature, software must be made available to editors and reviewers. We strongly encourage code deposition in a community repository (e.g. GitHub). See the Nature Portfolio [guidelines for submitting code & software](#) for further information.

Data

Policy information about [availability of data](#)

All manuscripts must include a [data availability statement](#). This statement should provide the following information, where applicable:

- Accession codes, unique identifiers, or web links for publicly available datasets
- A description of any restrictions on data availability
- For clinical datasets or third party data, please ensure that the statement adheres to our [policy](#)

The snRNA-seq, microglia RNA-seq and LiO RNA-seq data have been deposited in the Gene Expression Omnibus repository (GSE272344, GSE275326 and GSE295788).

The mass spectrometry proteomics data have been deposited to the ProteomeXchange Consortium via the PRIDE partner repository with the dataset identifier PXD063039. The proteins identified with high confidence and included in the statistical analysis are listed in Supplementary Table 7. All other proteins identified with lower confidence can be accessed from the files deposited at the ProteomeXchange Consortium via the PRIDE partner repository with the dataset identifier PXD063039. MS/MS proteomic data were searched against the UniProt *Mus musculus* protein database (FASTA format, including isoforms), downloaded on July 17, 2022.

For GWAS-DEG enrichment analysis using MAGMA, summary statistics for Alzheimer's disease (Accession ID: MONDO_0004975) were obtained from the GWAS Catalog (https://www.ebi.ac.uk/gwas/efotraits/MONDO_0004975).

Clinico-pathological data on postmortem human samples from ROSMPAP can be requested at <https://www.radc.rush.edu>.

Research involving human participants, their data, or biological material

Policy information about studies with [human participants or human data](#). See also policy information about [sex, gender \(identity/presentation\), and sexual orientation](#) and [race, ethnicity and racism](#).

Reporting on sex and gender

Both male and female participants were included in the human studies. In both sexes, individuals with MCI and AD showed reduced cortical-to-serum Li ratios and lower total cortical Li levels. Mouse experiments also included both sexes, and results were consistent between males and females.

Reporting on race, ethnicity, or other socially relevant groupings

Donor sex was self-reported and provided by Rush Medical Center, which conducted the ROSMAP longitudinal study, as well as by other tissue sources including Massachusetts General Hospital, Duke University, and Washington University.

Population characteristics

The cohort analyzed in this study consisted of 40.2% males and 59.8% females. Among the subgroups, NCI cases comprised 40.8% males and 59.2% females; MCI cases had 42% males and 58% females; and AD cases included 36.4% males and 63.6% females. Both males and females in the MCI and AD groups exhibited reduced Li cortex-to-serum ratio and lower total cortical Li levels.

For ROSMAP: To assess cognitive function, 21 cognitive function tests were used, 19 were in common and 11 used to inform on clinical diagnoses, as previously described (references 60,61). Brain tissue obtained from Massachusetts General Hospital, Duke University, and Washington University had a confirmed pathological diagnosis of AD or NCI.

Recruitment

Our study did not involve any recruitment or interaction with the donors. We only analyzed postmortem tissue, which was provided by Rush University Medical Center, as well as the brain banks at Massachusetts General Hospital, Duke University and Washington University. Samples were randomly selected by the source institutions based on tissue availability and alignment with the requested diagnostic categories (NCI, MCI, AD). Within each diagnostic group, samples were matched for age and sex to ensure group comparability.

Ethics oversight

Postmortem human brain and serum samples were obtained in accordance with institutional guidelines and with approval from the Harvard Medical School Institutional Review Board. All procedures complied with relevant ethical regulations. All postmortem human brain and serum samples were fully deidentified prior to receipt, and no identifiable private donor information was accessible to the researchers. As such, informed consent was not applicable.

Informed consent, an Anatomic Gift Act, and a repository consent were obtained and the studies were approved by an Institutional Review Board (IRB) of Rush University Medical Center. The Religious Orders Study and Rush Memory and Aging Project (ROSMAP) were approved by an IRB of Rush University Medical Center.

Note that full information on the approval of the study protocol must also be provided in the manuscript.

Field-specific reporting

Please select the one below that is the best fit for your research. If you are not sure, read the appropriate sections before making your selection.

Life sciences Behavioural & social sciences Ecological, evolutionary & environmental sciences

For a reference copy of the document with all sections, see nature.com/documents/nr-reporting-summary-flat.pdf

Life sciences study design

All studies must disclose on these points even when the disclosure is negative.

Sample size

No statistical methods were used to pre-determine sample size. Sample sizes were chosen based on prior literature that used similar approaches (see Martorell et al. *Cell* 177(2):256-271 (2019); Zullo et al. *Nature* 574, 359-364 (2019); Iaccarino et al. *Nature* 540(7632):230-235 (2016); Sevigny et al. *Nature* 537(7618):50-6 (2016); Oddo et al. *Neuron* 39(3):409-21 (2003)). The sample size was determined to be adequate based on the magnitude and reproducibility of observed differences between the different groups.

Data exclusions

Statistical outliers were identified using the ROUT method ($Q=1\%$, corresponding to $FDR<1\%$) in GraphPad Prism and excluded from the statistical analysis where appropriate. No data were excluded from the study.

Replication

The ICP-MS findings in postmortem human were replicated as follows. First, reduced lithium content in the cortex of AD patients was observed using 2 independent methods – after measurement of total lithium levels in frozen cortical material of cases from both ROSMAP (Fig. 1d) and other sources (Fig. 1e), as well as after fractionation and removal of amyloid plaques (Fig. 1g). Second, decreased Li levels in the AD vs. NCI frontal cortex ($P=2\times 10^{-3}$) were also independently confirmed when $n=60$ NCI and AD cases were processed and analyzed by ICP-MS in a different laboratory (Spectroscopy Core Facility at the University of Nebraska, Lincoln). Third, decreased Li levels in the AD vs. NCI frontal cortex ($P=3\times 10^{-3}$) were also confirmed when $n=48$ NCI and AD cases were processed using an alternative protocol. Frozen samples were thawed and dried to a constant weight by incubating in a dry oven at 60°C for 48 hours. The dried tissue was then digested in 1 mL of 67% nitric acid using a heating block at 95°C for 3 hours. After digestion, 0.3 mL of 30% hydrogen peroxide was added, and the mixture was heated for an additional 3 hours. Finally, the samples were diluted and analyzed using ICP-MS.

In agreement with previous findings, the Li levels we measured in the frontal cortex (FC) of aging NCI cases (ROSMAP cases: mean 2.36 ± 1.23 ng/g, range 0.52-6 ng/g; and non-ROSMAP cases: mean 3.5 ± 2.27 ng/g, range 0.89-9.94 ng/g; Figure 1d,e) were similar to those measured in

a previous study [Ramos, P. et al. J Trace Elem Med Biol 38, 174-182 (2016)] which found that Li levels were 4.1 ± 1.7 ng/g in the frontal cortex of aged non-diseased cases (age 71 ± 12 years). Similarly, the Li levels we measured in the cerebellum (ROSMAP cases: mean 2.9 ± 1.69 ng/g, range $0.58\text{--}8.4$ ng/g; Extended Data Fig. 1b) were similar to those measured in the previous study by Ramos et al. (2.9 ± 1.3 ng/g). Finally, consistent with previous studies, we also observed significantly elevated levels of sodium and zinc, along with reduced copper levels, in the AD frontal cortex (Figure 1a,b and Supplementary Table 1). [References: For sodium: Graham, S. F. et al. J Alzheimers Dis 44, 851-857 (2015). For zinc: Religa, D. et al. Elevated cortical zinc in Alzheimer disease. Neurology 67, 69-75 (2006). For copper: Squitti, R. et al. Biomolecules 11 (2021). <https://doi.org/10.3390/biom11070960>].

The effects of lithium deficiency on amyloid pathology were replicated in three mouse models: 3xTg, J20, and WT mice. All models exhibited elevated A β 42, and a marked acceleration of amyloid deposition observed in AD models (3xTg and J20). In 3xTg mice, accelerated amyloid pathology was evident at both short-term (5 weeks) and long-term (9 months) durations of a lithium-deficient diet. Similarly, in J20 mice, accelerated amyloid pathology was observed after both 3 and 9 months of lithium deficiency. Additionally, in WT mice, we noted increased A β x-42 production at two different time points (20 and 26 months of age) in the hippocampus and cortex.

The effects of Li deficiency on tau pathology were observed after both short (5 weeks) and longer (9 months) treatment durations in 3xTg mice, using two markers (pSer202 tau, CP13; as well as pSer396/Ser404 tau, PHF1) of tau phosphorylation. Moreover, Thioflavin S labeling allowed the detection of tangle-like profiles in Li-deficient 3xTg hippocampus.

The effects of Li deficiency on synapses were substantiated as follows: 1) by snRNA-seq analysis; 2) using labeling of synaptic markers (PSD-95 and Synaptophysin); 3) by unbiased proteomic analysis; and 4) using Golgi labeling, which showed a significant loss of dendritic spines in both WT and 3xTg Li-deficient mice.

Myelin and white matter disruption by lithium deficiency was observed using Fluoromyelin labeling, labeling for Myelin Basic Protein (MBP) and labeling of both mature oligodendrocytes (using Aspartoacylase as a marker) and oligodendrocyte precursor cells (using PDGFR α as a marker). In addition, transmission electron microscopy confirmed the myelin disruption in Li deficient mice at the ultrastructural level.

The effects of Li deficiency on microglia were observed in WT, 3xTg and J20 mice. In WT and 3xTg mice, Li deficiency altered the microglial transcriptome. Immunolabeling showed more reactive microglia in both 3xTg and J20 Li-deficient mice. Moreover, Li-deficient microglia secreted more pro-inflammatory cytokines, and had an impaired ability to clear amyloid beta.

The effects of Li deficiency on memory were replicated in 2 mouse lines: 3xTg and WT. Li deficiency accelerated memory loss in both lines.

The potentiating effects of lithium deficiency on GSK3 β were demonstrated through network modeling (Ingenuity Pathway Analysis), proteomics, increased GSK3 β levels in the Li-deficient 3xTg hippocampus, and immunolabeling for total and active GSK3 β (pTyr216). Enhanced GSK3 β activity under lithium-deficient conditions was further supported by both in vivo and in vitro experiments using GSK3 β inhibitors, which reversed the effects of lithium deficiency on A β deposition, tau phosphorylation, microglial activation, cytokine secretion, amyloid clearance, and myelin integrity.

The plaque-evasive abilities of Li orotate (LiO) were demonstrated in both aged J20 and 3xTg mice, at advanced stages of amyloid pathology. Moreover, Li binds human A β 1-42 fibrils and oligomers in vitro, over a range of concentrations. LiO binds less avidly to amyloid beta fibrils and oligomers compared to the clinical standard lithium carbonate (LiC), further suggesting that it may evade amyloid plaques in vivo.

The therapeutic effects of lithium orotate (LiO) were demonstrated in both 3xTg and J20 mouse models of Alzheimer's disease. In 3xTg mice, LiO showed both preventive and restorative effects on amyloid and tau pathology. Furthermore, LiO outperformed lithium carbonate (LiC), as evidenced by reduced amyloid and phosphorylated tau accumulation, improved synaptic integrity, attenuated microgliosis and astrogliosis, modulation of GSK3 β and β -catenin signaling, and improved performance in the Morris water maze test.

The beneficial effects of LiO treatment during aging in wild-type (WT) mice were demonstrated by improved performance in memory tests, preservation of dendritic spines, and reduced neuroinflammation. These findings align with the accelerated cognitive decline observed in Li-deficient WT mice, collectively supporting a physiological role for lithium in maintaining brain function during normal aging.

Randomization

For all mouse studies, animals were randomly assigned to experimental groups.

Blinding

For ICP-MS analysis of human samples, all measurements were performed under double-blind conditions. A team member not involved in the study re-labeled the samples and maintained the key linking original and blinded identifiers. Unblinding was conducted after data acquisition, in the presence of both the study investigators and the independent team member. For all other analyses involving human tissue, investigators were blinded to sample identity during both data collection and analysis. In mouse studies, genotypes and treatment conditions remained blinded to investigators throughout data collection and analysis.

Reporting for specific materials, systems and methods

We require information from authors about some types of materials, experimental systems and methods used in many studies. Here, indicate whether each material, system or method listed is relevant to your study. If you are not sure if a list item applies to your research, read the appropriate section before selecting a response.

Materials & experimental systems

n/a	Involved in the study
<input type="checkbox"/>	<input checked="" type="checkbox"/> Antibodies
<input type="checkbox"/>	<input checked="" type="checkbox"/> Eukaryotic cell lines
<input checked="" type="checkbox"/>	<input type="checkbox"/> Palaeontology and archaeology
<input type="checkbox"/>	<input checked="" type="checkbox"/> Animals and other organisms
<input checked="" type="checkbox"/>	<input type="checkbox"/> Clinical data
<input checked="" type="checkbox"/>	<input type="checkbox"/> Dual use research of concern
<input checked="" type="checkbox"/>	<input type="checkbox"/> Plants

Methods

n/a	Involved in the study
<input checked="" type="checkbox"/>	<input type="checkbox"/> ChIP-seq
<input checked="" type="checkbox"/>	<input type="checkbox"/> Flow cytometry
<input checked="" type="checkbox"/>	<input type="checkbox"/> MRI-based neuroimaging

Antibodies

Antibodies used

To detect different tau species, we used two antibodies: (1) a mouse monoclonal antibody that recognizes phosphorylated Ser 202 tau (CP13 clone; generous gift from Peter Davies, Albert Einstein College of Medicine, NY; dilution 1:150), and (2) a mouse monoclonal antibody raised against phosphorylated Ser 396/Ser404 tau (PHF1 clone; from Peter Davies, dilution 1:200). To detect transgenically expressed human A β in mouse models, we used a rabbit monoclonal anti-A β antibody (clone D54D2; Cell Signaling, catalog No. 8243, dilution 1:250).

The following primary antibodies were also used: anti-Aspartoacylase [N1C3-2] (GeneTex, GTX113389; rabbit polyclonal, dilution 1:200), anti-Aspartoacylase (clone D-11; Santa Cruz Biotechnology, sc-377308, dilution 1:50), anti- β -catenin (clone E247; Abcam, ab32572; rabbit recombinant monoclonal, dilution 1:250), anti- β -catenin (clone 188A1; PTGlab, 66379-1-Ig, mouse monoclonal, dilution 1:200), anti-CD68 (clone KP1; Abcam, ab955; mouse monoclonal, dilution 1:200), anti-GFAP (Sigma Aldrich, G9269; rabbit polyclonal, dilution 1:200), anti-GSK3 β (clone 3D10; Novus Bio, NBP1-47470SS; mouse monoclonal, dilution 1:200), anti-pTyr216-GSK3 β (Millipore Sigma, SAB4300237; rabbit polyclonal, dilution 1:100), anti-pSer9-GSK3 β (Abcam, ab131097; rabbit polyclonal, dilution 1:100), anti-Iba1 (clone EPR16588; Abcam ab178846; rabbit recombinant monoclonal, dilution 1:2,000), anti-PSD-95 (clone K28/43; Biolegend, 810401; mouse monoclonal, dilution 1:250), anti-Synaptophysin (clone SY38; Millipore Sigma, mouse monoclonal, MAB5258-I; dilution 1:200), anti-Neurofilament (pan axonal marker; clone SMI-312; Biolegend, 837904; mouse monoclonal, dilution 1:200), anti-GPNMB (clone 2B10B8; PTGlab, 66926-1-Ig; mouse monoclonal, dilution 1:200), anti-LPL (Novus Bio, AF7197-SP; goat polyclonal, dilution 1:200), anti-MAP2 (Phosphosolutions, 1099-MAP2; goat polyclonal, dilution 1:500), anti-Myelin Basic Protein (MBP) (clone D8X4Q; Cell Signaling, 78896; rabbit monoclonal, dilution 1:200) and anti-PDGFR α (R&D Systems, AF1062; goat polyclonal, dilution 1:200).

Secondary antibodies were used at a 1:300 dilution: donkey anti-Goat Alexa 594 (Invitrogen, A-11058), donkey anti-Rabbit IgG (H+L) Highly Cross-Adsorbed antibody, Alexa 488 (ThermoFisher Scientific, A21206), donkey anti-Mouse IgG (H+L) Highly Cross-Adsorbed antibody, Alexa 594 (ThermoFisher Scientific, A21203), donkey anti-Mouse Alexa 647 (Invitrogen, A-31571), donkey anti-Rabbit Alexa 647 (Invitrogen, A-31573), donkey anti-Goat Alexa 488 (Invitrogen, A-11055).

Validation

The tau antibodies obtained from Peter Davies, raised against pSer202 tau (CP13 clone) and pSer396/Ser404 tau (PHF1), have been extensively validated and cited in the field. In the lab, we have confirmed that both CP13 and PHF1 recognize tau species at the expected molecular weight in western blotting.

The anti-A β antibody (clone D54D2; Cell Signaling, catalog No. 8243) is a recombinant rabbit monoclonal antibody that recognizes human A β and has been validated for use in WB, IP, IF, and IHC-P. It has been cited 167 times.

The anti-Aspartoacylase antibody [N1C3-2], (GeneTex, GTX113389), rabbit polyclonal, has been validated for use in immunofluorescence, as well as WB, IHC-P, and IHC-Fr and has been cited 19 times.

The anti-Aspartoacylase antibody (clone D-11; Santa Cruz Biotechnology, sc-377308) is a mouse monoclonal antibody that has been validated for use in WB, IP, IF, IHC-P and ELISA. It has been cited 8 times.

The anti- β -catenin antibody (clone E247; Abcam, ab32572), rabbit recombinant monoclonal antibody, is a ChIP Grade antibody that has been validated for use in ChIP, ICC/IF, IHC-P, IP and Western blot. Specificity was confirmed in a knockout line by abcam. The antibody has been cited 1,408 times.

The anti- β -catenin antibody (clone 1B8A1; PTGlab, 66379-1-Ig), mouse monoclonal antibody, has been validated for use in WB, IHC, IF/ICC, IF-P, flow cytometry, IP, and ELISA. The antibody is knockout-validated and has been cited 108 times.

The anti-CD68 (clone KP1; Abcam, ab955), mouse monoclonal antibody, has been cited 620 times and has been validated for use in IHC-P, ICC/IF, WB by Abcam.

The anti-GFAP (Sigma Aldrich, G9269), rabbit polyclonal, has been validated for use in immunofluorescence, as well as IHC (P) and WB and has been cited 386 times.

The anti-GSK3 β antibody (clone 3D10; Novus Bio, NBP1-47470SS), mouse monoclonal, has been cited 10 times, and validated for use in WB, ICC/IF, IHC, ELISA, and flow cytometry. In previous work, we also found that the antibody recognizes a single major GSK3 β band in WB.

The anti-pTyr216-GSK3 β Millipore Sigma, SAB4300237, rabbit polyclonal, is an affinity purified antibody which has been validated by Millipore Sigma for use in immunofluorescence (using breast cancer samples), and shows a unique band at the expected molecular weight in WB.

The anti-pSer9-GSK3 β (Abcam, ab131097), rabbit polyclonal, has been validated for use in immunofluorescence, as well as WB, IHC-P, ICC/IF and has been cited 78 times.

The anti-Iba1 (clone EPR16588; Abcam, ab178846), rabbit recombinant monoclonal, has been validated for use in immunofluorescence, as well as WB, IHC-P, ICC/IF and has been cited 873 times.

The anti-PSD-95 antibody (clone K28/43; Biolegend, 810401), mouse monoclonal, is quality tested by Sigma, and has been validated for use in immunofluorescence; it has been cited 12 times.

The anti-Synaptophysin (clone SY38; Millipore Sigma, MAB5258-I), mouse monoclonal, has been validated for use in immunofluorescence, as well as flow cytometry, IHC-P and has been cited 255 times.

The anti-Neurofilament marker (clone SMI-312; pan axonal marker; Biolegend, 837904) is a mouse monoclonal antibody which has been validated for use in immunofluorescence, is IHC-P in-house quality tested, and has been cited over 100 times.

The anti-GPNMB (clone 2B10B8; PTGlab, 66926-1-Ig), mouse monoclonal, has been validated for use in immunofluorescence, as well as WB, IHC, IF/ICC, and ELISA and has been cited 4 times.

The anti-LPL (Novus Bio, AF7197-SP), goat polyclonal, has been validated for use in immunofluorescence, as well as WB, IHC, and ICC and has been cited 11 times.

The anti-MAP2 (PhosphoSolutions, 1099-MAP2), goat polyclonal, detects human, mouse, and rat MAP2 and is Protein G purified. It is recommended for use in WB, ICC and IHC. It has been cited 3 times.

The anti-Myelin Basic Protein (MBP) (clone D8X4Q; Cell Signaling, 78896), is a rabbit IgG monoclonal that recognizes endogenous levels of total myelin basic protein in mouse, rat and human. It is recommended for WB, ICC, IF and IHC-P and has been cited 114 times.

The anti-PDGFR α (R&D Systems, AF1062) is an affinity-purified goat polyclonal IgG that recognizes the mouse antigen in WB, ELISA and IHC. It has been cited 322 times.

Eukaryotic cell lines

Policy information about [cell lines and Sex and Gender in Research](#)

Cell line source(s)

The BV2 cell line has been available in the Yankner laboratory for over 20 years; we used original stocks stored at -180 deg. Celsius to derive the lines used in this study.

Authentication

The cells are positive for the microglial markers CD11b and Iba1, and exhibit a small, round to slightly elongated shape with a clear cytoplasm and sometimes short processes, consistent with microglial morphology.

Mycoplasma contamination

Not tested.

Commonly misidentified lines (See [ICLAC](#) register)

No commonly misidentified cell lines were used in this study.

Animals and other research organisms

Policy information about [studies involving animals; ARRIVE guidelines](#) recommended for reporting animal research, and [Sex and Gender in Research](#)

Laboratory animals

Mus musculus was used to model brain aging and Alzheimer's disease (AD), employing both wild-type (WT) and transgenic mouse lines. WT mice were on a C57BL/6J background. The 3xTg mice17 carry APPSwe and tauP301L mutant transgenes, as well as a PS1 knock-in mutation, and were in a hybrid C57BL/6J and 129Sv/Ev background. The J20 mice16 express transgenic mice express a mutant form of the human amyloid protein precursor bearing both the Swedish (K670N/M671L) and the Indiana (V717F) mutations (APPsW^{Ind}) in a C57BL/6J background.

To assess treatment effects on disease onset and progression, animals were treated either before pathology emerged (5–6 months for 3xTg; 3 months for J20) or after pathology was established (starting at 9 months for 3xTg and 17 months for J20). To investigate age-related effects in wild-type (WT) mice, chronic treatments were initiated in adulthood (10–12 months) and continued for 10–14 months during aging.

Wild animals

No wild animals were used in this study.

Reporting on sex

Both male and female mice were included in the study, and the major findings were consistent across sexes. Details on the number and sex of animals used in each experimental group are provided in the Source Data file.

Field-collected samples

No field collected samples were used in this study.

Ethics oversight

Animal housing and experimental procedures were approved by the Institutional Animal Care and Use Committee of Harvard Medical School.

Note that full information on the approval of the study protocol must also be provided in the manuscript.

Plants

Seed stocks

N/A

Novel plant genotypes

N/A

Authentication

N/A